

EUROPEAN
CONFERENCE ON
INTEGRATED OPTICS

# ECIO 2016

European Conference on Integrated Optics

Warsaw University of Technology, Poland

*Collected Manuscripts*

(c) Copyright 2016 The ECIO Board. All rights reserved.

# Contents


| ID | Author | Title |
|---|---|---|
| S1.1 | Andrea MELLONI*, Daniele MELATI, | Tunable photonic integrated toolbox: from realistic models to control algorithm |
| S1.2 | Philippe LALANNE, Rémi FAGGIANI | Light interaction with resonance |
| S1.3 | Wim BOGAERTS1,2* | Challenges for Designing Large-scale Integrated Photonics |
| S2.1 | Tomasz R. WOLIŃSKI1*, Agata SIAR | Nanoparticles-based Liquid Crystals Integrated with Photonic Crystal Fibers |
| S2.2 | Thomas F. KRAUSS*, Graham J. TRI | Multimodal Photonic Crystal Biosensors |
| S2.3 | Samuel Serna1,2,*, Weiwei Zhang1 | GVD control of low loss slot photonic crystal waveguides for hybrid silicon photonics |
| S3.1 | Michael WALE1,2* | InP-based Photonic Integration: Achievements and Opportunities |
| S3.2 | Anna LUKOWIAK1, Lidia ZUR2,3, Da | Glass and Glass-Ceramic Photonic Systems |
| S4.1 | Piotr ROZTOCKI1, Michael KUES1*, | Quantum state generation via integrated frequency combs |
| S5.1 | Meint K. SMIT | Prospects for InP-based integrated photonics |
| S5.2 | Juerg LEUTHOLD, Wolfgang HENI, C | Plasmonics – a Technology for Microscale High-Speed Integrated Optics |
| S5.3 | M. BUGAJSKI1, K. PIERŚCIŃSKI1, D | Monolithically integrated coupled-cavity quantum cascade lasers |
| S6.1 | Cuma TYSZKIEWICZ*, Paweł KARASIŃ | Sol-gel derived rib waveguides for evanescent wave spectroscopy |
| S6.4 | Stanisław STOPIŃSKI*1, Krzysztof | Integrated optical time division reflectometer |
| S6.5 | S. NÚÑEZ-SÁNCHEZ1*, E. BAQUEDANO | Lossy Metallic Micro/Nano-Structures for Solar Thermal Applications |
| S6.8 | De-Long Zhang1,2*, Xiao-Fei Yang | Near-stoichiometric Ti:D:LiNbO3 (D = Mg2+, Sc3+, Ga3+, Zr4+) Optical Waveguides for Integrated Optics |
| S6.10 | Marcin KOBA1,2*, Paweł SZCZEPAŃS | Threshold Analysis of 2-D Gain and Index Coupled Photonic Crystal Lasers |
| S6.11 | Hongsik Jung1* | Integrated Photonic Lithium-Niobate Electric-Field Sensor utilizing a Y-fed Balanced-Bridge(YBB) MachZehnder Interferometric Modulator |
| S6.12 | Konrad MARKOWSKI1, Kazimierz JED | Pareto optimization of group delay response of apodized tapered fibre gratings |
| S6.14 | Marta SOŁTYS1*, Agnieszka KOS1, | White luminescence in borate and phosphate glasses containing lead |
| S7.1 | Alwyn SEEDS1*, Siming CHEN1, Jia | Direct Integration of Quantum Dot Lasers on Silicon |
| S7.2 | Erwin Bente1, Sylwester Latkowsk | Mode locked laser systems on InP integration technology platforms |
| S7.3 | M. Deseada GUTIERREZ1,2*, Jules | Monolithically Integrated Lasers for Comb Generation in Bandwidth Variable Transponders |
| S7.4 | Vinicio CORRAL1*, Robinson GUZMA | Integrated Long Cavity Mode Locked Ring Laser |
| S7.5 | B. ROMEIRA*, V. DOLORES-CALZADI | High-Speed Direct Modulation of Waveguide-Coupled Metal-Cavity Nano-Light-Emitting Diodes |
| S7.6 | Mao OKADA1, Kazuto TAKAHASHI1, H | Multi-Wavelength Lasing with SOA and AWG for Linear-Cavity Fiber Sensor |
| S8.1 | Mariangela GIOANNINI1*, Paolo BA | Analysis of Quantum Dot Single Section FP Lasers for Comb Spectra Generation |
| S8.2 | Daan LENSTRA Eindhoven Universit | Rate-Equation Analysis for an Integrated Coupled- Cavity Laser with MMI Anti-Phase Coupler |
| S8.3 | Giannis POULOPOULOS1*, Dimitrios | Angled 3D Glass-to-SiPh adiabatic coupler |
| S8.4 | Pierre WAHL16, Ivo COUCKUYT2, Ch | Optimization of Silicon Photonic Components using Multi-Fidelity Simulations and Co-Kriging |
| S8.5 | Perry van SCHAIJK*, Daan LENSTRA | Feedback-Insensitive Integrated Laser |
| S9.1 | Moritz SEYFRIED*, Andreas HOPFMU | Laser soldering for highest-accuracy passive bonding applications |

| | | |
|---|---|---|
| S9.2 | Maciej FIMIARZ*, Przemysław KALI | Integratated IR detection modules |
| S9.3 | Martin KIRCHNER | High Fidelity Electron Beam Lithography for Photonic Devices |
| S9.5 | Marcin TOMKIEWICZ1, Jarosław KUC | PICs in Terabit Networks |
| S10.1 | Martijn J. R. HECK | Optical Isolators for Photonic Integrated Circuits |
| S10.2 | Hon Ki TSANG, Linghai LIU | Engineering the optical characteristics of waveguide grating couplers |
| S10.3 | De-Long Zhang1,2*, Jia-Qi Xu1, W | Electro-optic Long Period Ti:LiNbO3 Waveguide Gratings in Parallel for Broadband Filtering |
| S10.4 | Weiwei Zhang*, Samuel Serna, Xav | Critical coupling enhanced refractive index sensing in SOI slot microring resonators |
| S10.5 | Jose D. SARMIENTO-MERENGUEL1, Ca | Integrated polarization controller with 40 dB polarization extinction ratio range in the C-Band |
| S11.1 | Zhenguo LU | Coherence Comb Laser Sources: Quantum Dots, Packaging and Active Control |
| S11.2 | S. Latkowski1*, P.J. van Veldhov | Indium phosphide monolithic photonic integrated circuits for gas sensing applications |
| S11.3 | Vadim POGORETSKIY*, Aura HIGUERA | Development of active-passive regrowth for buttcoupled lasers in membrane photonic integrated circuits |
| S11.4 | Carlos D. GORDON1*, Mu Chieh LO1 | On-Chip Multiple Colliding Pulse Mode-Locked Laser for Millimeter and Terahertz Wave Generation |
| S12.1 | Simone BERNESCHI1, Immacolata An | Waveguide coupled high-Q micro-optical resonators |
| S12.2 | D. Benedikovic1,*, C. Alonso-Ram | Highly-Efficient Subwavelength Engineered Grating Couplers for Silicon-on-Insulator Waveguides |
| S12.3 | Dan ZHAO1*, Dzmitry PUSTAKHOD1, | Optical frequency domain reflectometry for characterization of waveguide crossings |
| S12.4 | Maxim NERADOVSKIY1,3*, Dmitry CH | Highly efficient nonlinear waveguides in LiNbO3 fabricated by a combination of Soft Proton Exchange (SPE) and E-beam writing. |
| S13.1 | Peter G.R. SMITH*, Christopher H | A new hybrid fibre / planar platform for optics, offering ultralow loss and robust integration |
| S13.2 | Sylvie MENEZO1* | Overview of Laser Sources for Silicon Photonic Transceivers |
| S13.3 | Anne Talneau, I. Sagnes and G. P | High-Optical-Quality Oxide-Free InP-on-Si Hybrid Interface |
| S13.4 | Paul MUELLNER1*, Alejandro MAESE | CMOS-compatible low-loss silicon nitride waveguide integration platform for interferometric sensing |
| S13.5 | Timo AALTO1*, Mikko HARJANNE1, M | Euler bends and TIR mirrors for ultra-dense PIC integration on SOI |
| S13.6 | Valeria RUSTICHELLI1,2*, Huub H. | Buried heterostructures for deep UV lithography |
| S15.5 | Longfei SHEN1*, Yuqing JIAO1, Au | Double-sided processing for membrane-based photonic integration |
| S16.5 | Ripalta STABILE*, Prometheus DAS | Fast and Energy Efficient Micro-Ring-Resonator-Based 4×4 InP Switch Matrix |
| S17.1 | Moritz BAIER*, Francisco M. SOAR | A New Approach to Designing Polarization Rotating Waveguides |
| S17.2 | S. Latkowski1*, P.J. van Veldhov | COBRA long wavelength active-passive monolithic photonic integration technology platform |
| S17.3 | M. DING, A. WONFOR, Q. CHENG, N. | Low-Energy, Dilated 4×4 Hybrid MZI-SOA Cross-point Optical Switch |
| S17.4 | D. GALLAGHER, A. DABBS | Design environment for active photonic integrated circuits improves the DML |
| S17.5 | Victor DOLORES-CALZADILLA*, Fran | InP-based Photonic Integration Platform: Status and Prospects |
| S17.6 | Shuxuan Zhu1*,Adrian Wonfor1, Ad | Unidirectional Operation of a Monolithically Integrated Mode locked Semiconductor Ring Laser |

ECIO 2016
18TH EUROPEAN CONFERENCE ON INTEGRATED OPTICS 2016
18–20 MAY | WARSAW | POLAND

# Tunable photonic integrated toolbox: from realistic models to control algorithm

**Andrea MELLONI*, Daniele MELATI, Stefano GRILLANDA, Andrea ANNONI, Nicola PESERICO[1] and Francesco MORICHETTI**
Dipartimento di Elettronics, Informazione e Bioingegneria, Politecnico di Milano,
via Ponzio 34/5, 20133 Milano, Italy
* andrea.melloni@polimi.it

The evolution towards complex photonic circuits integrating many building blocks and functionalities poses major issues on the design as well as on the control of the functionality in real operation conditions. Optical and thermal interactions between single devices, spurious effects, drifts, non-idealities and fabrication uncertainties can prevent the realized circuits to work as expected. As a consequence, advanced photonic devices must be considered as a system to control with feedback loops and algorithms, and the above non-idealities must be taken into account also during the early design stages to evaluate their impact on the circuit behavior and perform robust optimizations towards the parameters of interest.
Here, the estimation of the impact of the tolerances on a tunable delay line and a robust optimization of a filter, are reported. Further, the tools needed to monitor and control a complex circuit are described and an example discussed.

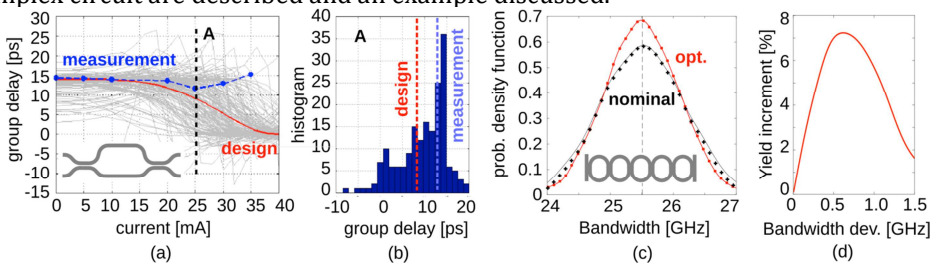



**Fig. 1. (a) Group delay of a Mach-Zehnder filter as function of the current fed into the controller of the tunable couplers and (b) histogram at 25 mA. (c) Probability density function of the 3-dB bandwidth of a five-ring-resonator filter for nominal (black curve) and optimized design (red curve). (d) Circuit yield increment for the optimized design.**

Circuit simulators enriched by advanced Process Design Kits and complex models are emerging as the right tools to perform this kind of analyses [1,2]. As an example, Fig.1 (a) shows the Monte-Carlo analysis of the group delay of a tunable delay line based on unbalanced Mach-Zehnder Interferometer (MZI) with tunable couplers (realized with two balanced MMI-based MZIs) when exposed to fabrication uncertainties. Group delay is reported as function of the current fed to the thermal actuators used to change the splitting ratio of the two couplers. Simulations were performed with the commercial circuit simulator Aspic [3]. Red curve shows the designed group delay that is expected to drop of about 15 ps applying a current of 40 mA. In order to describe realistic "grand challenge" and a major obstacle to the advent of large-scale photonic integrated systems. The possibility to control the PIC is a key requirement for different reasons and in many applications: i) reconfigurability of circuits to provide the required functionality such as in routers, cross-connects, tunable bandwidth filters, reconfigurable add-drop multiplexers, etc.; ii) adaptive circuits that modify their behavior depending on the state of the system such as signal polarization state, signal to noise ratio, crosstalk, eye aperture, BER, etc.; iii) locking or stabilization

of the circuit in a well-defined state independently of the temperature, electrical fluctuations, drifts, stress, aging, etc; iv) compensation of fabrication tolerances and technological non-uniformities. All these requirements become even more critical when dealing with wavelength selective devices, such as microrings resonators, high bit rate signals operating in coherent domain, dense WDM systems and densely integrated PICs realised on semiconductor platforms, such as silicon and indium phosphide InP. Local and global feedback control tools and strategies will soon become the ordinary way to operate even for simple circuits.

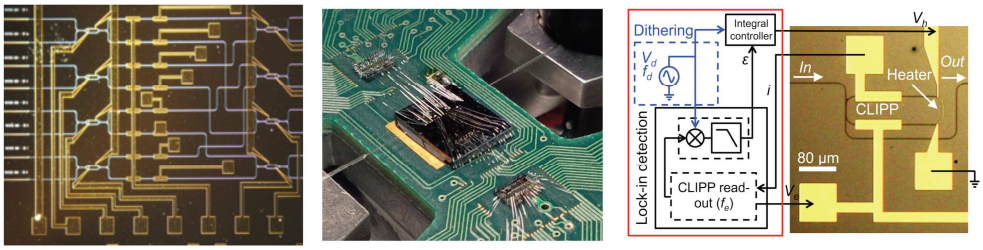



**Fig. 2. (from left to right) An 8x8 Silicon Photonic Router with heathers and CLIPPs, mounted on a PCB with two CMOS ASICs for the control and readout and a detail of a ring resonator with feedback control loop.**

In order to realize a feedback control loop, light monitors and actuators are required, in addition to an electronic control unit and control strategies. Monitoring approaches based on conventional photodetectors are not effectively scalable to large-scale PICs due to the need for multi-point light tapping. In this work, we report on our recent achievements on the development of an in-line transparent integrated detector, named ContactLess Integrated Photonic Probe (CLIPP) [5,6,7], that can monitor the light intensity in semiconductor waveguides without introducing any photon absorption in excess to the waveguide propagation loss and on the control strategies for PICs. Results shown in this work demonstrate the effectiveness of the non-invasive CLIPP technology for the feedback-control tuning, switching, and locking of silicon PICs. As an example, Fig. 2 shows an 8x8 Silicon Photonic Router with heathers and CLIPPs, mounted on a PCB with two CMOS ASICs for the control and readout and a detail of a ring resonator with feedback control loop. The CLIPPs permits to monitor the circuit in every desired point and control the working points of the various elements individually.

Also, when multiple optical signals are simultaneously injected at different input ports of a circuit, like a switch fabric, CLIPP detectors can be used to identify channels coming from specific input ports regardless of the presence of other concurrent channels injected at the other input ports if these are labelled with a tone with an intensity modulation amplitude of a few percent and a frequency in the order of some

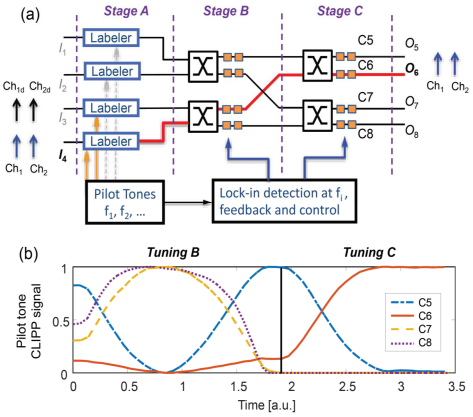



**Fig. 3. CLIPP assisted lightpath tracking using on-chip labelling with pilot tones: scheme and CLIPPs signal after the stage B and stage C.**

kilohertz. Fig. 3 shows the CLIPP assisted lightpath tracking of concurrent signals distinguished by using on-chip labelling through pilot tones.
In conclusion, we have shown the software tools for the design and analysis of circuits in presence of tolerances, non-perturbative probes for monitoring and feedback algorithms and for locking and control of complex PIC. This toolbox is strategic for a fully exploitation of the capabilities of photonic circuits.

References

[1] D. Melati,et al., *Statistical Process Design Kits: analysis of fabrication tolerances in integrated photonic circuits,* Proceedings IPR, IT4A–5, OSA, 2015
[2] T. Weng, et al., *Uncertainty quantification of silicon photonic devices with correlated and non-Gaussian random parameters*, Optics express 23, 4242–4254 (2015)
[3] Aspic, http://www.aspicdesign.com, Phoenix bv, http://www.phoenixbv.com
[4] T. Weng, et al., *Stochastic Simulation and Robust Design Optimization of Integrated Photonic Filters*, submitted to Nanophotonics
[5] F. Morichetti et al., "Non-invasive on-chip light observation by contactless waveguide conductivity monitoring," IEEE J. Sel. Top. Quantum Electron. 20, 1–10, 2014
[6] S. Grillanda *et al.*, "Non-invasive monitoring and control in silicon photonics using CMOS integrated electronics," Optica 1, 129-136, 2014
[7] D. Melati et al., "Contactless integrated photonic probe for light monitoring in InP-based devices. IET Opt. 9, 2015

ECIO 2016
18TH EUROPEAN CONFERENCE ON INTEGRATED OPTICS 2016
18–20 MAY | WARSAW | POLAND

# Light interaction with resonance

**Philippe LALANNE, Rémi FAGGIANI and Jianji YANG**
LP2N, CNRS, Institut d'Optique, IOGS - Univ. Bordeaux, 33400 Talence, France
* philippe.lalanne@institutoptique.fr

Thanks to an efficient and intuitive quasi-normal mode formalism valid for micro and nanoresonators made of dielectric as well as lossy and dispersive materials, we shine new light on the physics and modelling of light interaction with electromagnetic resonances [1]. In particular in the present context, we will discuss the role of quenching for light emission in metallic nanogap devices and will revisit the perturbation theory of electromagnetic resonance.

Simply because they enhance the electromagnetic field, micro/nano resonators play an important role in modern photonics. Perhaps they are as important as waveguides. A resonance mode is a solution of Maxwell's equations without source with a complex frequency, and the resonance quality factor Q equals the ratio between the real and imaginary parts of the frequency.

However, the maturity level of the theory and computation of resonances is ridiculously small compared to that reached for waveguides (see, e.g., the books by Marcuse, Snyder and Love, Vassalo …). As a matter of fact, very few scientists in nanophotonics and optics would be able to calculate and properly normalize the resonance modes with a complex frequencies.

As the frequency is complex, the resonance field exponentially diverges as the distance r to the resonator increases, $\exp(ikr) \rightarrow \infty$ since $k=w/c$ is complex, making a mode normalization difficult. We have recently challenged the longstanding normalization issue of resonance modes, and have been able to define (properly?) the "famous" mode volume [1].

Thanks to this theoretical upstream work, we explain why an emitter placed in a metallic nanogap (thickness < 10 nm) does not quench much despite the small distance to the metal, and the consequences for nanogap antenna [2] and revisit perturbation theory of resonator [3].

References

[1] C. Sauvan, J. P. Hugonin, I. S. Maksymov, and P. Lalanne, *Theory of the Spontaneous Optical Emission of Nanosize Photonic and Plasmon Resonators*, Phys. Rev. Lett. 110, pp. 237401, 2013
[2] R. Faggiani, J. Yang, P. Lalanne, *Quenching, Plasmonic, and Radiative Decays in Nanogap Emitting Devices*, *ACS Photonics 2* (12), pp 1739-1744, 2015
[3] J. Yang, H. Giessen, P. Lalanne, *Simple Analytical Expression for the Peak-Frequency Shifts of Plasmonic Resonances for Sensing*, Nano Lett. 15 (5), pp 3439-3444, 2015

ECIO 2016
18TH EUROPEAN CONFERENCE ON INTEGRATED OPTICS 2016
18–20 MAY | WARSAW | POLAND

# Challenges for Designing Large-scale Integrated Photonics

**Wim BOGAERTS**[1,2*]
[1]Ghent University – IMEC, 9000 Ghent , Belgium
[2]Luceda Photonics, 9200 Dendermonde, Belgium
* wim.bogaerts@ugent.be

With the growing adoption of silicon photonics in data- and telecommunication as well as sensing and spectroscopy, the difficulties of designing larger circuits in this technology have become more prominent. Silicon photonic waveguides have submicron dimensions, and can therefore be integrated in large numbers on a chip. But these same submicron dimensions give rise to extreme sensitivity of the waveguide response to small variations in geometry, temperature, stress etc. Multiply this with thousands of functional building blocks and even more interconnects, and it is clear that it becomes very challenging to guarantee the correct functionality of a photonic integrated circuit. Even if the circuit is nominally correct, compound variability can still dramatically lower the yield.

When designing silicon photonic chips, it is important to start from a workflow which has the largest chance of transferring the intent of the designer to a working chip layout for fabrication. Such a workflow is known in electronic design automation (EDA). It makes sense to reuse this model from electronics because photonic circuits are ever more tightly integrated with electronics, both technologies make use of similar planar manufacturing processes, design frameworks exist and there is a large community of expertise. An EDA workflow starts from a schematic circuit that can be optimized for the desired functionality. As electronics and photonics use different physics, it is challenge is to combine the two circuit models into a single design flow. The circuit description can then be implemented in a chip layout manually or with assistance of a *schematic driven layout* tool. Again, photonics imposes different constraints on layout than electronics. The resulting layout should then be verified against design rules (*design rule check*) and the functionality is checked against the original specifications (*layout-vs-schematic*). Here as well, photonics imposes challenges in extracting the connectivity and verifying the curved geometries.

While the similarities in design flows already enable photonic designers to a large extent, the challenges in each step, combined with the inherent variability of the process and operational conditions, make it very hard to accurately predict the yield of larger circuits. *Design-for-Manufacturability* (DfM) techniques that are used for electronics cannot necessarily be applied for photonics. We will discuss the different challenges in detail and also present some of the solutions that are emerging.

References

[1] W. Bogaerts, M. Fiers, P. Dumon,, *Design Challenges in Silicon Photonics*, J. Sel. Top. Quantum Electron., vol. 20, no. 4, 1-8, 2014
[2] L. Alloatti, M. Wade, V. Stojanovic, M. Popovic and R. J. Ram, *Photonics design tool for advanced CMOS nodes,* in IET Optoelectronics, vol. 9, no. 4, pp. 163-167, 8 2015.
[3] M. Heins, et al. *Design Flow Automation for Silicon Photonics: Challenges, Collaboration, and Standardization,* Silicon Photonics III. Springer Berlin Heidelberg, 2016. 99-156.

ECIO 2016
18TH EUROPEAN CONFERENCE ON INTEGRATED OPTICS 2016
18–20 MAY | WARSAW | POLAND

# Nanoparticles-based Liquid Crystals Integrated with Photonic Crystal Fibers

**Tomasz R. WOLIŃSKI[1*], Agata SIARKOWSKA[1], Miłosz CHYCHŁOWSKI[1]**
**Bartłomiej JANKIEWICZ[2], Roman DĄBROWSKI[2]**

[1]Faculty of Physics, Warsaw University of Technology, Warszawa, 00-662, Poland
[2]Military University of Technology, Warsaw, Poland
[*] wolinski@if.pw.edu.pl

Liquid crystals (LCs) are materials with an unceasing interest due to their unique properties as: electric field-induced director axis reorientation or a vast range of optical anisotropies. All these properties made LCs to be widely used in LC displays. However, these devices still need an improvement of their electro-optical response times, which are relatively slow compared to electroluminescent devices. Recently, there has been a growing interest in dispersing nanoparticles (NPs) in LCs. Metal NPs can adopt a vast number of structural geometries with an electronic structure. Even a small amount of metallic NPs (gold or silver) should be sufficient to influence both the dielectric anisotropy as well threshold voltage of LCs [1].

One of the promising ideas is to integrate NPs-doped LCs with photonic crystal fibers (PCFs) that may result in significant improved efficiency of electric field tuning. Photonic structures referred as photonic liquid crystal fibers (PLCFs) with highly improved spectral, polarization, and guiding tuning properties were proposed more than 10 years ago [2]. Light propagation in PLCFs is governed by one of two principal guiding mechanisms responsible for light trapping within the core and can be dynamically changed by introducing NP-doped LCs into the air-channels, broadening the applicability of PCFs. It appeared that the use of LCs as an infiltrating material greatly improved optical properties of PCFs, also when doped with NPs [3].

The lecture will discuss the latest experimental results of PCFs infiltrated with nematic LCs doped with metallic NPs. Two types of NPs: titanium NPs and gold NPs and two types of LCs: 6CHBT and 5CB LCs were used to compare an influence of the doping on propagation parameters of the PLCFs and their electro-optical response to external electric field. Such a combination of nanoparticles-based liquid crystals and photonic crystal fibers can be considered as a next milestone in developing of a new class of fiber-based optofluidic systems.

References

[1] M. Mishra, R. Dabrowski, J.K. Vij, A. Mishra, R. Dhar, Liq. Cryst. 42, 1580 (2015),
[2] T.R. Woliński, K. Szaniawska, K. Bondarczuk, P. Lesiak, A.W. Domański, R. Dąbrowski, E. Nowinowski- Kruszelnicki, J. Wójcik, Opto-Electronics Rev. 13, 177 (2005).
[3] L. Scolari, S. Gauza, H. Xianyu, L. Zhai, L. Eskildsen, T.T. Alkeskjold, S.-T. Wu, A. Bjarklev, Opt. Express 17, 3754 (2009).

ECIO 2016
18TH EUROPEAN CONFERENCE ON INTEGRATED OPTICS 2016
18–20 MAY | WARSAW | POLAND

# Multimodal Photonic Crystal Biosensors

**Thomas F. KRAUSS*, Graham J. TRIGGS, Yue WANG, Chris P. REARDON, Jose Juan COLAS, Steven D. JOHNSON**
[1]Department of Physics, University of York, YO10 5DD, UK
* thomas.krauss@york.ac.uk

Photonic Crystals are the culmination of many fascinating developments in Physics, such as Bragg mirrors, Bloch modes, and bandstructures. Their ability to control the flow of light has given rise to many applications, ranging from light emission to optical switching and light trapping in photovoltaics [1]. Here, we discuss a novel sensing & imaging architecture, whereby the localised guided mode resonances of the photonic crystal can be considered the pixel of an image [2]. This combination adds an exciting new imaging modality to the biophotonics toolkit, which allows us to image both cells and the biomarkers they secret in real time. Thinking of each resonance as an imaging pixel also provides a very simple readout mechanism, where we have now demonstrated nanomolar sensitivities with a device that, in principle, can be made for £10 (Fig. 1) [3]. Furthermore, we note that silicon photonic biosensors do not tend to exploit silicon's obvious ability to conduct electricity, and we demonstrate the first hybrid silicon photonic - electrochemical biosensor [4].

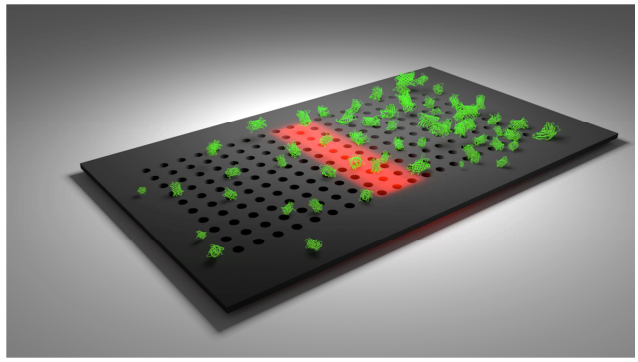


**Fig. 6. Artist's impression of a photonic crystal biosensor that affords a simple camera readout, as the resonance is localised in a certain part of the photonic crystal depending on the local refractive index; as the index changes due to, e.g. the attachment of biomolecules, the resonanace moves to a different position on the chip.**

References

[1] F. Priolo, T. Gregorkiewicz, M. Galli and T.F. Krauss, "Silicon nanostructures for photonics and photovoltaics", Nature Nanotechnology 9, pp. 19-32 (2014)
[2] G. J. Triggs, M. Fischer, D. Stellinga, M. G. Scullion, G. J. O. Evans, T. F. Krauss, "Spatial resolution and refractive index contrast of resonant photonic crystal surfaces for biosensing", IEEE Photonics Journal 7, 6801810 (2015)
[3] G.J. Triggs, Y. Wang, C.P. Reardon, M.Fischer, G.J.O. Evans and T.F. Krauss, "The chirped grating biosensor" (under review)
[4] J.J. Colás, A. Parkin, K.E. Dunn, M.G. Scullion, T.F. Krauss and S.D. Johnson "The electro-photonic silicon biosensor" (under review)

ECIO 2016
18TH EUROPEAN CONFERENCE ON INTEGRATED OPTICS 2016
18–20 MAY | WARSAW | POLAND

# GVD control of low loss slot photonic crystal waveguides for hybrid silicon photonics

**Samuel Serna[1,2,*], Weiwei Zhang[1], Xavier Le Roux[1], Laurent Vivien[1], and Eric Cassan[1]**

[1]Institut d'Electronique Fondamentale, University Paris-Sud, CNRS UMR 8622, Université Paris Saclay, Bat. 220, 91405 Orsay Cedex, France

[2] Laboratoire Charles Fabry, Institut d'Optique Graduate School, CNRS, Université Paris Saclay, 2 Avenue Augustin Fresnel, 91127 Palaiseau Cedex, France

*samuel.serna@u-psud.fr

## Abstract

Photonic Crystal Waveguides are key components to study diverse phenomena in the linear and nonlinear regimes for integrated circuits and rise as a promising platform to host novel materials. Nevertheless, serious limitations are manifest when slow light is targeted, mainly the propagation losses [1,2]. Even though, photonic crystals are theoretically lossless, the practical implementation is limited by the fabrication accuracy, mainly during the lithographic and etching steps. Interesting studies have been performed in W1-like photonic crystals in order to engineer the losses for given group indices [2]. Further, slot waveguides are known to suffer from larger roughness-induced scattering extrinsic losses than Si wires due to a higher electric field interaction regarding the continuity of the electrical displacement vectors. Then, slot photonic crystal waveguides (SPCW) enhance both sides: hollow core effect and slow light, the light-matter interaction with guest materials, such as polymers or doped compounds.

For optical data transfer and nonlinear applications, the dispersion properties of the waveguides should be carefully addressed. Some interesting approaches for this dispersion engineering in photonic crystals have been theoretically proposed and numerically explored during the last decade. Some of them rely in exotic shapes or asymmetries. This is compelling from a physical point of view but when nanofabrication is considered, the latter approaches are difficult if not impossible to produce. In this work, we have performed rigorous experimental studies under different approaches to determine the best compromise regarding electronic beam lithography, group index, propagation length and losses in slotted structures. As in the lithographic process the average hole position (center) is easier to control than the hole shape, we have experimentally shifted the first two row of holes and vary the radius of the first row to see the effect on the dispersion curves.

## Simulations and Experiments

The basic geometry consists in a structure with a lattice constant of $a$=420 nm, and the hole radius $r$ is 125 nm to ensure a wide TE bandgap. In order to tune the mode and achieve changes in the dispersion curves, the first row of holes was shifted towards the slot by 0.20$a$ and the second row shifted outwards by 0.35$a$ (see Fig. 1). In this study, the radius of the second row of holes was fixed to 125 nm but the radius of the first row was shifted in order to quantify the experimental effects in small changes of only one parameter. The sweeping values are from 95 nm until 125 nm. We have guaranteed the single mode operation and some degree of freedom against possible fabrication imperfections.

In this abstract we only present, as a typical example, the results obtained for the waveguide with $r_1$=95nm. For instance, we show in Fig.1 a comparison between the two band diagrams of a dispersion engineered waveguide and a SPCW with a fixed radius of 125 nm and no hole shifting. The structures have been filled with a Cargille liquid of refractive index of 1.45 at 1550nm. Some insights about the effect of the indices of the forbidden band and dispersion properties will be detailed during the conference.

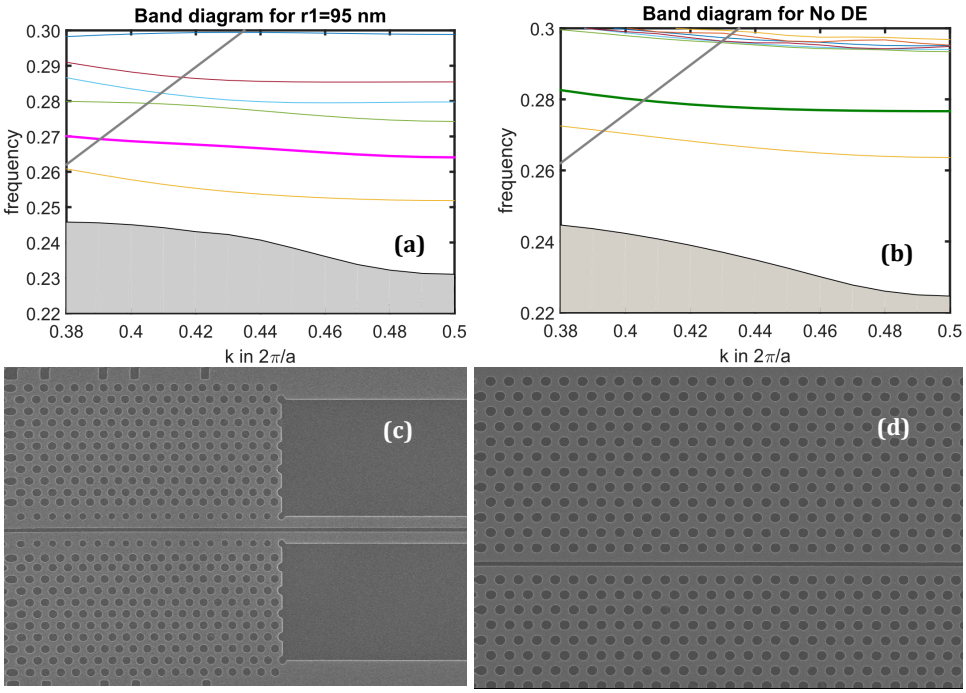



**Fig. 21. Band diagram of (a) $r_1$=95nm radii of the first row of shifted holes and (b) photonic crystal with no DE ($r$=125nm), (c) and (d) are the respective SEM images of the waveguides. Notice the difference between the first and second row of holes.**

It is known that losses dramatically vary with the light group velocity (ng), typically scaling as ng and then ng$^2$ after a given ng-threshold [1]. This is the reason why any loss estimation in our waveguides should be achieved for a given ng value. The losses in a particular waveguide of 700 μm long could be appreciated from Fig. 2 (a) where a strip waveguide (red) is plotted as reference to compare the on-chip propagation losses. Even though the differences are not noticeable in the scanning electron microscope, there are clear alterations in the optical characterization that we explore with different devices.

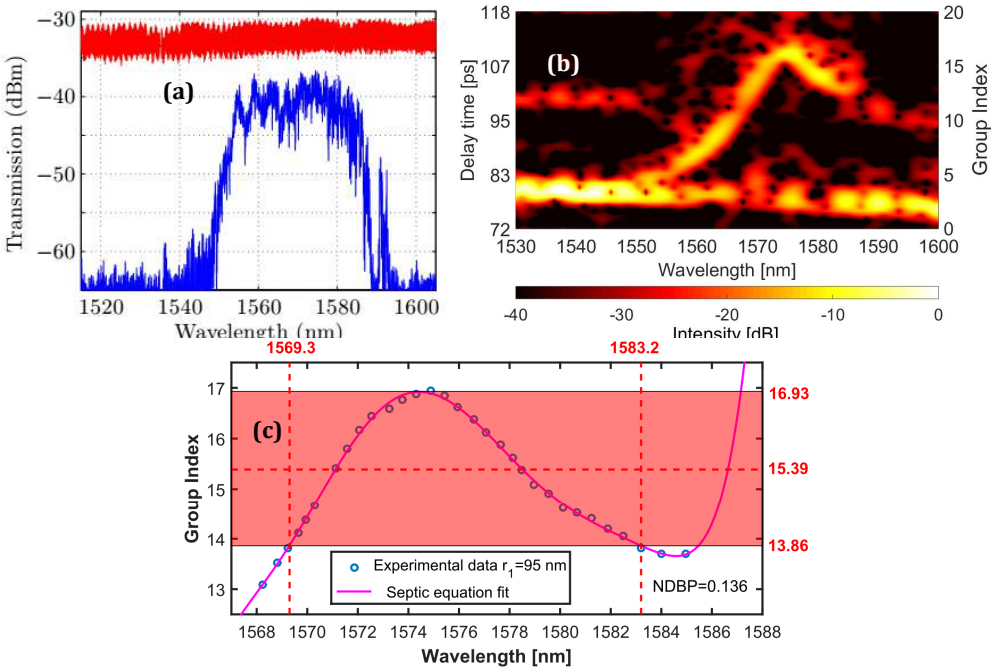



**Fig. 2. (a) Optical transmission of a 700 μm SPCW (blue) and a strip waveguide (red). (b) Reflectance map showing the behavior of the photonic delay as a function of the wavelength and (c) Fitting of the dispersion curve with a seventh order polynomial fit (septic equation) with an estimation of a 10% variation of ng.**

In Fig. 2 (b) we present the reflectance map of the photonic crystal waveguide [4] where the deflection of the optical delay is clear and the estimation of the average group index is around 15.4 (c). This represents to the best of our knowledge the first experimental demonstration of dispersion engineered SPCW.

Several nonlinear experiments in the slow light regime require the dispersion compensation over a wide bandwidth. For instance, in W1 waveguides, the increase of the confined electric field due to spatial pulse compression have been used to improve the FWM efficiency or the photon generation of correlated photon pairs in the quantum regime. So the engineered hybrid waveguides open a window to novel frontiers in the investigation of new materials and phenomena.

## References

[1] L. O'Faolain, et al. *Loss engineered slow light waveguides*, Opt. Express vol. 18, p.p. 27627-27638, 2010.

[2] S. Mazoyer, et al. *Statistical fluctuations of transmission in slow light photonic-crystal waveguides*, Opt. Express vol. 18, pp. 14654-14663, 2010.

[3] Wu, J., et al. *Wideband and low dispersion slow light in slotted photonic crystal waveguide.* Opt. Comm. vol. 283, pp. 2815-2819, 2010.

[4] A. Parini, et al., *Time-wavelength reflectance maps of photonic crystal waveguides: a new view on disorder-induced scattering*, J. Lightwave Technol. vol. 26, p.p. 3794–3802, 2008.

ECIO 2016
18TH EUROPEAN CONFERENCE ON INTEGRATED OPTICS 2016
18–20 MAY | WARSAW | POLAND

# InP-based Photonic Integration: Achievements and Opportunities

**Michael WALE[1,2*]**

[1]Oclaro Technology Limited, Caswell, Towcester, NN12 8EQ, UK
[2]Photonic Integration Group, Eindhoven University of Technology, Eindhoven, The Netherlands
[*] Mike.Wale@oclaro.com

Photonic Integrated Circuit (PIC) technology based on indium phosphide has evolved over more than 30 years to become a key enabler for high-performance optical communications systems, which form the backbone of the internet, fixed and mobile telephony and all of the data-intensive systems on which modern life depends. In order to accommodate the exponential growth of internet traffic, modern optical fibre systems often employ wavelength division multiplexing with 80-100 channels, using tunable lasers operating under electronic control, whilst advanced modulation schemes coupled with coherent transmission techniques allow very high bit rates (100 Gbit/s per wavelength and above) with high spectral efficiency. The use of such advanced techniques is greatly facilitated by the adoption of integrated photonics and compact coherent transmission modules based on InP PICs are now in volume production alongside existing PIC-based integrated laser-modulator and receiver products for 10 Gbit/s and 40 Gbit/s. High data rate communications within and between data centres present further exciting opportunities for InP PICs.

Although the development of InP PIC technology has historically been driven by communications and this sector still accounts for the majority of the production volumes, it is clear that many other applications can benefit from this technology. InP PIC technology is unique in being able to offer the integration of semiconductor lasers, optical amplifiers, modulators, detectors and a full range of passive waveguide functions, all with very high performance, within a single chip. As such it is expected to become a major enabler for many other business sectors, including medical, industrial and aerospace applications, where complex optical functionality is required within a compact, power-efficient and cost-effective component.

Major progress has been achieved over the last few years in the development of generic platform-based design and manufacturing methods, which will facilitate the use of PICs in new applications and stimulate innovative product design.

The talk will review the current state of the art and point towards future opportunities.

ECIO 2016
18TH EUROPEAN CONFERENCE ON INTEGRATED OPTICS 2016
18–20 MAY | WARSAW | POLAND

# Glass and Glass-Ceramic Photonic Systems

**Anna LUKOWIAK[1], Lidia ZUR[2,3], Davor RISTIC[4,5], Alessandro CHIASERA[3], Stefano VARAS[3], Thi Ngoc Lam TRAN[6,3,7], Marcello MENEGHETTI[8,3], Daniele ZONTA[6,3,9], Dominik DOROSZ[10], Giancarlo C. RIGHINi[2,11], Roberta RAMPONI[12], Maurizio FERRARI[3,2*]**

[1]Institute of Low Temperature and Structure Research PAS, Okolna St. 2, 50-422 Wroclaw, Poland
[2]Centro di Studi e Ricerche "Enrico Fermi", Piazza del Viminale 1, 00184 Roma, Italy
[3]IFN-CNR CSMFO Lab., and FBK Photonics Unit via alla Cascata 56/C Povo, 38123 Trento, Italy
[4]Ruđer Bošković Institute, Division of Materials Physics, Laboratory for Molecular Physics, Bijenička c. 54, Zagreb, Croatia
[5]Center of Excellence for Advanced Materials and Sensing Devices, Research unit New Functional Materials, Bijenička c. 54, Zagreb, Croatia
[6]Department of Civil, Environmental and Mechanical Engineering, Trento University Via Mesiano, 77, 38123 Trento, Italy
[7]Ho Chi Minh City University of Technical Education, 1 Vo Van Ngan Street, Linh Chieu Ward, Thu Duc District, Ho Chi Minh City, Viet Nam
[8]Dipartimento di Fisica, Università di Trento, via Sommarive 14, Povo, 38123 Trento, Italy
[9]Department of Civil and Environmental Engineering, University of Strathclyde, 75 Montrose Street, Glasgow, G11XJ, UK
[10]Bialystok University of Technology, Department of Power Engineering, Photonics and Lighting Technology, 45D Wiejska St., Bialystok 15-351, Poland.
[11]MDF Lab.IFAC - CNR, Via Madonna del Piano 10, 50019 Sesto Fiorentino, Italy
[12]IFN-CNR and Department of Physics, Politecnico di Milano, piazza Leonardo da Vinci 32, 20133 Milano, Italy.
* maurizio.ferrari@ifn.cnr.it

The development of optically confined structure is a major topic in both basic and applied physics not solely ICT oriented but also concerning lighting, laser, sensing, energy, environment, biological and medical sciences, and quantum optics. Glasses and glass-ceramics activated by rare earth ions are the bricks of such structures. Glass-ceramics are nanocomposite systems that exhibit specific morphologic, structural and spectroscopic properties allowing to develop interesting new physical concepts, for instance the mechanism related to the transparency, as well as novel photonic devices based on the enhancement of the luminescence. The dependence of the final product on the specific parent glass and on the fabrication protocol still remain an important task of the research in material science. Looking to application, the enhanced spectroscopic properties typical of glass ceramic in respect to those of the amorphous structures constitute an important point for the development of integrated optics devices, including optical amplifiers, monolithic waveguide laser, novel sensors, coating of spherical microresonators, and up and down converters. This lecture presents some results obtained by our consortium regarding bulks and planar waveguides focusing the discussion on photonics application, and evidences the capital scientific and technological interest of this kind of two-phase materials.

This research was performed in the framework of the projects CNR-PAS (2014-2016), MaDEleNA PAT and COST action MP1401.

ECIO 2016
18TH EUROPEAN CONFERENCE ON INTEGRATED OPTICS 2016
18–20 MAY | WARSAW | POLAND

# Electronic Control and Stabilization of Silicon Photonic Microring Resonator Circuits

**Hasitha Jayatilleka, Robert Boeck, Jonas Flueckiger, Sudip Shekhar, Nicolas A. F. Jaeger, Lukas Chrostowski***
Department of Electrical and Computer Engineering, University of British Columbia, 2332 Main Mall, Vancouver, BC V6T 1Z4, Canada.
* lukasc@ece.ubc.ca

In silicon microring-based circuits with many resonators, in-resonator photoconductive heaters (IRPHs) provide a means for automatic tuning and stabilization by allowing for both monitoring and tuning the resonance conditions of individual resonators. Using IRPHs, automatic tuning of a doped-silicon series-coupled four-ring Vernier filter is demonstrated.

The unwanted spectral shifts in silicon microring-based systems, due to temperature and fabrication variations [1], can be mitigated by implementing automatic tuning and stabilization techniques. This can be achieved using feedback loops, which require sensing of the resonance conditions and tuning the resonators until the desired resonance conditions are met. Typically, while the sensing operation can be accomplished using various detection methods, separate electro-optic or thermo-optic tuners are required for tuning [1-3]. However, using separate elements for the sensing and tuning operations does not scale well to systems with large numbers of rings, due to the increase in footprint, number of electrical contacts, and fabrication cost. In some cases (e.g., series-coupled resonators), the resonance conditions of all of the resonators in a system cannot be readily determined from the system's outputs alone. Such instances may require multi-dimensional optimization algorithms [3], which could increase the time required to reach the desired resonance conditions.

In-resonator photoconductive heaters (IRPHs) can provide a solution. IRPHs are doped resistive heaters integrated into silicon optical resonators. IRPHs have photodetection capabilities, due to defect-state-absorption, and show high responsivities [4]. Using IRPHs, we demonstrated automatic tuning and stabilization of one-ring and two-ring filters [4] as well as the tuning of a two-ring Vernier filter to all of the ITU channels (200 GHz spacing) in the C-band [5]. In [6], we demonstrated a thermally tunable four-ring Vernier filter with attractive spectral features for WDM applications. In [4], we showed that IRPHs can be used to automatically find the desired filter response of a series-coupled filter by tuning the resonators sequentially, starting with the resonator coupled to the input-bus. We tune each resonator by maximizing the photocurrent measured by the resonator's IRPH. Importantly, this algorithm scales linearly with the number of series-coupled resonators. In this paper, we use this method to automatically tune a four-ring Vernier filter.

A micrograph of a fabricated series-coupled four-ring Vernier filter is shown in Fig. 1(a). The silicon rib waveguides (rib height = 220 nm, slab height = 90 nm) in the resonators were *n*-doped to form the IRPHs. These IRPHs are shown as resistors in Fig. 1(a). Here, the different path lengths of the rings set the free spectral range (FSR) of the device (37.21 nm) to be wider than the C-band. Since the IRPHs carry both heater-currents and photocurrents, a calibration step was first performed to measure the heater-currents with the laser input turned off. Fig. 1(b) shows the photocurrents measured after setting the laser input to an ITU wavelength of 1536.61 nm and sweeping the power applied to the IRPHs in Rings 1-4 (sequentially). Here, the photocurrent of each IRPH was calculated by subtracting the pre-calibrated heater-

current from the total measured current [4]. At the end of each sweep, the voltage of the corresponding IRPH was set to the value that maximized its photocurrent. For illustration purposes, here we have chosen to sweep the heater powers. However, in practice, a simple maximum search algorithm can be used to find the maximum photocurrents [4]. A further optimization step was applied after each sweep to adjust for any shifts in the resonances of the previously tuned rings due to thermal crosstalk. The through- and drop-port spectra after completing the tuning and the optimization steps are shown in Figs. 1(c) and (d).

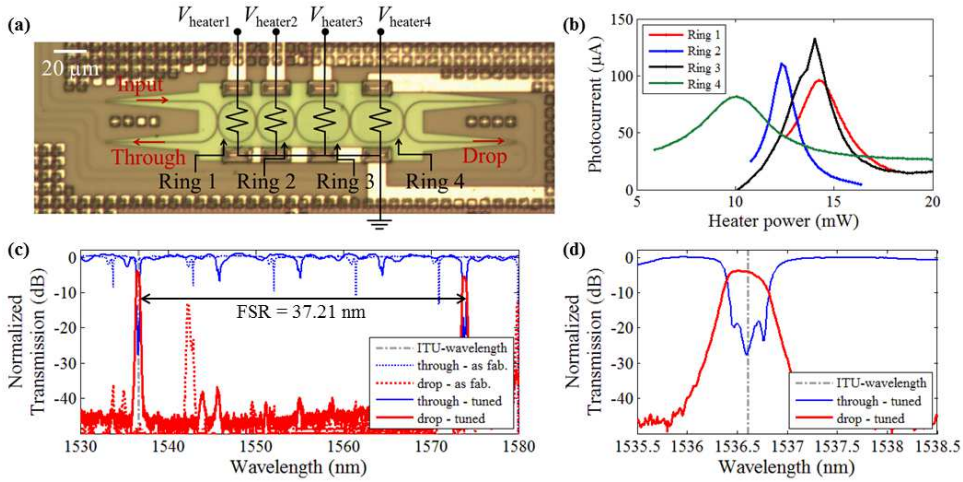



**Fig. 1. (a) Micrograph of a fabricated silicon four-ring Vernier filter. (b) Photocurrents measured in the IRPHs during the tuning process. (c) Normalized through- and drop-port spectra as fabricated and after automatically tuning filter to ITU channel at 1536.61 nm. (d) Zoomed-in spectra near the ITU wavelength after tuning.**

In summary, we have demonstrated automatic tuning of a four-ring series-coupled Vernier filter. The tuning was achieved without compromising the area or cost efficiency of the device and using methods that scale linearly with the number of series-coupled resonators. Our results suggest that IRPHs can be used for automatic tuning and stabilization of silicon photonic microring-based circuits with many resonators.

**Acknowledgements**
We thank Kyle Murray, Michael Caverley, and Miguel Guillén-Torres for their help, the Natural Sciences and Engineering Research Council of Canada for financial support, CMC microsystems for providing access to fabrication and design tools, and the OpSIS MPW program for fabrication.

**References**

[1] K. Padmaraju, K. Bergman, *Resolving the thermal challenges for silicon microring resonator devices*, Nanophotonics, vol. 3, no. 4–5, pp. 269–281, 2014.
[2] S. Saeedi, A. Emami, *Silicon-photonic PTAT temperature sensor for micro-ring resonator thermal stabilization*, Opt. Express, vol. 23, no. 17, pp. 21875-21883, 2015.
[3] J. C. C. Mak et al., *Automatic resonance alignment of high-order microring filters*, IEEE J. Quantum Electron., vol. 51, no. 11, pp. 1-11, 2015.
[4] H. Jayatilleka et. al, *Wavelength tuning and stabilization of microring-based filters using silicon in-resonator photoconductive heaters,* Opt. Express, vol. 23, no. 19, pp. 25084–25097, 2015.
[5] H. Jayatilleka et. al, *Automatic wavelength tuning of series-coupled Vernier racetrack resonators on SOI*, Optical Fiber Communications Conference (OFC), 2016.
[6] R. Boeck et. al, *Thermally tunable quadruple Vernier racetrack resonators*, Opt. Lett., vol. 38, no. 14, pp. 2440-2442, 2013.

ECIO 2016
18TH EUROPEAN CONFERENCE ON INTEGRATED OPTICS 2016
18–20 MAY | WARSAW | POLAND

# Prospects for InP-based integrated photonics

**Meint K. SMIT**
COBRA Research Institute, Eindhoven University of Technology, The Netherlands

Photonic Integration is making rapid progress. InP PICs play an increasingly important role in telecommunications and data communications, and novel applications are emerging in other fields, like fibre sensing technology, medical diagnostics and metrology. InP-based foundry processes offer low-cost access to mature integration processes with high performance, and wafer-scale integration of InP-based photonic circuits with silicon electronics is emerging. In the presentation an overview will be given of recent developments with emphasis on future prospects.

*Long abstract not available at the date of final printing.*

ECIO 2016
18TH EUROPEAN CONFERENCE ON INTEGRATED OPTICS 2016
18–20 MAY | WARSAW | POLAND

# Plasmonics - a Technology for Microscale High-Speed Integrated Optics

**Juerg LEUTHOLD*, Wolfgang HENI, Claudia HOESSBACHER, Christian HAFFNER, Yannick SALAMIN, Ueli KOCH, Yuriy FEDORYSHYN, Romain BONJOUR, Arne JOSTEN, Benedikt BAEUERLE, David HILLERKUSS, Christian HAFNER**
ETH Zurich, 8091 Zurich, Switzerland
* JuergLeuthold@ethz.ch

Plasmonics is increasingly attracting the attention of the optical community [1-4]. The new field promises novel ultra-compact devices in combination with speed only limited by the RC constants of the attached driver circuits. This talk will review key aspects of plasmonics and will discuss opportunities and challenges of plasmonic communications.

Plasmonic communication is an emerging field that promises the generation, processing, transmission, sensing and detection of signals at optical frequencies along a surface of a tiny metal. The term “plasmonics” has been brought to the spotlight by H.A. Atwater and other pioneers in anticipation for an entirely new class of devices with ultra-compact dimensions operating up to highest bandwidths. Meanwhile more than 50’000 scientific articles pop up when searching the web for “plasmonics”.

In the field of plasmonics it is not photons that carry the information but mostly surface plasmon-polaritons (SPPs). SPPs are electromagnetic waves coupled to charge density oscillations at the interface between a material of negative and a material of positive permittivity (e.g., a metal and an insulator, respectively). These electrons then oscillate at said optical frequency. In plasmonics the signal processing is performed on the SPP rather than the photons. After signal processing has been performed the SPPs are converted back to the optical domain.

While plasmonics is not a solution to all integrated optical applications, plasmonics has a strong case for devices

- Featuring active functionalities such as phase and amplitude modulation
- That require ultra-compact size
- That rely on ultra-fast speed and
- That should operate across a broad spectral operation

Challenges that plasmonics has to deal with are

- High losses and
- High resolution in fabrication

Plasmonics thus is a case for active devices with tight requirements on the footprint that need to operate at highest speed.

To keep losses low, plasmonic devices should be as compact as possible. I.e. if active photonic components are used they should feature the largest possible nonlinearity such that operations can be performed in micrometer rather than in millimetre long devices. Fortunately, plasmonics helps in achieving high nonlinearities. This is because plasmonic modes can be confined to dimensions way below diffraction limit and thereby increase nonlinear efficiencies. Another challenge are the lithographic resolutions needed to fabricate plasmonic structures. Feature sized below 20 nm are often needed. Currently, this is the domain of electron-beam lithography – a technology that scales poorly but that may soon be replaced by the next generation of scalable

extreme UV lithography.

As an example we discuss the plasmonic Mach-Zehnder modulator depicted in Fig. 1, [5]. The modulator comprises of three sections. In a first section the photonic mode is converted into a plasmon and mapped onto two plasmonic modes that propagate to the left and to the right of metallic signal electrodes. In section 2, the electrodes not only guide the gap plasmons but also form the ground-signal-ground electrodes of a the modulator. Upon applying a voltage onto the signal electrode the refractive indices of the nonlinear electro-optic material in the gap changes. Finally, in the output of section 3 the plasmons are converted back into a photonic mode and - depending on the relative phase-relations - mapped back onto the subsequent silicon wire waveguide or radiated off due to destructive interference. The whole plasmonic waveguide is only 10 □m in length and has been shown to operate up to 72 Gbit/s [5]. More recently we have introduce a plasmonic IQ-modulator [6] or demonstrated 100 Gbit/s operation [7]. Also multiple plasmonic modulators have been assembled to form an array on a very dense space for optical interconnect applications [8].

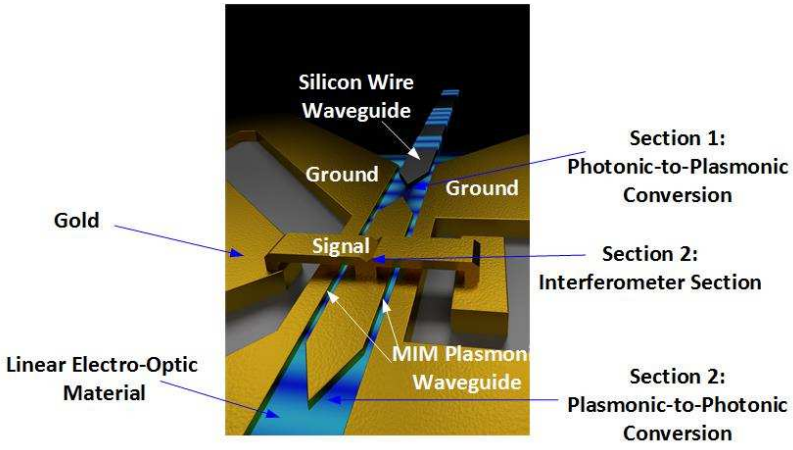



**Fig. 1. Plasmonic Mach-Zehnder modulator. The plasmonic interferometer is formed by the metallic island and the metallic contact pads. An electrical signal can be applied to the island via a suspended bridge. [5].**

We acknowledge support by the ERC grant PLASILOR (EU-670478) and the joint Japan-EU project FF-Photon for partial funding.

[1] H. A. Atwater, "The Promise of Plasmonics," *Scientific American,* vol. 296, p. 56.62, 2007.
[2] D. K. Gramotnev and S. I. Bozhevolnyi, "Plasmonics beyond the diffraction limit," *Nat Photon,* vol. 4, pp. 83-91, 2010
[3] M. L. Brongersma and V. M. Shalaev, "The Case for Plasmonics," *Science,* vol. 328, pp. 440-441, 2010.
[4] J. Leuthold, *et al.* ; Plasmonic Communications - LIGHT ON A WIRE. *Optics & Photonics News*. 28-35. May 2013
[5] C. Haffner, *et al.*, "All-plasmonic Mach–Zehnder modulator enabling optical high-speed communication at the microscale," *Nature Photonics,* vol. 9, pp. 525-528, Aug. 2015.
[6] C. Haffner, W. Heni, Y. Fedoryshyn, B. Baeuerle, A. Josten, Y. Salamin, *et al.*, "Ultra-compact plasmonic IQ-modulator," in *European Conference on Optical Communication (ECOC)*, 2015, pp. 1-3.
[7] W. Heni, *et al.*, "108 Gbit/s Plasmonic Mach-Zehnder Modulator with > 70-GHz Electrical Bandwidth," *Journal of Lightwave Technology,* vol. 34, pp. 393-400, 2016.
[8] C. Hoessbacher, *et al.*, "Optical Interconnect with Densely Integrated Plasmonic Modulator and Germanium Photodetector Arrays," in *Optical Fiber Communication Conference*, Anaheim, California, 2016, p. Th1F.6.

ECIO 2016
18TH EUROPEAN CONFERENCE ON INTEGRATED OPTICS 2016
18–20 MAY | WARSAW | POLAND

# Monolithically integrated coupled-cavity quantum cascade lasers

**M. BUGAJSKI[1], K. PIERŚCIŃSKI[1], D. PIERŚCIŃSKA[1], P. GUTOWSKI[1], I. SANKOWSKA[1], O. SEREBRENNIKOVA[1], P. KARBOWNIK[1], M. PLUSKA[1], A. CZERWINSKI[1], M. KUC[2], R. SARZAŁA[2], T. CZYSZANOWSKI[2], G. HAŁDAŚ[3], A. KOLEK[3]**

[1]Institute of Electron Technology, Al. Lotników 32/46, 02 668 Warsaw, Poland
[2]Institute of Physics, Łódź University of Technology, Wólczańska 219, 90 924 Łódź, Poland
[3]Department of Electronics, Rzeszów University of Technology, W. Pola 2, 35 959 Rzeszów, Poland
* bugajski@ite.waw.pl

Single mode, room-temperature quantum cascade lasers emitting in the 9.5 μm range have been produced by focused ion beam (FIB) etching. Modification of the resonator geometry by dividing the cavity into two sections separated by a small gap, of the order of emission wavelength, results in strong optical coupling of the sections and consequently leads to a strong modification of spectral properties of the emitted radiation. Additional possibilities of influencing the mode structure of coupled-cavity quantum cascade laser (CC QCL) are provided by the feasibility of independent current injection into each section. The long section provides gain and can be operated in pulse or continuous mode. The short section provides the possibility to fine tune its refractive index, through injection of carriers. The stable, single mode emission was observed within temperature tuning range, with a side mode suppression ratio of 43 dB. The paper will review our recent results on design, technology and fabrication of GaAs and InP based mid-IR CC QCLs. We will also discuss a new type of two section, coupled-cavity QCLs with monolithically integrated heater (CC IH QCL), designed for extended temperature tuning.

ECIO 2016
18TH EUROPEAN CONFERENCE ON INTEGRATED OPTICS 2016
18–20 MAY | WARSAW | POLAND

# Sol-gel derived rib waveguides for evanescent wave spectroscopy

**Cuma TYSZKIEWICZ*, Paweł KARASIŃSKI, Roman ROGOZIŃSKI**
Department of Optoelectronics, Silesian University of Technology, ul. B. Krzywoustego 2, Gliwice, 44-100, Poland
* cuma.tyszkiewicz@polsl.pl

Planar evanescent wave sensors (EWS) are important tools for detection of the presence of (bio)chemical compounds as well as for studying kinetics of biochemical reactions [1]. Planar EWS have wide application spectrum including: biomedicine, pharmaceutical industry, biotechnology, diagnostics as well as in-situ environmental monitoring. Planar EWS offer high sensitivities, reliability, stability of their parameters, mechanical resistance, ability for miniaturization and mass production [1]. Achievement of high sensitivities is conditioned by application of waveguides having high refractive index contrast [2]. Achievement of EWS parameters stability is conditioned by application of chemically resistant waveguide films [3]. Slab or channel waveguides are used for development of planar EWS [1]. Channel waveguides are fundamental elements of planar interferometric EWS structures.

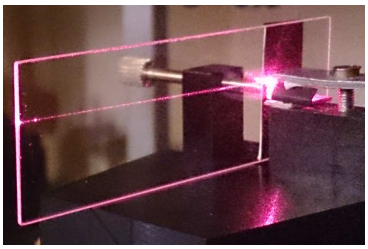


**Fig. 42. Image of excited slab $SiO_2$:$TiO_2$ waveguide on BK7 glass substrate (26×76×1 mm³).**

The rib waveguides fabricated using sol-gel derived $SiO_2$:$TiO_2$ waveguide films, optical contact photolithography and chemical etching, are the subject of our presentation. These waveguide films, whose fabrication technology has been developed in our research group, are characterized by high refractive index (~1.81), homogeneity, very high smoothness, chemical resistance and stability of their parameters over long time period [4]. In our technological route, sol films are deposited on glass substrates using a dip-coating technique. In the Fig. 1, there is presented an image of the excited slab $SiO_2$:$TiO_2$ waveguide fabricated on a BK7 glass substrate. One can see the narrow streak of scattered light which proves high homogeneity of this waveguide film. We are able to fabricate $SiO_2$:$TiO_2$ waveguide films having both: thickness a little higher than cut-off thickness and attenuation lower than 0.2 dB/cm for $\lambda$=677 nm.

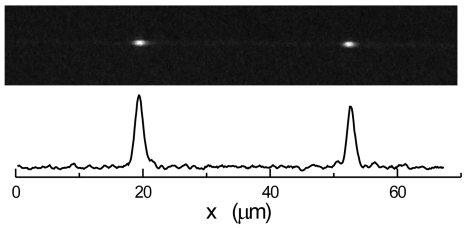



**Fig. 2 Near-field picture of a 1×2 directional couplers outgoing rib waveguides and related distributions of optical power. $\lambda$=677 nm, waveguide high $h$=219 nm, rib width w=2 μm, rib high $t$=6 nm, rib separation $s$=1.5 μm, coupler length $L$=1.5 mm.**

The elaborated technological route is composed of the following, subsequent stages: deposition of a photoresist film on a $SiO_2$:$TiO_2$ waveguide film using a spin-coating method, hardening of the photoresist film by curing, selective UV exposure of the structure throughout a positive photolithographic mask, developing and hardening of a pattern reproduced in the photoresist, chemical etching and removal of the photoresist. The in this way fabricated optical channel structures: rib waveguides and directional couplers, were theoretically analyzed using commercial solver FIMMWAVE 6.1 [5]. The results of theoretical analysis allowed design of single modal channel structures. The near-field picture of outgoing rib waveguides of a 1×2 directional coupler as well as related distributions of optical power are show in Fig.2. We have achieved to fabricate rib waveguides having optical losses of ~1.5 dB/cm [6]. A scattering on rib sidewalls is their main source, so they can be decreased by decreasing a roughness of rib sidewalls.

Elaborated rib waveguide structures are suitable for application in fabrication technology of planar interferometric EWS.

This work was supported by the National Science Centre on the basis of decision DEC-2011/03/B/ST7/03538.

References

[1] P. Kozma, F. Kehl, E. Ehrentreich-Förster, C. Stamm, F.F. Bier, *Integrated planar optical waveguide interferometer biosensors: A comparative review*. Biosensors and Bioelectronics, vol. 58, pp. 287–307, 2014
[2] P. Karasiński, R. Rogoziński, *Characterization and sensor properties of sol-gel $SiO_2$:$TiO_2$/ion-exchange glass waveguide*, Opt. Commun. vol. 281, pp. 2472-2480, 2008
[3] J.J. Ramsden, *Review of new experimental techniques for investigating random sequential adsorption*, J. Stat. Phys., vol. 73, pp. 853-877, 1993
[4] P. Karasiński, C. Tyszkiewicz, A. Domanowska, A. Michalewicz, J. Mazur, *Low loss, long time stable sol-gel derived silica-titania waveguide films*, Mater. Lett. Vol. 143 pp. 5-7, 2015
[5] C. Tyszkiewicz, P.Karasiński, R.Rogoziński, *Directional couplers fabricated via a sol-gel route and conventional optical lithography*, Opt. Quant. Electron, vol. 48, paper 19, 2016
[6] P. Karasiński, C. Tyszkiewicz, R. Rogoziński, J. Jaglarz, J. Mazur, *Optical rib waveguides based on sol-gel derived silica-titania films*, Thin Solid Films vol. 519 pp.5544-5551, 2011

ECIO 2016
18TH EUROPEAN CONFERENCE ON INTEGRATED OPTICS 2016
18–20 MAY | WARSAW | POLAND

# Integrated optical time division reflectometer

**Stanisław STOPIŃSKI*[1], Krzysztof ANDERS[1], Marcin LELIT[1], Luc AUGUSTIN[2] and Ryszard PIRAMIDOWICZ[1]**
[1]Institute of Microelectronics and Optoelectronics, Warsaw University of Technology, Koszykowa 75, 00-662 Warszawa, Poland
[2]SMART Photonics B.V., Horsten 1, 5612 AX Eindhoven, The Netherlands
*S.Stopinski@imio.pw.edu.pl

An optical time domain reflectometer (OTDR) is a device commonly used for testing and monitoring of fiber-optic networks of every kind [1,2]. Despite significant progress in the field, it should be noted that contemporary devices are typically bulky, comprising discrete optoelectronic components and designed for monitoring of a single optical fiber link only. In this work we propose two application specific photonic integrated circuits (ASPICs) designed and developed for a novel OTDR system, which combines the advantages of compactness and multi-channel operation.

The first ASPIC is a single channel reflectometer and its scheme is presented in Fig. 1. Probing light pulses are generated by means of direct modulation of the DFB laser, while detection of the backscattered and reflected light is performed by a photodiode. The chip input/output is connected to the source and the detector through a 2×2 MMI coupler. Fig. 1 presents also a microscope photograph of the device (dimensions 6 mm × 4 mm) fabricated in a generic process provided by Heinrich Hertz Institute [3].

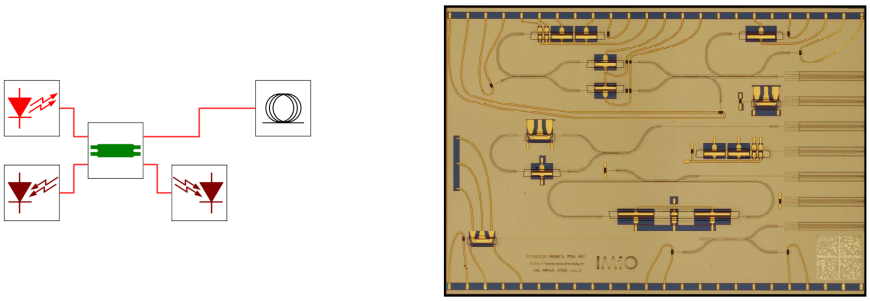


**Fig. 1. Integrated OTDR – circuit scheme (left) and microscope photograph of the fabricated ASPIC (right).**

ASPIC characterization was performed using the measurement setup presented in Fig. 2. The DFB laser was driven through a bias-tee from a pulse generator and a source-measure unit. The photodiode was reversely biased and the voltage signal from the resistor was visualized on the oscilloscope. Fig. 3 presents recorded time traces obtained after launching optical pulses (1 μs pulse duration, 4 kHz repetition rate) to an optical fiber link of a total length of 5 km, 10 km and 20 km. The backscattered signal was too weak to be detected directly on the resistor. However, the reflections from the end of the fiber link were detected and the value of the time delay was coherent with the length of the link.

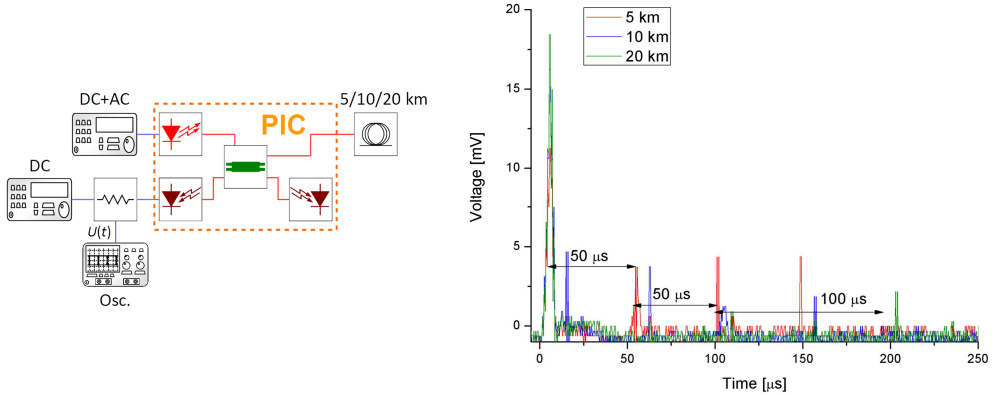



**Fig. 2. Measurement setup used for characterization of a single channel integrated OTDR (left) and recorded time traces (right)**

The second ASPIC, realized in the generic process of SMART Photonics [3], is a multi-channel reflectometer. Fig. 3. presents a scheme of a two-channel photonic circuit, which comprises Fabry-Perot lasers as light sources, combined with amplifiers to boost the output power. The lasers can be either directly or externally modulated using a Mach-Zehnder modulator. The optical signal is coupled to two optical IOs through a cascade of MMI couplers. The fabricated chip (dimensions 4.6 mm × 4 mm) is presented in Fig. 3.

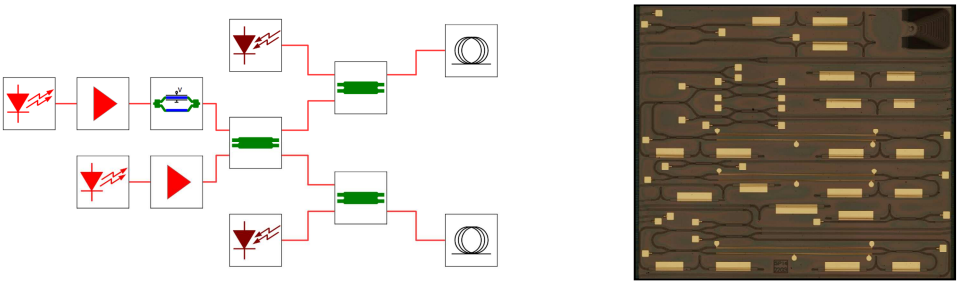


**Fig. 3. Multi-channel integrated OTDR – circuit scheme (left) and microscope photograph of the fabricated ASPIC (right).**

As a result of this work two integrated OTDR photonic integrated circuits were designed and fabricated using generic foundry processes. Initial characterization results confirm the potential and applicability of the photonic integration technology for this application.

This work has been supported by the statutory funds of the Faculty of Electronics and Information Technology of Warsaw University of Technology.

References

[1] S. D. Personick, “Photon probe-An optical-fiber time-domain reflectometer”, Bell Syst. Tech. J., vol. 56, no. 3 , pp. 355-366, 1977.
[2] E. Brinkmeyer, “Backscattering in single-mode fibers”, Electron. Lett., vol. 16, no. 9, pp. 329-330, 1980.
[3] M. Smit, et al., “An introduction to inp-based generic integration technology,” Semiconductor Science and Technology, vol. 29, no. 8 p. 083001 (2014)

ECIO 2016
18TH EUROPEAN CONFERENCE ON INTEGRATED OPTICS 2016
18–20 MAY | WARSAW | POLAND

# Lossy Metallic Micro/Nano-Structures for Solar Thermal Applications

**S. NÚÑEZ-SÁNCHEZ[1*], E. BAQUEDANO-PERALVAREZ[2], J. PUGH1, P. A. POSTIGO[2], N.A. FOX[3] and M. J.CRYAN[1]**

[1]Department of Electrical and Electronic Engineering, University of Bristol, Bristol BS8 1TR, U. K.
[2]Instituto de Microelectrónica de Madrid, Spanish National Research Council, Madrid, Spain.
[3]School of Chemistry, CVD Diamond Group, University of Bristol, Bristol BS8 1TL, UK.
[*] S.Nunez-Sanchez@bristol.ac.uk

Research on controlling heat in photonic devices has been fuelled by their potential application in energy devices, mainly in solar energy[1]–[3]. In this environment thermionic emission is an emerging technology where energy converters turn heat directly into electricity. The basic thermionic solar converter structure is a hot cathode separated from a cooler anode by a vacuum gap. The hot cathode should be a perfect light absorber and a perfect electron emitter in a compact, low cost, planar device. The final objective of our work is to integrate a thermionic solar-energy converted based on polycrystalline diamond as an active material. Diamond thermionic solar converters require substrates with excellent high temperature performance since they have to operate continuously at temperatures around 900 ˚C. Noble metals are an excellent platform for plasmonic applications, however they have a poor performance at high temperatures with melting points close to the working temperature. Therefore our main design requirement for the viability of our integrated device is to work with unconventional metals with higher melting points than noble metals, for example, nickel or molybdenum.

We have already shown that lossy nickel periodic structures are a good candidate to excite plasmons in the visible with high attenuation of the coupled light obtaining broadband absorbers.[4], [5] In this paper we have developed a large area preparation technique based on nanoimprint technology using commercial DVD and CD patterns to create periodic nickel structures. Homogenous samples with an area of 1cm$^2$ have been obtained and are shown in Figure 1(a). The optical angular response of the samples has been characterized in our in-house Fourier microscope, shown in Figure 1(b). As we expect from Finite Difference Time Domain (FDTD) simulations the optical properties of the samples depend strongly on the period and the morphology of the grating channels .[5] Figure 1(b) shows reasonably good broad band absorptance, this is currently being limited by the nanoimprint process not achieving sufficiently deep grooves.

Molybdenum is a refractory metal with an even higher melting point than nickel (above 2000 °C) which is often used for industrial applications. It has not yet been explored for applications in the visible range, firstly due to its high losses and, secondly, the inability to couple to surface plasmons due to its optical properties. However, molybdenum does have a large value for the imaginary part of the permittivity, making it an excellent candidate to produce high losses through Joule heating. Under these conditions we have developed a new design approach where molybdenum acts as a very lossy dielectric instead of a metal. Large samples have been laser etched with large period structures with periods around 10μm. Figure 1(c) shows and optical image under polarized white light and excellent black metal properties are observed.

The final objective of this work is to optimize the response of nano/micro patterned metal absorbers based on plasmonic metals and lossy dielectrics and combine them with a large area fabrication techniques to produce low cost solar-thermionics energy converters.

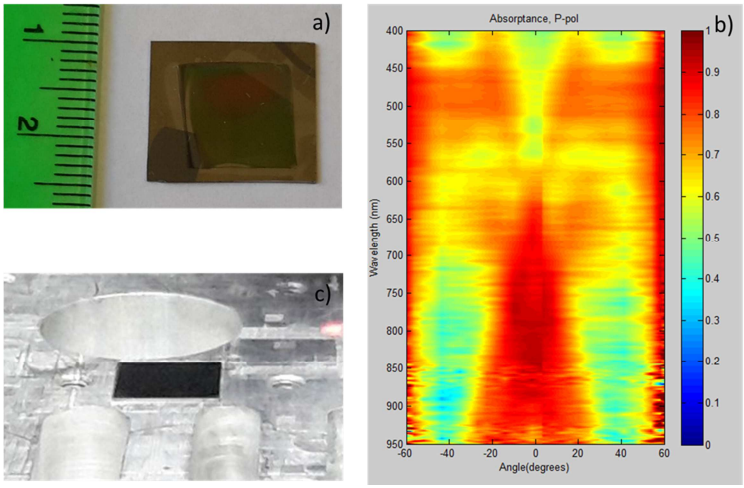



**Fig. 45. (a) Photograph of a nickel periodic nanostructure prepared from nanoimprint lithography with a commercial CD mask.**
**(b) Angular response of the nickel sample of Figure 1.a.**
**(c) Image of a molybdenum patterned sample under linear polarized white light.**

References

[1] A. Lenert, D. M. Bierman, Y. Nam, W. R. Chan, I. Celanovic, and E. N. Wang, "A nanophotonic solar thermophotovoltaic device," *Nat. Nanotechnol.*, vol. 9, no. January, pp. 126–130, 2014.
[2] K. a Arpin, M. D. Losego, A. N. Cloud, H. Ning, J. Mallek, N. P. Sergeant, L. Zhu, Z. Yu, B. Kalanyan, G. N. Parsons, G. S. Girolami, J. R. Abelson, S. Fan, and P. V Braun, "Three-dimensional self-assembled photonic crystals with high temperature stability for thermal emission modification.," *Nat. Commun.*, vol. 4, p. 2630, Jan. 2013.
[3] A. Polman, "Solar steam nanobubbles.," *ACS Nano*, vol. 7, no. 1, pp. 15–8, Jan. 2013.
[4] N. Ahmad, J. Stokes, N. a. Fox, M. Teng, and M. J. Cryan, "Ultra-thin metal films for enhanced solar absorption," *Nano Energy*, vol. 1, no. 6, pp. 777–782, Nov. 2012.
[5] N. Ahmad, J. Stokes, and M. Cryan, "Solar absorbers using 1D and 2D periodic nanostructured nickel films," *J. Opt.*, vol. 16, no. 12, p. 125003, 2014.

ECIO 2016
18TH EUROPEAN CONFERENCE ON INTEGRATED OPTICS 2016
18–20 MAY | WARSAW | POLAND

# Near-stoichiometric Ti:D:$LiNbO_3$ (D = $Mg^{2+}$, $Sc^{3+}$, $Ga^{3+}$, $Zr^{4+}$) Optical Waveguides for Integrated Optics

**De-Long Zhang[1,2*], Xiao-Fei Yang[1], Wing-Han Wong[2], Edwin Yue-Bun Pun[2]**
[1] School of Precision Instruments and Opto-electronics Engineering, Tianjin University, Tianjin 300072, China, and Key Laboratory of Optoelectronic Information Technology (Ministry of Education), Tianjin University, Tianjin, 300072, China.
[2] Department of Electronic Engineering and State Key Laboratory of Millimeter Waves, City University of Hong Kong, Kowloon, Hong Kong SAR, China.
[*] dlzhang@tju.edu.cn

Near-stoichiometric (NS) Ti:D:$LiNbO_3$(D=$Mg^{2+}$, $Sc^{3+}$, $Ga^{3+}$, $Zr^{4+}$) strip waveguides were fabricated by D-diffusion-doping, Ti-diffusion and post vapor-transport-equilibration. We exemplify Ti:Zr:$LiNbO_3$ to demonstrate its implementation. We show that the waveguide is NS, well supports both TE and TM single-modes, and $Zr^{4+}$ concentration in the waveguide is above optical-damage threshold.

$LiNbO_3$ (LN)-based devices suffer from the photorefractive effect, which limits both pumping and operating wavelengths and hence hinders development of novel devices. Low threshold concentration of photorefractive-damage-resistant dopant is desired. A near-stoichiometric (NS) LN doped with higher than 0.8 mol% $Mg^{2+}$ [1], 0.4 mol% $Sc^{3+}$ [2], 0.5 mol% $Ga^{3+}$ [3] or only 0.085 mol% $Zr^{4+}$ [4] has been shown to effectively suppress the photorefractive effect. An NS Ti:D:LN (D = $Mg^{2+}$, $Sc^{3+}$, $Ga^{3+}$, $Zr^{4+}$) waveguide is more promising than a congruent one. Here, we exemplify the Ti:Zr:LN one to demonstrate the implantation of such waveguide.

The NS Ti:Zr:LN waveguide was fabricated starting from a congruent LN with a technological process in sequence of $Zr^{4+}$-diffusion doping, Ti diffusion and post Li-rich vapor-transport-equilibration(VTE). A 100±2 nm thick $ZrO_2$ film was coated onto surface part of a commercial Z-cut congruent LN plate, followed by an anneal at 1060 °C for 10 h. Then, an array of 200-μm-separated Ti strips with a width 8 μm and a thickness 100±2 nm were delineated on the $Zr^{4+}$-diffused surface, followed by an anneal at 1060 °C for 10 h and the subsequent Li-rich VTE at 1100 °C for 10 h.

The material composition in the waveguide layer was roughly evaluated from the refractive index measured at the undoped surface part of the sample and on the basis of the $Li_2O$-content-dependent Sellmeier equation. The result shows that the waveguide is in an NS environment. The end-fire experiment shows that the waveguide well supports both TE and TM single-modes at 1.5 μm wavelength as shown in Fig. 1(a). Analysis shows the light intensity of the guided mode follows a Gauss function $A_x\exp[-2(x/W_x)^2]$ in the width direction x and a Hermite-Gauss function $A_y y^2\exp[-2(y/W_y)^2]$ in the depth direction y. The TE mode size ($W_x \times W_y$ =4.7 × 4.9 $\mu m^2$) is similar to the TM mode size ($W_x \times W_y$ = 4.7 × 4.8 $\mu m^2$). From the measured insertion loss, reflection loss and the coupling loss evaluated from the known mode size, the waveguide loss was evaluated as 0.6/0.8 dB/cm for the TE/TM mode. Fig. 1(b) shows the $Ti^{4+}$ profile on the waveguide surface.

ECIO 2016
18TH EUROPEAN CONFERENCE ON INTEGRATED OPTICS 2016
18–20 MAY | WARSAW | POLAND

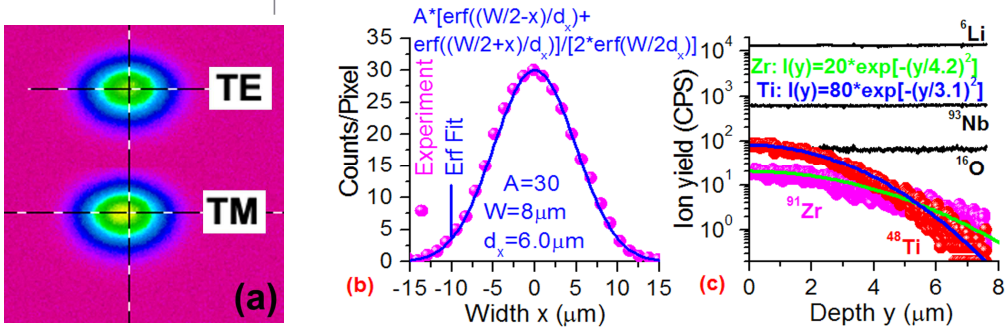



**Fig. 1. (a) Mode images at 1.5 μm wavelength, (b) Surface Ti profile and (c) depth profiles of Li, Nb, O, Zr and Ti in 8-μm-wide NS Ti:Zr:LN waveguide.**

Fig. 1(b) shows the depth profiles of $^{6}Li$, $^{93}Nb$, $^{16}O$, $^{91}Zr$ and $^{48}Ti$ in the waveguide. The fitting results show that the Ti ions on the waveguide surface follows a sum of two error functions with a diffusion width $d_x$ = 6.0 ± 0.2 μm. Both the $Ti^{4+}$ and $Zr^{4+}$ profiles can be well fitted by a Gaussian function with a diffusion depth $d_{Ti}$ ($d_{Zr}$) = 3.1 ± 0.1 μm (4.2 ± 0.1 μm). The fitting expressions are indicated. From the law of mass conservation, the $Zr^{4+}$ concentration at the waveguide surface was evaluated as 4.2 ± 0.2 mol%, which is ~49 times higher than the optical-damage threshold of NS Zr:LN, $C_{th}$ = 0.085 mol%. Moreover, the $Zr^{4+}$ concentration at the 1/e $Ti^{4+}$ concentration depth is 1.5 mol%, which is ~ 18 times higher than $C_{th}$. In words, the $Zr^{4+}$ concentration in the waveguide is above optical-damage threshold and the waveguide is expected to be optical-damage-resistant.

By using similar method we have also fabricated NS Ti:Mg:LN, Ti:Sc:LN and Ti:Ga:LN strip waveguides. The realization of active and passive NS Ti:(Er:)LN waveguides doped with $Mg^{2+}$, $Sc^{3+}$, $Ga^{3+}$ or $Zr^{4+}$ constructs a technical platform for the development of novel active and passive LN-based devices.

References

[1] Y. Furukawa, K. Kitamura, S. Takekawa, A. Miyamoto, M. Terao, and N. Suda, Photorefraction in $LiNbO_3$ as a function of [Li]/[Nb] and MgO concentrations, Appl. Phys. Lett., vol. 77, no. 16, pp. 2494-2496, 2000

[2] M. Nakamura, S. Takekawa, Y. W. Liu, K. Kitamura, Crystal growth of Sc-doped near-stoichiometric $LiNbO_3$ and its characteristics, J. Crystal Growth, vol. 281, no. 2-4, pp. 549-555, 2005

[3] M. Nakamura, S. Takekawa, Y. W. Liu and K. Kitamura, Use of Ga doping to suppress optical damage in near-stoichiometric $LiNbO_3$ crystals, Jpn. J. Appl. Phys., 48 (2009) 020214 (1-3)

[4] L. Kovács, Z. Szaller, K. Lengyel, Á. Péter, I. Hajdara, G. Mandula, L. Pálfalvi and J. Hebling, "Photorefractive damage resistance threshold in stoichiometric $LiNbO_3$:Zr crystals," Opt. Lett., vol. 38, no. 15, pp. 2861-2864, 2013

ECIO 2016
18TH EUROPEAN CONFERENCE ON INTEGRATED OPTICS 2016
18–20 MAY | WARSAW | POLAND

# Threshold Analysis of 2-D Gain and Index Coupled Photonic Crystal Lasers

**Marcin KOBA[1,2]*, Paweł SZCZEPAŃSKI[1,2]**
[1]Institute of Microelectronics and Optoelectronics, Warsaw University of Technology, Koszykowa 75, 00-662 Warszawa, Poland
[2]National Institute of Telecommunications, Szachowa 1, 04-894 Warszawa, Poland
*M.Koba@elka.pw.edu.pl

In this work we compare threshold mode operation of Index and Gain coupled photonic crystal lasers. The active region of the laser structure consists of two materials - background material with high refractive index and cylindrical rods/holes arranged in square or triangular lattice with low refractive index. It is worth noting that some other rods geometries might be considered in future works, e.g., [1]. For the two structures and two lattices types two orthogonal polarizations, i.e., transverse magnetic and transverse electric, are investigated. From the eight possible cases the most favorable design in terms of lasing threshold is determined. The analysis is based on the coupled mode theory, which gives sets of coupled equations for each of the investigated cases. An exemplary set of equations for square lattice index and gain coupled structure with TM polarization is given by [2,3]:

$$-\frac{\partial}{\partial x}E_1^s + (\alpha - i\delta)E_1^s = (i\eta_3 - \alpha_3)E_3^s + (i\eta_2 - \alpha_2)(E_2^s + E_4^s), \quad (1)$$

$$\frac{\partial}{\partial x}E_3^s + (\alpha - i\delta)E_3^s = (i\eta_3 - \alpha_3)E_1^s + (i\eta_2 - \alpha_2)(E_2^s + E_4^s), \quad (2)$$

$$-\frac{\partial}{\partial y}E_2^s + (\alpha - i\delta)E_2^s = (i\eta_3 - \alpha_3)E_4^s + (i\eta_2 - \alpha_2)(E_1^s + E_3^s), \quad (3)$$

$$\frac{\partial}{\partial y}E_4^s + (\alpha - i\delta)E_4^s = (i\eta_3 - \alpha_3)E_2^s + (i\eta_2 - \alpha_2)(E_1^s + E_3^s), \quad (4)$$

In the above equations $E_i^s$, *i = 1,2,3,4* are the four basic electric field amplitudes propagating in four directions of the photonic crystal cavity, i.e., *+x, -x, +y, -y*. The coupling in the structure is expressed by $\eta_2$ and $\eta_3$. The periodic gain is stated by $\alpha_2$, $\alpha_3$ – which are the higher order gain components, which for Index coupled structure are assumed to be 0, whereas for Index and Gain Coupled structure are assumed nonzero. The gain coefficient $\alpha$ describes a threshold gain in the lasing medium. The coupling coefficients are responsible for orthogonal (e.g., the coupling of $E_1^s$ to $E_2^s$ and $E_4^s$) and backward (e.g., the coupling of $E_1^s$ *to* $E_3^s$) coupling. In equations (1) – (4) the Bragg frequency deviation is given by the following expression:

$$\delta = (\beta^2 - \beta_0^{s2})/2\beta \approx \beta - \beta_0^s. \quad (5)$$

Equations (1) – (4) are solved using the finite difference method with appropriate boundary conditions. Obtained solutions describe each mode by its threshold distributions $E_i^s$, threshold gain, and Bragg frequency deviation.

The calculations are conducted for square and triangular lattices assuming that both have the same filling factor (the fraction of rods area to the structure area) $f$ = 0.16. Here, for the presented case of square lattice it is assumed that $|\eta_2 L|$ = 4.1, and

$|\eta_3 L| = 2$, where L denotes cavity length.

An example solution of equations (1) – (4) showing the behavior of threshold gain in terms of Bragg frequency deviation and coupling coefficient are given in figure 1. Figures 1a shows the comparison of threshold gain for four fundamental modes in case of Index and Gain Coupled structure. Figure 1b depicts (for the mode A) the development and comparison of the threshold gains in a wide range of the coupling coefficient for the Index and Index and Gain Coupled structures.

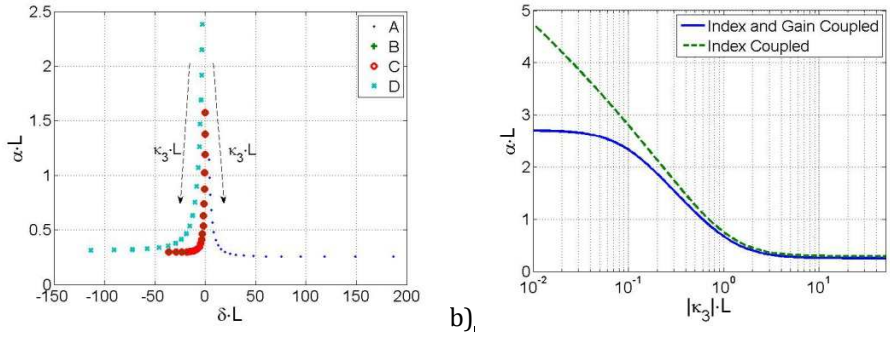



**Fig. 48. Square lattice structure with TM polarization. The dependence of normalized threshold gain versus a) Bragg frequency deviation; and b) normalized coupling coefficient for mode A for Index and Gain Coupled (solid line) and Index Coupled (dashed line) structures [3].**

The outcome shows that the nonuniformity of the gain in the low index contrast structures has a strong impact on the threshold gain, by lowering it. Consequently, by inducing gain coupling in the Index Coupled structure, it is possible to lower threshold gain particularly for low index contrast photonic crystals. The overall analysis shows that the lowest threshold is achieved for the Index and Gain Coupled structures, and it is takes lower values for higher refractive index contrast in case of transverse magnetic polarization. This outcome helps understand the principles of PC band-edge laser operation and it may be useful in supporting the design process of PC laser structures.

References

[1] Y. Liang, C. Peng, K. Sakai, S. Iwahashi, and S. Noda, *Three dimensional coupled-wave analysis for square-lattice photonic crystal surface emitting lasers with transverse-electric polarization: Finite-size effects*, Optics Express, vol. 20, no. 14, pp. 15945-15951, 2012

[2] M. Koba, P. Szczepanski, T. Osuch, *Threshold Mode Analysis of 2-D Square and Triangular Lattice Gain and Index Coupled Photonic Crystal Lasers*, IEEE Journal of Quantum Electronics, vol. 50, no. 7, pp. 554-562, 2014

[3] M. Koba, *Advances in Photonic Crystals,* InTech, Rijeka, 2013

[4] M. Koba, P. Szczepanski, *Photonic Crystals - Introduction, Applications and Theory*, InTech, Rijeka, 2012

ECIO 2016
18TH EUROPEAN CONFERENCE ON INTEGRATED OPTICS 2016
18–20 MAY | WARSAW | POLAND

# Integrated Photonic Lithium-Niobate Electric-Field Sensor utilizing a Y-fed Balanced-Bridge(YBB) Mach-Zehnder Interferometric Modulator

**Hongsik Jung[1*]**
Dept. Electronic & Electrical Eng., Hongik Univ.,
2639, Sejong-ro, Jochiwon, Sejong, 339-701, Korea
hsjun@hongik.ac.kr

We designed, fabricated and characterized a compact and highly sensitive integrated photonic electric-field sensor based on a Ti:$LiNbO_3$ 1×2 YBB-MZI modulator driven by a patch dipole antenna. The modulators have been formed from titanium-diffused lithium Niobate waveguides at the wavelength of 1.3 μm. The YBB-MZI modulator consists of a 3 dB directional coupler at the output and has two complementary output waveguide as shown in Fig. 1(a). For electric-field sensing, a dipole patch antenna arranged on one arm of the MZI structure, as shown in Fig. 1(b) induces the electric-field on one of the two arms of the MZI, which results in a change of refractive index and an unbalanced modulation.

The waveguide width is 7.5 μm and the splitting angle of the Y-branch is 0.6°. The gap width between two adjacent waveguide of the directional coupler is 5 μm and the parallel coupling length $L_c$ is 2.8 mm. The distance between the inner edges of two output waveguides is 50 μm. The length and gap of the modulation electrode connected to the dipole patch antenna are 10 mm and 12 μm.

When no voltage was applied, the optical output powers of the two branches were almost identical. It was observed that the switching voltage applied to modulate the light power of either branch from a bar state (maximum intensity) to a cross state (minimum intensity) was ~16.6 V, corresponding to a light-extinction ratio of ~14.7 dB as shown in Fig. 2(a). The spectrum outputs for input of 20 dBm to the TEM cell at frequencies of 10, 50 and, 70 MHz, respectively have been measured. The measured rf power received at the photo-detector was measured to -101.5, -110.9, and -122.2 dBm, at the frequencies. The noise floor is about -130 dBm. The internal electric-field of 29.8 V/m in the TEM cell produces an SNR of 28.5, 19.1, and 7.8 dB, respectively at the frequencies. Therefore, the minimum detectable electric-fields are ~1.12, ~3.3, and 12.13 V/m, respectively based on $E_{min} = 29.8\times10^{(-SNR/20)}$ V/m at the frequencies.

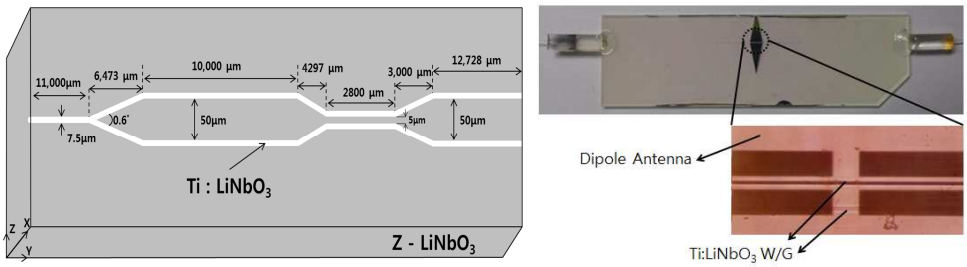
The Fig. 3(a) shows the sensitivity curves at frequencies of 10, 50 and 100 MHz. We can confirm that the graph shows almost linear response for applied electric-field intensity from 0.293 V/m to 23.2 V/m, even though some data were not on the line, yet very close. The device has a dynamic range of about ~22, ~18, and ~12 dB at frequencies of 10, 50, and 100 MHz, respectively. Moreover, the measuring frequency response of the sensor at rf input power of 20 dBm was obtained in the TEM cell, showing almost flat response from 1 MHz to ~50 MHz, as seen in Fig. 3(b).

In conclusion, a 1×2 Y-fed balanced-bridge Mach-Zehnder interferometer which can be used as an integrated-optic electric-field sensor has been presented. Modulators have been formed from titanium-diffused lithium niobate waveguides at the wavelength of 1.3 μm. A dc switching voltage of ~16.6 V and an extinction ratio of ~14.7 dB are measured. For a 20 dBm rf power, the minimum detectable electric-fields are ~1.12

V/m and ~3.3 V/m corresponding to a dynamic range of about ~22 dB and ~18 dB at frequencies 10 MHz and 50 MHz, respectively. The sensors exhibit almost linear response for the applied electric-field intensity from 0.29 V/m to 29.8 V/m.

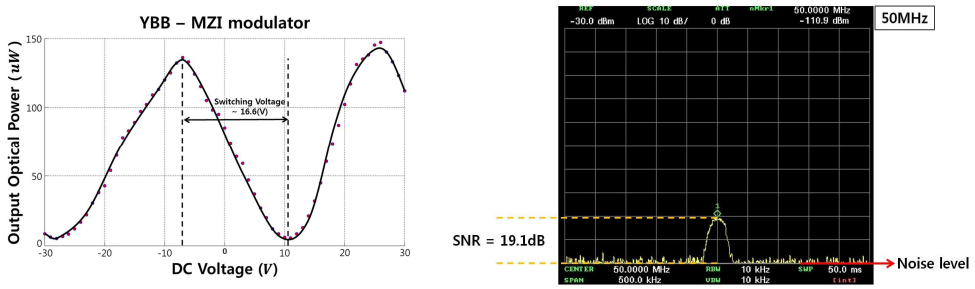
References

[1] H. Jung, *Integrated-Optic Electric-Field Utilizing a Ti:LiNbO₃ Y-fed Balanced-Bridge Mach-Zehnder Interferometric Modulator With a Segmented Dipole Antenna*, Journal of the Optical Society of Korea, vol. 18, no. 6, pp. 739-745, 2014



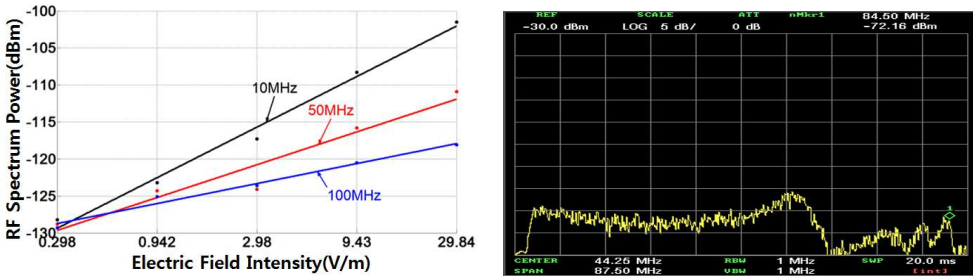

**(a)** **(b)**

**Fig. 1. Schematic diagrams and dimensions of (a) YBB-MZI structure and (b) photograph of fabricated device with dipole patch antenna arrangement and pig-tailed optical fiber.**




**(a)** **(b)**

**Fig. 2. (a) Measured optical output power intensity versus applied dc voltage (b) RF spectrum of 50 MHz input signal with a power level of 100 mW.**




**(a)** **(b)**

**Fig. 3. (a) Photodetected signal power versus electric-field strength at different frequencies (b) the frequency response of the sensor.**

ECIO 2016
18TH EUROPEAN CONFERENCE ON INTEGRATED OPTICS 2016
18–20 MAY | WARSAW | POLAND

# Pareto optimization of group delay response of apodized tapered fibre gratings

**Konrad MARKOWSKI[1], Kazimierz JEDRZEJEWSKI[1], Tomasz OSUCH[1,2*]**
[1]Institute of Electronic Systems, Warsaw University of Technology, Nowowiejska 15/19, Warsaw, 00-665, Poland
[2]National Institute of Telecommunications, Szachowa 1, Warsaw, 04-894, Poland
* T.Osuch@elka.pw.edu.pl

It was proved that practical usage of dispersion properties of chirped FBG requires shaping the envelope of the induced (by the UV exposure) refractive index changes using apodization function to achieve reduction of the oscillations in group delay characteristic [1]. Among many apodization functions, it was shown that hyperbolic tangent (tanh) profile provides better dispersion compensation properties than the others [2,3]. The tanh apodization function may be written as follows:

$$g(z)=\begin{cases}1+\tanh\left\{A\left[1-2\left(1-\frac{2}{L}z\right)^{B}\right]\right\}, z\in\left(0,\frac{L}{2}\right)\\ 1+\tanh\left\{A\left[1-2\left(\frac{2z-L}{L}\right)^{B}\right]\right\}, z\in\left(\frac{L}{2},L\right)\end{cases} \quad (1)$$

where A , B are function parameters and L is the grating length.

Although, the method in fact reduces the oscillations of the group delay response (defined as average peak to peak value of the group delay response), it also results in reduction of the operating bandwidth (defined as spectral width at a relative reference level of -10 dB) of the grating response. It occurs due to the reduction of the effective length of an apodized tapered fibre Bragg grating resulted from decreasing an amplitude of refractive index changes at both grating ends. Thus, in dispersion compensation purposes, simultaneous fulfillment of minimum group delay oscillations and maximum operating bandwidth of apodized FBG are mutually exclusive. Series of simulations were performed to demonstrate dependency between shape of the apodization and spectral width as well as oscillation factor. Results shown in Fig. 1a and Fig. 1b indicate that areas with optimal A and B parameters are located in the opposite end of the presented maps (the upper right corner for maximum spectral width and the area near the bottom left corner for minimum oscillation factor). Thus, such case may be considered as classical optimization problem with two adversative objective functions.

In order to quantitatively solve this problem and find the optimal solution(s) we propose here the use of the Pareto optimization. A solution can be called Pareto optimal (i.e. non-dominated) if no solution in the set are dominated by any other solutions in the set [4]. For analyzed tanh(A,B) apodized TFBG certain constrains has been established: maximum oscillation factor of 4ps and minimum spectral width of 3.6nm. Fig. 2a shows all possible solutions that meet these assumptions, noted in the figure with grey transparent field.

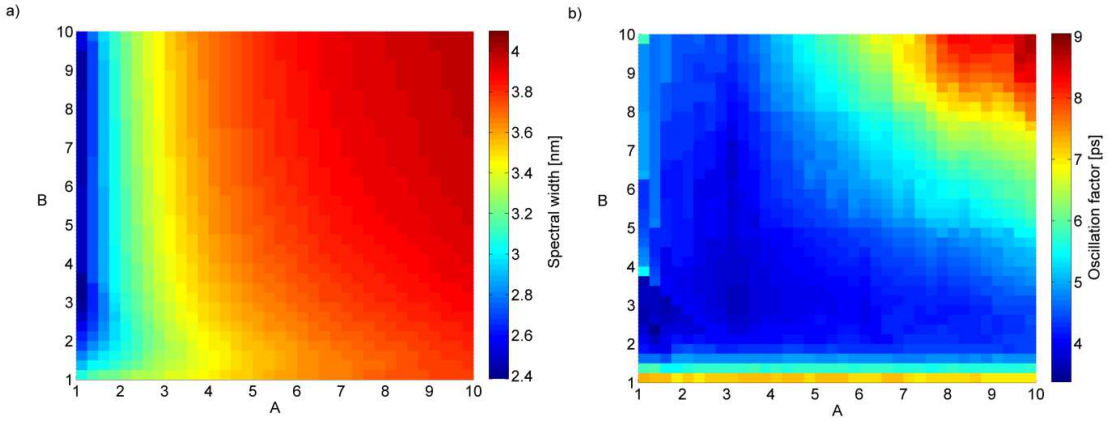



**Fig. 1 Maps of a) spectral width and b) oscillation factor of apodized TFBG reflection and group delay characteristics for various A and B parameters of tanh function**

However, the best, i. e. Pareto optimal, are only three of them, circled in the graph and marked with arrows. Thus, one may summarize, that the best apodization profiles are tanh functions with A and B pairs indicated in Fig. 2a. The group delay response of the optimally apodized (i.e. with A=3 and B=6.2) TFBG is presented in Fig. 2b.

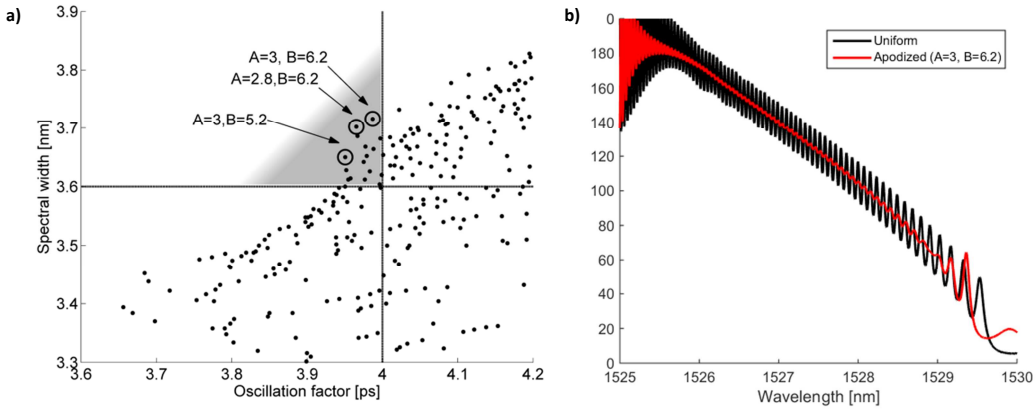



**Fig. 2 Set of the solutions that fulfill established criteria for spectral width and oscillation factor with indicated Pareto frontier.**

References

[1] S. J. Mihailov, et al., *Comparison of fiber Bragg grating dispersion-compensators made with holographic and e-beam written phase masks*, IEEE Photon. Technol. Lett., vol. 11, no. 2, pp. 572–574, 1999.

[2] N. A. Mohammed, M. Solaiman, and M. H. Aly, *Design and performance evaluation of a dispersion compensation unit using several chirping functions in a tanh apodized FBG and comparison with dispersion compensation fiber*, Appl. Opt., vol. 53, no. 29, pp. H239–H247, 2014.

[3] K. Ennser, M. N. Zervas, and R. Laming, *Optimization of apodized linearly chirped fiber gratings for optical communications*, IEEE J. Quantum Electron., vol. 34, no. 5, pp. 770–778, 1998.

[4] J. Horn, N. Nafpliotis and D. E. Goldberg, *A niched Pareto genetic algorithm for multiobjective optimization*, in Proc. IEEE Conf. Evolutionary Computation, pp. 82–87, 1994.

ECIO 2016
18TH EUROPEAN CONFERENCE ON INTEGRATED OPTICS 2016
18–20 MAY | WARSAW | POLAND

# White luminescence in borate and phosphate glasses containing lead

**Marta SOŁTYS[1*], Agnieszka KOS[1], Joanna PISARSKA[1], Wojciech A. PISARSKI[1]**
[1]University of Silesia, Institute of Chemistry, Szkolna 9 Street, Katowice, 40-007, Poland
* martasoltys@interia.pl

Generation of white light has become a challenging task nowadays as the white light-based devices are considered as important components of human electronic interface. To produce white light by conventional way, a blended set of various phosphors are usually used in fluorescent lamps, so that the wavelengths at which the phosphors emit are distributed evenly. Rare earth doped borate and phosphate glasses [1] belonging to wide family of inorganic glass systems could be considered as favorable alternative luminescent materials replacing conventional phosphors for white LEDs due to their some potential advantages such as, lower production cost, simpler manufacturing procedure, homogeneous light emission and better thermal stability. Among various glass host matrices, borate glasses containing lead [2, 3] have attracted considerable attention, because they possess excellent luminescence properties. Different scientific works focused on rare earth-doped glasses have succeeded in generating white light, although co-doping with at least two different rare earth ions ($Ln^{3+}$) is necessary and strongly recommended by several co-workers.

Our previous investigations indicate that lead borates doubly doped with $Dy^{3+}/Tb^{3+}$ and $Tb^{3+}/Eu^{3+}$ [4] are the most important glass systems from the optical point of view. Generally, trivalent $Tb^{3+}$ and $Eu^{3+}$ are incorporated to glass host matrices in order to produce systems emitting two primary color (green and red) light. Glass materials containing terbium ions are known as green emitters, due to $^5D_4 \rightarrow {}^7F_5$ transitions, located at about 543 nm. The second $Ln^{3+}$ ions, i.e. trivalent $Eu^{3+}$ ions are often used as a spectroscopic probe in inorganic glasses. Many glass systems demonstrate intense and efficient red emission at 611 nm associated to the $^5D_0 \rightarrow {}^7F_2$ transition of $Eu^{3+}$. Moreover, quite intense green ($Tb^{3+}$) and red ($Eu^{3+}$) luminescence can be produced under excitation by commercially available UV or blue LED in wide 350 - 490 nm range, where several absorption bands of $Ln^{3+}$ (Ln = Tb, Eu) occur. Such primary (green, red) colors emitting materials are of significant importance in the development of emission rich optical systems. White light generation from the simultaneous emissions of blue, green and red lights under UV-light excitation is possible to obtain in $Tb^{3+}/Eu^{3+}$ glass matrices with the presence of the third component giving blue luminescence, for example $Dy^{3+}$. Thus, these phenomena will be quite well realized in $Dy^{3+}/Tb^{3+}/Eu^{3+}$ triply doped inorganic glasses, which exhibit the ability to address white light as a sum of blue ($Dy^{3+}$), green ($Tb^{3+}$) and red ($Eu^{3+}$) emissions under laser excitation with commercially available solid-state diode lasers.

In this work, we present preliminary results for $Dy^{3+}/Tb^{3+}/Eu^{3+}$ ions in lead borate glasses under different excitation wavelengths. Our investigations clearly indicate that the quite efficient energy transfer processes between rare earth ions in lead borate glass host occur (Fig. 1). The same phenomena were also observed for $Dy^{3+}/Tb^{3+}/Eu^{3+}$ ions in phosphate glasses containing lead.

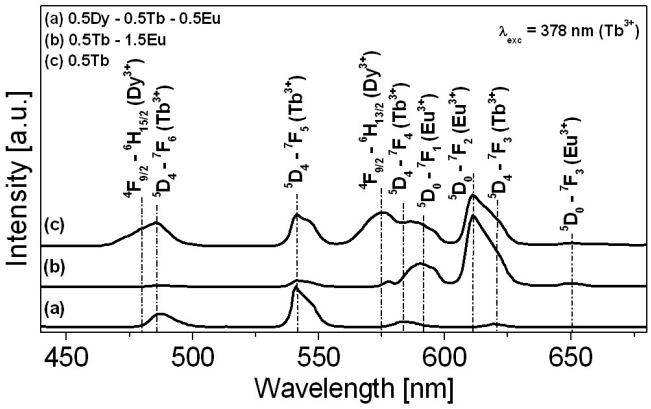



**Fig. 49. Luminescence spectra of rare earth ions in borate glasses containing lead.**

Generally, these trivalent rare earths are incorporated to glass host matrices in order to produce systems emitting four primary color light: blue and yellow ($Dy^{3+}$), green ($Tb^{3+}$) and red ($Eu^{3+}$) light. Our glasses exhibit nearly white emission originating from the simultaneous generation of several bands of $Dy^{3+}$, $Tb^{3+}$, and $Eu^{3+}$ ions under the UV-vis light excitation. The similar effects were also obtained for oxyfluoride silicate glass triply doped with $Dy^{3+}/Tb^{3+}/Eu^{3+}$ [5].

*Acknowledgment*: The National Science Centre (Poland) supported this work under research project 2015/17/B/ST7/03730.

References

[1] V. Mehta, G. Aka, A.L. Dawar, A. Mansingh, *Optical properties and spectroscopic parameters of $Nd^{3+}$-doped phosphate and borate glasses*, Optical Materials, vol. 12, pp. 53-63, 1999

[2] C.K. Jayasankar, V. Venkatramu, S. Surendra Babu, P. Babu, *Luminescence properties of $Dy^{3+}$ ions in a variety of borate and fluoroborate glasses containing lithium, zinc, and lead*, Journal of Alloys and Compounds, vol. 374, pp. 22-26, 2004

[3] V. Venkatramu, P. Babu, C.K. Jayasankar, *Fluorescence properties of $Eu^{3+}$ ions doped borate and fluoroborate glasses containing lithium, zinc and lead*, Spectrochimica Acta A, Vol. 63, pp. 276-281, 2006

[4] J. Pisarska, A. Kos, W.A. Pisarski, *Spectroscopy and energy transfer in lead borate glasses doubly doped with $Dy^{3+}$-$Tb^{3+}$ and $Tb^{3+}$-$Eu^{3+}$ ions*, Spectrochimica Acta A, vol. 129, pp. 649-653, 2014

[5] Ch. Zhu, J. Wang, M. Zhang, X. Ren, J. Shen, Y. Yue, *Eu-, Tb-, and Dy-doped oxyfluoride silicate glasses for LED applications*, Journal of the American Ceramic Society, vol. 97, pp. 854-861, 2014

ECIO 2016
18TH EUROPEAN CONFERENCE ON INTEGRATED OPTICS 2016
18–20 MAY | WARSAW | POLAND

# Direct Integration of Quantum Dot Lasers on Silicon

**Alwyn SEEDS[1*], Siming CHEN[1], Jiang WU[1], Mingchu TANG[1], Huiyun LIU[1]**
[1]Department of Electronic and Electrical Engineering, University College London, Torrington Place, London, WC1E 7JE, England
[*] a.seeds@ucl.ac.uk

Complex photonic systems for optical communications can benefit from monolithic integration of the key photonic devices with their interconnecting waveguides. Advantages include improved stability and environmental ruggedness, reduced size and reduced cost.

Although silicon photonics technology has demonstrated high performance optical modulators and detectors [1,2], efficient electrically pumped optical sources are key to delivering the required range of system functions.

To date the most successful approach has been wafer bonding of compound semiconductor gain sections to silicon waveguides [3,4]. Direct epitaxial growth of compound semiconductor materials on silicon has been frustrated by material lattice mismatch and incompatible thermal expansion coefficients between III–V materials and silicon leading to high-density threading dislocations [5].

Quantum dot (QD) laser gain regions have proved to be less sensitive to defects than conventional bulk materials and quantum well structures, due to carrier localization and hence a reduced interaction with the defects [6,7]. In our work, we have combined QD gain regions with the use of superlattice defect filter layers to enable the direct epitaxial growth of telecommunications wavelength lasers on silicon substrates.

Figure 1 shows the laser structure [8, 9].

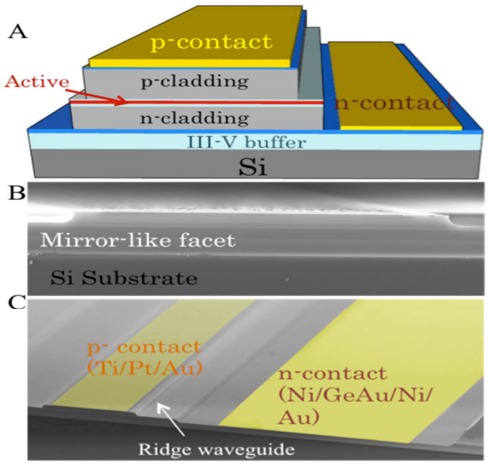



**Fig. 1. III-V laser directly grown on Si substrates. (A) Schematic of the layer structure. (B) Cross-sectional SEM image, of the fabricated Si laser with as-cleaved facet, showing very good facet quality. (C) SEM overview of completed III-V laser on silicon.**

A thin (5 nm) AlAs nucleation layer was first deposited by migration enhanced epitaxy using alternating Al and As4 flux at a low growth temperature of 350 °C. Following the

5 nm AlAs nucleation layer, a three-step growth technique of GaAs epitaxial growth was used with temperatures of 350 °C, 450 °C, and 590 °C for 30 nm, 170 nm, and 800 nm, respectively. Superlattices (SLSs) were then grown as dislocation filter layers on the top of the GaAs buffer layer. Each SLS is made of five periods of 10-nm In0.18Ga0.82As/10-nm GaAs and repeated for four times separated by 300 nm GaAs spacing layers. The strain relaxation of the SLSs applies an in-plane force to the threading dislocations, which enhance the lateral motion of threading dislocations considerably, increasing the probability for annihilation. Using this growth technique a dislocation density as low as $10^5$ $cm^{-2}$ was obtained. A typical QD laser structure was then grown, including five repeats of InAs/GaAs dot-in-a-well (DWELL) structures separated by 50 nm GaAs spacers in the middle of 140 nm undoped GaAs waveguide, 1.4 μm n-type lower and p-type upper $Al_{0.4}Ga_{0.6}As$ cladding layers. The laser structure was completed with a 300 nm p-type GaAs contact layer.

Broad area lasers were fabricated by optical lithography with as-cleaved facets. The measured room temperature threshold current density was 62.5 A $cm^{-2}$, very similar to the best values for lasers grown on native substrates. Optical output powers as high as 105 mW were measured for a current density of 650 A $cm^{-2}$. Lasing was obtained for substrate temperatures as high as 120 °C. An ageing test was carried out at 26 °C and 1.75 times threshold current for 3,100 hours, during which the output power reduced by 27.9% (26.4% in the first 500 hours). The extrapolated time to failure, defined as a doubling of threshold current, was 100,158 hours.

In conclusion, we have demonstrated the first telecommunications wavelength quantum dot laser directly grown on a silicon substrate having high performance and long lifetime.

References

[1] G. T. Reed, G. Mashanovich, F. Gardes, D. Thomson, *Silicon optical modulators*, Nature Photonics. 4, 518-526 (2010).
[2] L. Virot et al., *Germanium avalanche receiver for low power interconnects,* Nature Communications. 5(2014).
[3] A. W. Fang et al., *Electrically pumped hybrid AlGaInAs-silicon evanescent laser,* Optics Express. 14, 9203-9210 (2006).
[4] K. Tanabe, K. Watanabe, Y. Arakawa, *III-V/Si hybrid photonic devices by direct fusion bonding,* Scientific Reports. 2, 349 (2012).
[5] H. Park et al., *Device and integration technology for silicon photonic transmitters,* IEEE Jnl. Sel. Topics in Quantum Electron., 17, 671-688 (2011).
[6] C. Ribbat et al., *Enhanced radiation hardness of quantum dot lasers to high energy proton irradiation*, Electron. Lett. 37, 174-175 (2001).
[7] N. Ledentsov, *Quantum dot lasers: the birth and future trends,* Semiconductors. 33, 946-950 (1999).
[8] S. Chen et al., *1.3 μm InAs/GaAs quantum-dot laser monolithically grown on Si substrates operating over 100 C*, Electron. Lett. 50, 1467-1468 (2014).
[9] M. Tang et al., *1.3-μm InAs/GaAs quantum-dot lasers monolithically grown on Si substrates using InAlAs/GaAs dislocation filter layers,* Optics Express. 22, 11528-11535 (2014).
[10] S. Chen et al., *Electrically pumped continuous-wave III–V quantum dot lasers on silicon*, Nature Photonics doi:10.1038/nphoton.2016.21 (2016)

ECIO 2016
18TH EUROPEAN CONFERENCE ON INTEGRATED OPTICS 2016
18–20 MAY | WARSAW | POLAND

# Mode locked laser systems on InP integration technology platforms

**Erwin Bente[1], Sylwester Latkowski[1], Valentina Moskalenko[1], Mònica Llorens-Revull[1], Kevin Williams[1]**
[1]COBRA Research Institute, Department of Electrical Engineering, Eindhoven University of Technology, P.O. Box 513, 5600 MB Eindhoven, The Netherlands
* e.a.j.m.bente@tue.nl

In recent years a number of Indium phosphide (InP) based photonic integration platforms have emerged which enable complex optical circuits containing optical amplifiers, (electro-optic) phase modulators, low-loss passive waveguides, on-chip mirrors, splitters, filters etcetera [1]. These capabilities provide a freedom in the design of planar integrated mode locked laser sources which is starting to resemble the freedom one has when using bulk optics, but with the added advantages of stability and compactness. This development thus raises the expectation that integrated mode locked laser (MLL) systems can be realised with a performance that supersedes planar waveguide devices that only use an active layer stack and bring integrated MLL devices to applications. Applications of short optical pulses and wide coherent optical frequency combs that can be generated by mode locked lasers e.g. in microwave photonics, communication or biophotonics can present widely varying requirements for the laser system. In a particular technology platform the composition of the layer stack is a given but a large degree of freedom in the design of the laser circuit is available to meet the application requirements. In this paper results are presented that have been obtained at our institute utilising standardised integration platforms on InP that illustrate the advantages and possibilities.

Many planar semiconductor Fabry-Perot lasers show evidence of phase coherence between the modes to some degree. However the basis for every high quality system that is based on quantum well gain material is a passively mode locked laser using a saturable absorber (SA). Such an SA is typically realised using a reverse biased SOA section. The ability to have active and passive waveguide elements in the integrated laser cavity has a number of advantages for such devices. These are illustrated in a design of a mode locked ring laser with a repetition rate of 20GHz as presented in Figure 1 [2].

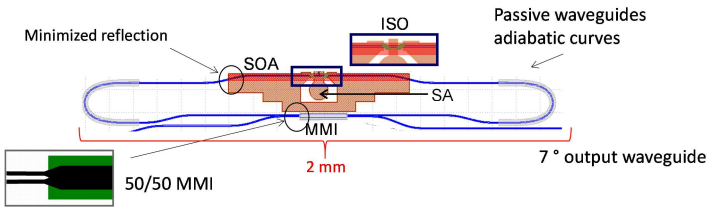



**Fig. 2. Example of a mask lay-out of an integrated mode locked ring laser with 20GHz repetition rate. Specific measures to minimize on-chip reflections are pointed out [2].**

This device has shown a record frequency comb width and a sub-picosecond output pulse duration was demonstrated. The length of the semiconductor optical amplifier (SOA) and the saturable absorber can be much shorter than the laser cavity and thus are to a large extent decoupled from the repetition rate. This helps with suppressing relaxation oscillations. The relative position of the SOA and SA sections can be varied to

control e.g. the relative power in the two directions in the ring. There is much more control over the output coupler which can now be a passive device, in this example a 2 by 2 multi-mode interference coupler (MMI). Such a device has a clearly defined output coupling fraction since it is a passive device. For reliable operation of the MLL it is important that reflections from the intra-cavity components (foundry defined building blocks) are minimised e.g. using methods as pointed out in Figure 1. Using linear cavity designs to establish the optimal position of the SA [3], and the use of distributed Bragg reflectors for tuning the MLL were investigated. We will present the most recent results obtained with such mode locked lasers.

By applying an RF signal the stability of the repetition rate of the MLLs, i.e. the frequency spacing between the lines in the spectral comb, can be improved significantly. If one manages to stabilise the frequency offset of the frequency comb as well, one has stabilised the whole comb. Ongoing research on stabilising the frequency comb of 2.5 GHz repetition rate ring MLL systems [4] using a CW single frequency laser as a reference as well as the possibility to develop a single chip for an integrated Fourier transform spectroscopy system based on two stabilised MLLs will be discussed.

The photonics integration technology allows one to manipulate the output from mode locked lasers using a special amplifiers design or a more complex pulse shaping circuit [5] on the same chip. Since such manipulation is often required in applications, e.g. to achieve the shortest pulse inside an optically dispersive sample. In such applications it is the fixed phase relation between the laser modes that is the most important property of the laser output. Operating such circuits becomes increasingly complex since it involves many electrical signals and the integration of the control electronics with the laser system chip as well as the control strategies for such systems are important research subjects for the future.

This work was supported by the EU FP7 Paradigm project, Technology foundation STW project 13533 “Integrated optical frequency combs” and IOP Photonic Devices project 10016230 “Integrated FTS”.

References

[1] M. Smit, “An introduction to InP-based generic integration technology,” Semiconductor Science and Technology, vol. 29, no. 8, p. 083001, Jun. 2014.
[2] V. Moskalenko, S. Latkowski, S. Tahvili, T. de Vries, M. Smit, and E. Bente, “Record bandwidth and sub-picosecond pulses from a monolithically integrated mode-locked quantum well ring laser,” Optics Express, vol. 22, no. 23, p. 28865, Nov. 2014.
[3] V. Moskalenko, K. A. Williams, and E. A. J. M. Bente, “Integrated Extended-Cavity 1.5μm Semiconductor Laser Switchable Between Self- and Anti-Colliding Pulse Passive Mode-Locking Configuration,” IEEE Journal of Selected Topics in Quantum Electronics, vol. 21, no. 6, pp. 1–6, Nov. 2015.
[4] S. Latkowski, V. Moskalenko, S. Tahvili, L. Augustin, M. Smit, K. Williams, and E. Bente, “Monolithically integrated 2.5 GHz extended cavity mode-locked ring laser with intracavity phase modulators,” Optics Letters, vol. 40, no. 1, p. 77, Jan. 2015.
[5] M. S. Tahvili, E. Smalbrugge, X. J. M. Leijtens, M. J. Wale, M. K. Smit, and E. A. J. M. Bente, “Calibration of an InP-Based Monolithically Integrated Optical Pulse Shaper,” IEEE Photonics Journal, vol. 5, no. 6, pp. 6602317–6602317, Dec. 2013.

ECIO 2016
18TH EUROPEAN CONFERENCE ON INTEGRATED OPTICS 2016
18–20 MAY | WARSAW | POLAND

# Monolithically Integrated Lasers for Comb Generation in Bandwidth Variable Transponders

**M. Deseada GUTIERREZ[1,2*], Jules BRADDELL[2], Frank SMYTH[1,2], Liam P. BARRY[1]**
[1]The Rince Institute, School of Electronic Engineering, Dublin City University, Dublin 9, Ireland
[2]Pilot Photonics, Invent Centre, Dublin City University, Dublin 9, Ireland
[*] desi@pilotphotonics.com

Elastic optical networks (EONs) are being considered for the next generation of optical transport networks due to their potential to provide enhanced spectral efficiency and outstanding flexibility. In EONs, transmission parameters such as modulation format, bandwidth occupancy and baud rate can be adjusted dynamically to suit traffic demands and different transmission scenarios [1-2]. These functionalities can be achieved through the use of innovative bandwidth variable transponders (BVTs) that can be reconfigured by a remote controller. BVTs can benefit from the incorporation of an optical frequency comb (OFC) source which generates the optical carriers from a single subsystem and enables the reduction or elimination of guard bands by ensuring stable frequency spacing between the carriers [1-2]. However, these OFCs are required to be flexible [1-3] and allow easy adaptation of the overall bandwidth (e.g. varying the number of carriers) and the frequency spacing between the carriers to accommodate different modulation formats and baud rates. Ideally, OFCs should also be suitable for photonic integration, yielding further cost-efficiency, footprint and reduction of power consumption. In this work, we present a photonic integrated device for the generation of flexible gain switched OFCs suitable for BVTs. The device comprises two integrated lasers in a master-slave configuration. The spacing between the carriers can be adapted by simply modifying the gain switching RF frequency while the number of carriers can be altered by modifying the interaction between the two integrated lasers.

Fig. 1 (a) shows the schematic for OFC generation by gain switching the monolithically integrated lasers. The photonic integrated circuit (PIC) illustrated in the figure has a standard 1550 nm laser material on an InP substrate with five strained AlGaInAs quantum-wells in the active region. The PIC comprises two integrated discrete mode laser diodes (DMLD) [4]. These lasers are regrowth free Fabry-Pérot lasers that include a mirror section consisting of a number of slots that have been etched close to the active region to provide a regular refractive index perturbation and single mode operation. Each of the lasers is then formed by a gain section and reflector section that provides sufficient reflection to form two differentiated laser emissions, as depicted in Fig. 1 (b).

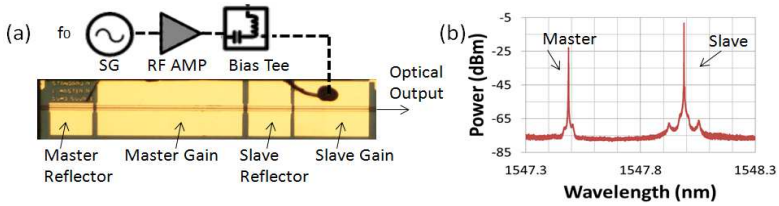



**Fig. 10. (a) Schematic for comb generation by gain switching the manufactured PIC that comprises two integrated lasers. (b) CW Optical spectrum observed at the PIC output.**

These lasers are placed in a master-slave configuration where the light generated from the master is injected into the slave to improve basic laser parameters, such as modulation response. The four sections are dc biased and gain switching is achieved by

direct modulation of the slave gain section with an amplified sinusoidal RF signal in conjunction of the dc bias current. Fig. 2 (a)-(d) illustrates the resultant OFCs generated with frequency spacings between the optical carriers spanning a range of 6-9 GHz. The OFCs obtained consist of 5-8 clearly resolved carriers within a 6 dB window, corresponding to a fixed 6 dB bandwidth of ~50 GHz. These results are achieved by simply changing the RF synthesizer frequency.

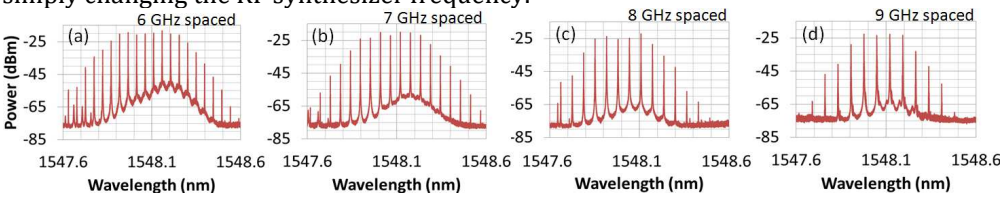



**Fig. 11. Resultant gain switched OFC with different frequency spacing (a) 6 GHz, (b) 7 GHz (c) 8 GHz (d) 9 GHz**

The overall number of optical carriers can be also varied, as depicted in Fig. 3 (a)-(c) where 8, 6, and 4 optical carriers in a 6 dB spectral ripple are observed for the same frequency spacing, 6 GHz. The 6 dB bandwidths are then 48 GHz, 36 GHz and 24 GHz, respectively. These results have been achieved by modifying the current injection to the gain and mirror sections which permits us to control the wavelength detuning and power ratio between the lasers and therefore, the interaction between master and slave.

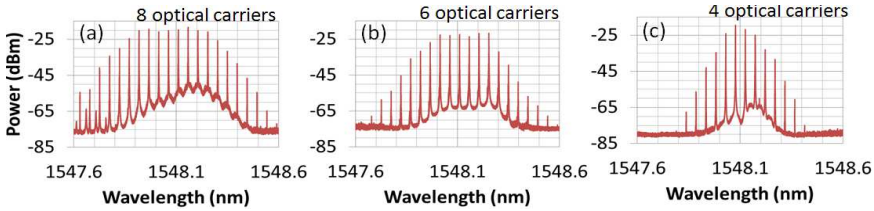



**Fig. 12. Resultant gain switched OFC with different number of optical carriers (a) 8, (b) 6 and (c) 4 optical carriers in a 6 dB spectral ripple**

In summary, in this paper we have demonstrated a photonic integrated circuit that comprises two integrated lasers in a master-slave configuration for gain switched comb generation. The resultant OFC is flexible in terms of frequency spacing and overall bandwidth occupancy. Such integrated devices may offer potential for use in next generation BVTs for elastic optical networks.

References

[1] A. Napoli, M. Nolle, D. Rafique, J.K. Fischer, B. Spinnler, T. Rahman, M. M. Mezghanni, M. Bohn, *On the next generation bandwidth variable transponders for future flexible optical systems*, European Conference on Networks and Communications (EuCNC), pp. 1-5, 2014.

[2] M. Imran, F. Fresi, G. Meloni, L. Potì, *12.5GHz-100GHz tunable spacing optical carrier source for flexgrid bandwidth variable transponders*, in Proc. ONDM, pp. 157-161, 2015.

[3] D. Gutierrez, R. Zhou, F. Smyth, P. Anandarajah, Liam P. Barry, *Software reconfigurable highly flexible gain switched optical frequency comb source*, Opt. Express, 23, pp.23225-23235, 2015.

[4] Q. Lu, W. Guo, M. Nawrocka, A. Abdullaev, C. Daunt, J. O'Callaghan, M. Lynch, V. Weldon, F. Peters, J. F. Donegan, *Single mode lasers based on slots suitable for photonic integration*, Optics Express, vol. 19, no. 26, pp. B140-B145, 2011.

ECIO 2016
18TH EUROPEAN CONFERENCE ON INTEGRATED OPTICS 2016
18–20 MAY | WARSAW | POLAND

# Integrated Long Cavity Mode Locked Ring Laser

**Vinicio CORRAL[1*], Robinson GUZMAN[1], Carlos GORDON[1], Luis J. ORBE[2], Mu Chieh LO[1], Guillermo CARPINTERO[1]**

[1]Department of Electronic Technology, University Carlos III of Madrid, Leganés, 28911, Spain
[2]PhoeniX Software, Hengelosestraat 705, 7521 PA Enschede, The Netherlands
* fcorral@ing.uc3m.es

**Abstract:** We report an integrated 30 mm long cavity mode locked ring laser at 1555 nm, with a low repetition rate at 2.7 GHz. The device uses InP-based active-passive integration technology and integrated multimode interference reflectors. Passive (PML) and hybrid mode locked (HML) operation are experimentally demonstrated, with picosecond pulses of 4.65 ps and 4.23 ps pulse-widths respectively. The device exhibits a very narrow RF linewidth of the beat note of few KHz.

**Introduction:** There are different techniques for generating radiofrequencies. Photonic techniques have a number of advantages over electronic, among which is the possibility of using fiber optics to transport signal with very low propagation loss. Furthermore, photonic techniques have additional advantages such as the quality of the signal generated (low phase noise), the tuning range of the generated frequency and bandwidth modulation [1]. Photonic signal generation techniques are based on optical heterodyning (Dual Wavelength Laser Source), or pulsed lasers (Mode-Locked Laser Source). Each of the techniques has its own quality features and tuning range [2]. The main advantage of the solution provided by the pulsed lasers is that they offer stable signal generation, directly producing a frequency comb. There are extensive references on integrated mode locking lasers [3]. However, few solutions operating within the frequency range of our interest (10 MHz to 14 GHz). The most recent reference is a mode-locked extended cavity in a ring configuration with a repetition rate of 2.5 GHz. The length cavity is 33 mm and the area is 4 $mm^2$ [4]. One way to lower the repetition rate is increasing the length of the cavity. However, due to the propagation loss in the InP, they must be performed by hybrid integration. An example is presented in[5], whose cavity length is 9 cm. The use of photonic integration technologies circuits implementing optical signal sources to improve the quality of the signal generated. Also reduces system size. We aim to develop photonic integrated circuits (PICs) for the generation and distribution of frequency standards and calibration signals of very high quality by photonic techniques.

**Design of device:** We have designed a chip with multiple devices mode-locked. The PIC was designed using standardized building blocks and fabricated within a commercial MPW run through an InP active-passive integration foundry service. The mask manufacturing carried shown in figure 1, where we have the ring structure.

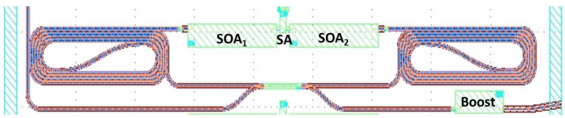



**Fig. 13. Layout of the photonic integrated circuit .**

The ring laser has a cavity length of 30 mm, corresponding to a frequency spacing of 2.7 GHz. It has two 750 µm semiconductor optical amplifier (SOA) with intermediate 50 µm

saturable absorber (SA). At both ends of the SOA, we designed a waveguide passive, whose length is generated by a spiral-shaped structure ("snail"). Both guides on each side of the amplifiers are joined through a 2x2 MMI coupler, forming a ring. At the outputs, we place a Mach Zehnder modulator or another SOA (booster), for modulate the signal inside of the cavity.

**Experimental results:** The results of this device, both mode-locked regime passive (PML) and hybrid (HML) are presented in figure 2 and figure 3. Electrical spectra are generated frequency combs, where the fundamental harmonic appears repetition frequency (2.7 GHz), with higher harmonics. The fundamental harmonic appears in detail being clearly hybrid mode in which the device is more stable. The device exhibits a very narrow RF linewidth of the beat note (11.52 and 5.43 KHz @-3dB, for PML and HML, respectively).

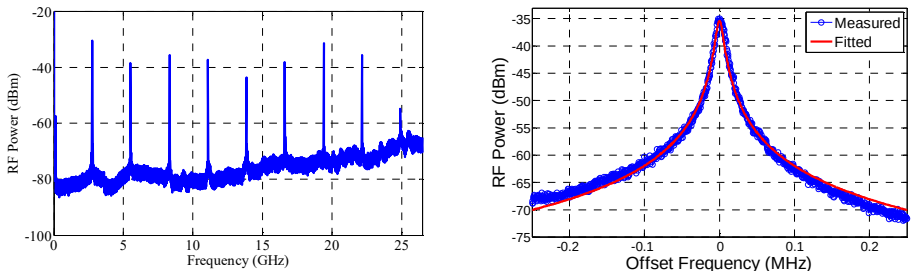



**Fig. 2. PML: Electrical spectrum, Isoa = 115 mA, Iboost = 10 mA, Vsa = -2.28 V .**

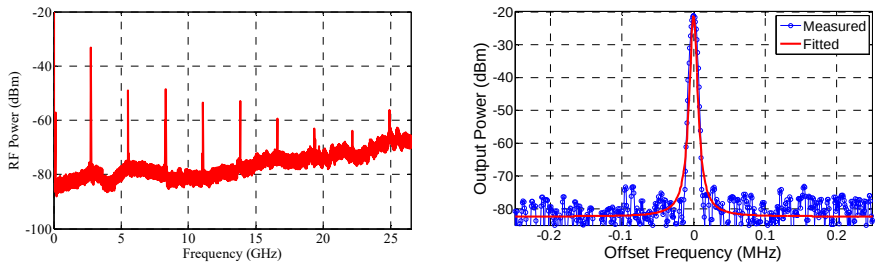



**Fig. 3. HML: Electrical spectrum, Isoa = 115 mA, Iboost = 10 mA, Vsa = -2.28 V .**

## References

[1] G. Carpintero et al, "Photonic Integrated Circuits for Radio-frequency signal generation", Journal of Lightwave Technology, VOL.34, No. 2, pp. 508-515, 2016.

[2] T. Nagatsuma and G. Carpintero, "Recent progress and Future Prospect of Photonics-Enabled Terahertz Communication Research", IEICE Trans. Electron., VOL.E98-C, No. 12, pp. 1060-1070, 2015.

[3] K A Williams et al, "Long-wavelength monolithic mode-locked diode lasers", New Journal of Physics 6 (2004) 179.

[4] S. Latkowski, et al, "Monolithically integrated 2.5 GHz extended cavity mode-locked ring laser with intracavity phase modulators", OPTICS LETTERS, Vol. 40, no. 1, pp.77-80, January 1, 2015.

[5] Martijn J.R. Heck et al, "Ultra-Long Cavity Hybrid Silicon Mode-locked Laser Diode Operating at 930 MHz", Conference OFC.2010, OMI5, Marzo, 2010.

ECIO 2016
18TH EUROPEAN CONFERENCE ON INTEGRATED OPTICS 2016
18–20 MAY | WARSAW | POLAND

# High-Speed Direct Modulation of Waveguide-Coupled Metal-Cavity Nano-Light-Emitting Diodes

**B. ROMEIRA*, V. DOLORES-CALZADILLA, D. HEISS, F. PAGLIANO, S. BIRINDELLI, P. J. van VELDHOVEN, M. K. SMIT, and A. FIORE**
COBRA Research Institute, Eindhoven University of Technology, PO Box 513, 5600 MB Eindhoven, The Netherlands
*b.m.romeira@tue.nl

Future optical interconnects require ultra-small light sources working efficiently (~fJ/bit) at tens of Gb/s speeds [1]. This will be of paramount importance for the development of ultrafast computing and optical communication systems. Electrically driven nanolasers recently succeeded in achieving lasing in sub-μm sized metallo-dielectic cavities [2]. Nonetheless, high losses in metal cavities make it challenging to accomplish efficient lasing at room-temperature (RT), while their predicted high-speed modulation properties have remained unexplored.

As an alternative, nanoscale light-emitting diodes (nanoLEDs) using plasmon waveguides [3] and antenna enhanced waveguide-coupled nanoLEDs [4], appeared recently as promising light sources that are not limited by low-quality cavities, can operate without a threshold and emit in a single spatial mode. Despite these efforts, the proposed sources display negligible output power and ultra-low efficiencies (~$10^{-7}$), preventing the characterization of their modulation characteristics, and therefore limiting our understanding of their true potential for on-chip interconnects.

In this work, we investigate the high-speed dynamic properties of metal-cavity nanoLEDs, Fig. 1(a), operating at telecommunications wavelengths with nW optical output power, Fig. 1(b). Under direct electrical modulation we achieve sub-nanosecond electro-optical response revealing potential for multi-Gb/s modulation speeds.

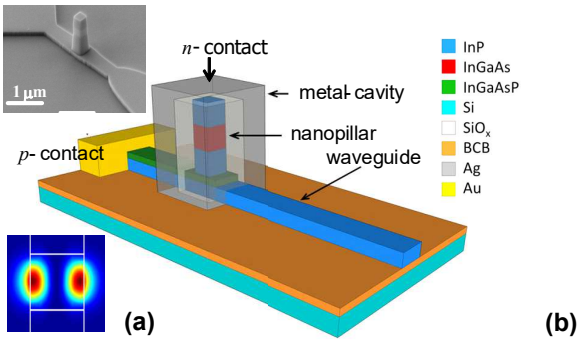



**Fig. 14. (a) Schematic of the waveguide-coupled metal-cavity nanoLED. The inset shows a scanning electron microscope (SEM) picture with the fabricated nanopillar (top-left), and the simulated $|E|^2$ of the in-plane polarized mode supported by the cavity within the InGaAs active region (bottom-left). (b) Typical L-I characteristics measured at 9.5 K and at RT and model fit (dashed curves). The inset shows a typical spectrum emission at RT.**

The nanoLED is a nanopillar metal-dielectric cavity coupled to a InP-waveguide on a III-V membrane bonded to silicon [5]. The nanopillar (~300nm side length) consists of a semiconductor epilayer structure with an intrinsic InGaAs active region, covered with a $SiO_2$ layer and then encapsulated with a silver cladding forming a metallo-dielectric

cavity which redirects a sizeable fraction of spontaneously emitted photons into a single guided mode. Light-current (L-I) curves of a nanoLED are displayed in Fig. 1(b), showing typical optical emission ~1.53 μm with nW (tens of nW) output power at RT (low T) measured from a grating coupler at tens of μA bias levels. The corresponding efficiency for waveguide emission is estimated as $10^{-4}$ and $10^{-2}$ at RT and low T, respectively.

We employed time-correlated single-photon counting to experimentally investigate the high-speed direct modulation of fabricated metal-cavity nanoLEDs. The devices were modulated employing a pulse pattern generator (PPG) while setting a dc bias through a bias-T. The electroluminescence was coupled into a single mode optical fiber using a microscope objective and then guided to a superconducting single photon detector (SSPD). For the time resolved measurements, a histogram of photon arrival times was built by correlating the SSPD output with the PPG trigger with a correlation card.

We achieve ns and sub-ns switching time responses at 9.5 K and at RT, respectively, Fig. 2(a-left). The fast spontaneous decay rates at RT are in good agreement with the modelling results using rate equations, Fig. 2(a-right), confirming that the fast non-radiative recombination is dominant at RT enabling sub-ns modulation. Further speed increase, Fig. 2(b), is achieved by operating at low bias pumping to obtain a full turn-off cycle of the modulation, enabling a fast sweep-out of carriers from the InGaAs active region. The high-speed modulation results represent a step forward in providing ultrafast nanoscale light sources for optical interconnects in nanophotonic circuits.

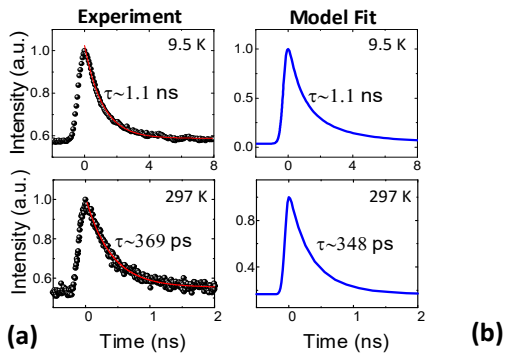



**Fig. 2. (a) Experimental (left) and numerical simulated (right) direct modulation operation at 9.5 K and RT. (b) High-speed modulation at RT varying the bias current revealing sub-100 ps switch-off. In all plots, the modulation was a 80 MHz pulsed signal (100 ps width).**

References

[1] D. A. B. Miller, *Optical interconnects to electronic chips*, Applied Optics, vol. 49, pp. 59, 2010
[2] M. T. Hill, et al., *Lasing in metallic-coated nanocavities*, Nature Photonics, vol. 1, pp. 589, 2007
[3] K. C. Y. Huang, et al., *Electrically driven subwavelength optical nanocircuits*, Nature Photonics, vol. 8, pp. 244-249, 2014
[4] M. S. Eggleston and M. C. Wu., *Efficient coupling of an antenna-enhanced nanoLED into an integrated InP waveguide*, Nanoletters, vol. 15, pp. 3329-3333, 2015
[5] V. Dolores-Calzadilla, et al., *Integrated metal-cavity nanoLEDs in III-V membranes on silicon,* in 2015 Conference on Lasers and Electro-Optics Pacific Rim, paper 27J2_2, 2015

ECIO 2016
18TH EUROPEAN CONFERENCE ON INTEGRATED OPTICS 2016
18–20 MAY | WARSAW | POLAND

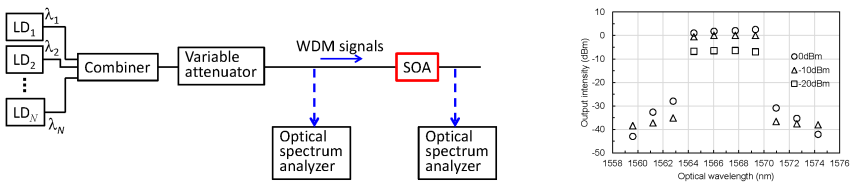
# Multi-Wavelength Lasing with SOA and AWG for Linear-Cavity Fiber Sensor

**Mao OKADA[1], Kazuto TAKAHASHI[1], Hiroki KISHIKAWA[1*], Nobuo GOTO[1]**
**Yi-Lin YU[2], and Shien-Kuei LIAW[2]**
[1]Tokushima University, Tokushima 770-8506, Japan
[2]National Taiwan University of Science and Technology, Taipei City 10607, Taiwan
[*] kishikawa.hiroki@tokushima-u.ac.jp

Optical fiber sensing has been extensively studied in various areas such as aging deterioration measurement of constructed building, seismic measurement, environmental measurement. Optical fiber sensing systems are classified into two configurations. One consists of an optical source, an optical fiber transmission line, and sensing elements. The other consists of a fiber lasing system including sensing element in the cavity [1-3]. Compared to the former, the latter systems have advantages such as higher resolution for wavelength-shift induced by sensing element, and higher signal-to-noise ratio (SNR). By employing a fiber Bragg grating (FBG) as the sensing element, reflecting center wavelength can be shifted due to environmental temperature or tension.

We propose multi-wavelength sensing system consisting of multiple FBG elements and an arrayed waveguide grating (AWG). In fiber lasing systems, erbium-doped fiber amplifier (EDFA), Raman amplifier, and semiconductor optical amplifier (SOA) have been employed as the gain component. We consider multi-wavelength simultaneous lasing to sense multiple points. When the EDFA is employed in the system, the homogeneous broadening of erbium ions limits the number of lasing wavelengths. On the contrary, the SOA shows the inhomogeneous broadening properties, which makes it possible to oscillate at multiple wavelengths.

The proposed fiber sensing system consists of multiple linear cavities lasing at different wavelengths as shown in Fig.1(a). The SOA placed in the linear-cavity amplifies multi-wavelength signals propagating in both directions. The AWG plays a role as multi-/demultiplexer. The passband filtering response of the AWG is schematically illustrated in (b). Since the FBG reflection frequency depends on the environment, an environmental change results in wavelength-shift of the lasing wavelength.




**(a)** **(b)**

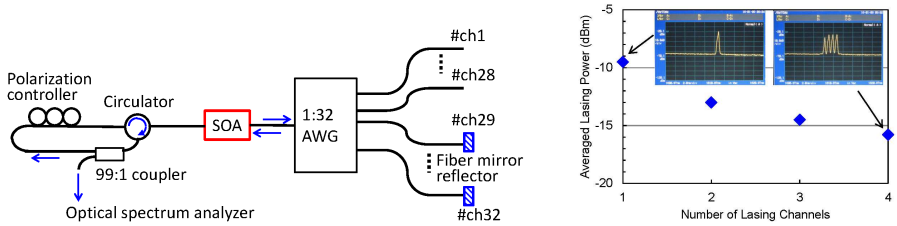
**Fig. 2 Multi-wavelength amplification;(a) the experimental set up and (b) a measured result.**

**Fig.1 (a) Linear-cavity multi-channel fiber sensing system and (b) lasing spectrum with AWG filtering characteristics.**

We consider optical lasing at multiple wavelengths. The number of wavelength channels is limited by amplifiable wavelength range and by optical nonlinearity in the SOA. The nonlinearities in multi-channel amplification were experimentally verified

with a SOA (Inphenix, IPSAD1502-214) using an experimental setup shown in Fig. 2(a). We demonstrated four-channel simultaneous amplification. The output intensities including four-wave-mixing (FWM) signals are shown in (b).

Next, we demonstrated multi-wavelength lasing with a linear cavity optical system shown in Fig.3(a). The cavity consists of the SOA, an AWG, fiber mirror reflectors at the end of the four demultiplexed channels (from channel #29 to #32), and a fiber loop mirror consisting of a circulator and a polarization controller. A 99:1 optical directional coupler is employed to measure the optical signal in the fiber loop mirror. The AWG has channel interval of 100 GHz with the insertion loss of 4.01 to 4.53 dB with 20 dB pass-bandwidth of 1.14 nm. The measured optical spectrum for the four-channel lasing is shown in (b). Although a pass-band wavelength of #30 is 1559.0 nm, the lasing was observed at 1609.8 nm due to cyclic nature of the AWG. By employing an optical band-pass filter in the linear-cavity, the lasing wavelength can be changed to 1559.0nm.




**(a)** **(b)**

**Fig. 3. Multi-wavelength lasing; (a) the experimental set up and (b) a measured result.**

**Acknowledgment**

This work was supported in part by JSPS KAKENHI (15H06443) and Collaborative Research Project between National Taiwan University of Science and Technology and Tokushima University.

References

[1] S. Kim, J. Kwon, S. Kim, and B. Lee, *Multiplexed strain sensor using fiber grating-tuned fiber laser with a semiconductor optical amplifier*, IEEE Photon. Technol. Lett., vol.13, no.4, pp.350-351, 2001.

[2] S. -K. Liaw, Y. -W. Lee, H. -W. Huang, and W. -F. Wu, *Multi-wavelength linear-cavity SOA-based laser array for long-haul sensing*, IEEE Sensor J., vol.15, no.6, pp.3353-3358, 2015.

[3] S. Shin, S. -K. Liaw, and S. -W. Yang, *Post-impact fatigue damage monitoring using fiber Bragg grating sensors*, Sensors, vol.14, no.3, pp.4144-4153, 2014.

ECIO 2016
18TH EUROPEAN CONFERENCE ON INTEGRATED OPTICS 2016
18–20 MAY | WARSAW | POLAND

# Analysis of Quantum Dot Single Section FP Lasers for Comb Spectra Generation

**Mariangela GIOANNINI[1*], Paolo BARDELLA[1], Ivo MONTOSSET[1]**
[1]Dipartimento di Elettronica e Telecomunicazioni, Politecnico di Torino, Torino, Italy
[*] mariangela.gioannini@polito.it

There is an increasing interest on Quantum Dot lasers as light source in silicon photonic integrated circuit; one promising application is the use of a QD comb laser as compact WDM source that could replace a DFB array more difficult to integrate with the Si PIC[1]. Many experiments on single section Fabry Perot QD lasers have demonstrated the possibility of generating wide optical comb spectra at telecom wavelengths but there is still a lack of modelling work for providing physical explanations on the capability of the QD lasers of generating phase locked optical modes. We present a Time Domain Travelling Wave model we have recently developed to move the first step in this direction [2]. We discuss here the role of some key QD material parameters such as the large gain compression factor (ε-parameter), the inhomogeneous gain broadening due to QD self-assembled growth process, the homogeneous gain broadening due to polarization dephasing time and the carrier relaxation time.

**Numerical Model** The spatio-temporal evolution of the optical electric field is described by the slowly varying forward/backward components of the electric field coupled with the slowly varying components of the macroscopic polarization which is the sum of the polarizations of each QD sub-group (ie: QDs with almost the same size) of the inhomogeneous ensemble. The polarization equations are coupled with electron and hole multi-population rate equations and the whole system is then solved with a finite difference scheme [2].

**Simulation results and discussion** We consider a 500 μm FP laser with 10 QD layers. We analyse the role of the QD material parameters on the phase locking of the longitudinal modes and on the stability of the intensity of the optical lines. The phase locking is evaluated by the possibility of generating narrow pulses after including the numerical group delay dispersion (GDD) compensation of the FP laser output field. If the modes are in a stable phase relation one respect to the other, the GDD compensation corrects the non-linear phase variation and allows the pulse formation . The intensity stability of each longitudinal mode is analysed by calculating the RIN of each single line compared to the RIN of the total power [3]. The numerical results are summarized in the following figures. Fig. 1(a) plots the output power vs time after a current step of 500mA at *t=0s* and Fig. 1(b) is the optical spectrum showing a -10dB bandwidth of 10nm. Fig. 1(c) reports the intensity vs time of each optical line showing that only few modes initially turns on at *t=0s.* These seed modes start transferring the power to the other adjacent modes thanks to the quite large gain compression of the QDs ($\varepsilon$=1.5 $10^{-16}$ $cm^3$) . This transient concludes at about 250 ns with a rather broad optical spectrum. From this time instant, applying the GDD compensation we can obtain pulses as depicted in Fig. 1(d) and (e).

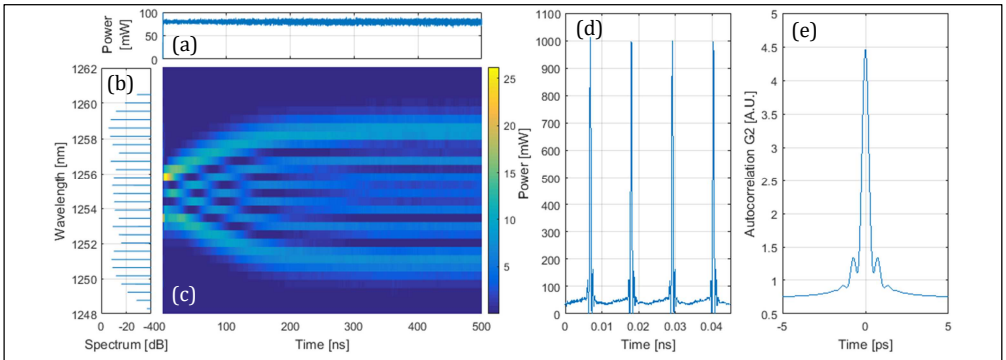



**Fig. 1. (a) Power versus time, (b) optical spectrum, (c) mode intensity versus time, (d) pulses after GDD compensation and (e) corresponding autocorrelation.**

Fig. 2 reports the calculated RIN of the output power and of the individual spectral lines. In good agreement with the experiments [3] the total RIN is much smaller than the RIN of each single line indicating that the intensity fluctuations of the optical lines are coupled and compensate each other. The comparison of Fig. 2a and 2b evidences that a large ε-parameter increases the RIN because of the stronger coupling among the modes. In Fig. 3 we compare the role of the homogeneous broadening (Fig. 3a), of the inhomogeneous broadening (Fig. 3b) and of the carrier relaxation time from the QD excited state to the ground state (Fig. 3c) on the pulse formation and therefore on the number of phase locked modes of the spectrum. From the comparison we conclude that a very homogeneous material (large homogeneous broadening and small inhomogeneous broadening) is the best case for narrow pulses and therefore for increasing the number of locked modes in the spectrum. A slower relaxation time and a slower gain recovery (respect to the cavity round trip) also inhibit multiple pulse formation and improve pulse stability.

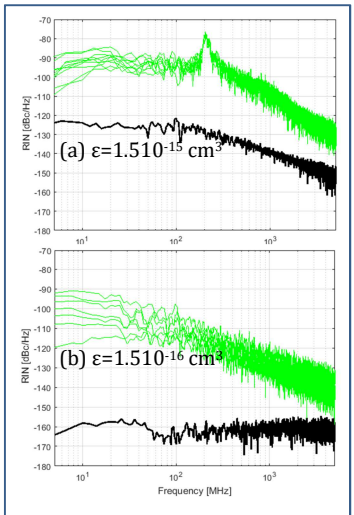



**Fig. 2. Calculated RIN of each optical line (green) and total power (black).**

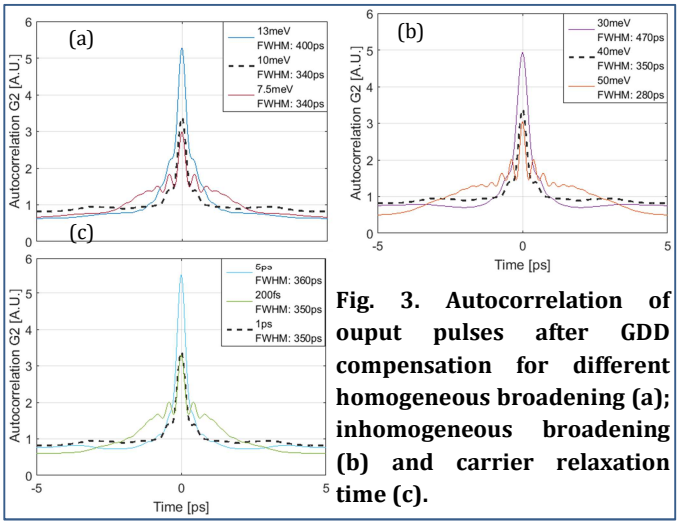



**Fig. 3. Autocorrelation of ouput pulses after GDD compensation for different homogeneous broadening (a); inhomogeneous broadening (b) and carrier relaxation time (c).**

[1] C. Schulien , PIC International Conf., Brussels, 1-2 March 2016
[2] M. Gioannini et al. IEEE J. Select. Top. Quantum Electron., vol. 21, no. 6, 2015
[3] Y .M'Sallem et al. Phot. Tech. Lett., vol. 23, no. 7, 2011

ECIO 2016
18TH EUROPEAN CONFERENCE ON INTEGRATED OPTICS 2016
18–20 MAY | WARSAW | POLAND

# Rate-Equation Analysis for an Integrated Coupled-Cavity Laser with MMI Anti-Phase Coupler

**Daan LENSTRA**
Eindhoven University of Technology, P.O.Box 513, 5600MB , The Netherlands
* d.lenstra@tue.nl

In this paper a dynamical theory is reported for the coupled-cavity laser (CCL) with a multi-mode interference (MMI) coupler, which provides an excellent description of the locking and other operational aspects of the laser realized by D'Agostino et al. in 2015 [1]. The revived interest in CCLs as widely tuneable lasers for sensing and other applications is due to the specially designed MMI anti-phase coupler as described in [1]. The theory explains if, why and how the two individual isolated constituent modes combine to one single "super mode", a situation referred to as locked state. A comprehensive formulation of the model and derivation of the rate equations for the CCL with quantum-well active material can be found in [2].

We consider two Fabry-Pérot (FP) lasers that are very similar except they differ 5–10 % in length and couple by a reflective MMI coupler. The amplitudes indicated (Fig.1) are evaluated at the point where each laser touches the MMI-coupler. Note that the coupling parameters have been designed in such a way that $C_{bar}$ and $C_x$ are 180 degrees out of phase and the sum of their absolute values equals unity. This is a property of the 3x3 reflective coupler in which only the two outer ports are used [1,2]. The ideal theoretical values for the coupling coefficients are $C_{bar}$=0.79 and $C_x$=-0.21 [1,2]. This implies that if the amplitudes $E_1$ and $E_2$ are equal and opposite, the coupler behaves as a 100% reflector for both lasers. Due to small deviations from growth specifications the ideal values for the coupling coefficients can very well be somewhat different. In fact, we found that best agreement with experimental data was achieved by taking smaller values for $C_{bar}$, i.e. 0.75 instead of 0.79, and for $|C_x|$, i.e. 0.18 instead of 0.21.

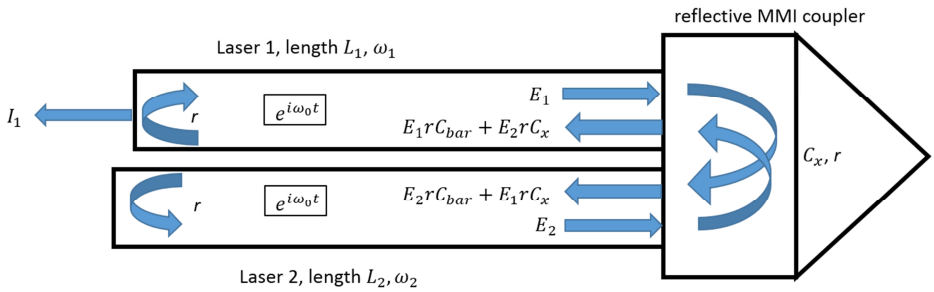



**Fig. 37. Sketch of two FP-lasers coupled by a reflective MMI coupler with designed coupling parameters $C_{bar}$ and $C_x$. The slowly-varying amplitudes are relative to the exponential time factor as indicated, where $\omega_0$ is the locked frequency. $\omega_1$ , $\omega_2$ are the frequencies of the isolated lasers, i.e. when $C_x$=0.**

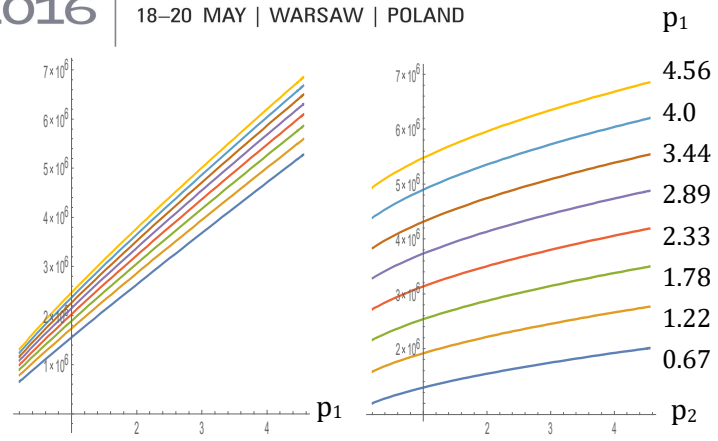



**Fig. 2. Left: Intensity $I_1$ versus $p_1$, at fixed $p_2$ = {0.67, 1.22, 1.78, 2.33, 2.89, 3.44, 4., 4.65}. Right: intensity $I_1$ versus $p_2$, with fixed $p_1$ = {same values}; optimized detuning assumed. The shapes of the curves hardly depend on the precise value of $\alpha$ . The values for $C_{bar}$ and $C_x$ as in table 1 were taken so as to optimize the qualitative and quantitative proportionality agreement with the measured curves in [1].**

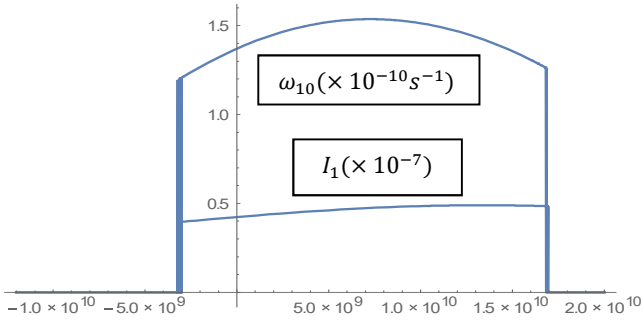



**Fig. 3. Intensity $I_1(\times 10^{-7})$ and operation frequency shift $\omega_{10}(\times 10^{-10})$ versus detuning $\omega_{21} \equiv \omega_2 - \omega_1$ within the locking range. The pump strengths are $p1$=4, $p2$=2.**

Fig. 2 left shows the output-intensity curves of laser 1 versus its pump strength for various values of the pump strength of laser 2; Fig. 2 right shows the output intensities versus the pump strength of laser 2 with the pump strength of laser 1 as parameter. Here we define for $j$=1,2 the pump strengths as $p_j \equiv \Delta J_j / J_{thr,j}$ where $\Delta J_j$ is the injection current w.r.t. the threshold current $J_{thr,j}$ (i.e. when each laser stands on its own, that is, without any coupling. The shapes of the curves agree well with the measured curves in [1]. Fig. 3 shows numerical results for the output intensity of laser 1 and the operation frequency within the locking range.

References

[1] D. D'Agostino,* D. Lenstra, H. P. M. M. Ambrosius, and M. K. Smit, "Coupled cavity laser based on anti-resonant imaging via multimode interference", OPTICS LETTERS, vol. 40, pp. 653-656, February 2015.

[2] D.Lenstra,"Rate-equation analysis for the coupled-cavity laser with MMI anti-phase coupler", DOI: 10.13140/RG.2.1.2747.6245, February 2016.

ECIO 2016
18TH EUROPEAN CONFERENCE ON INTEGRATED OPTICS 2016
18–20 MAY | WARSAW | POLAND

# Angled 3D Glass-to-SiPh adiabatic coupler

**Giannis POULOPOULOS[1*], Dimitrios KALAVROUZIOTIS[1], John R. MACDONALD[2], Paul MITCHELL[2], Nicholas PSAILA[2], Joek TUIN[3], Rutger SMINK[3], Sander DORRESTEIN[3], Michiel VAN RIJNBACH[3], Jeroen DUIS[3], Hercules AVRAMOPOULOS[1]**

[1]National Technical University of Athens, Patission 42, Athens, 10682, Greece
[2]Optoscribe Ltd, 5 Bain Square, Kirkton Campus, Livingston, EH54 7DQ. UK
[3]TE Connectivity, Rietveldenweg 32, 5222 AR 's-Hertogenbosch, The Netherlands
[*] jpoul@mail.ntua.gr

**Concept** Despite the promise of Silicon Photonics (SiPh) towards next-generation deployments seamlessly combining the on-chip advanced optical functionality with efficient E/O and O/E conversion, their wide penetration across all communication layers is currently hindered by the lack of efficient and scalable optical input-outputs (I/O) that can be realized using standard low-cost assembly equipment. To this end, diffraction-based structures, such as grating couplers, have been lately superseded by in-place coupling solutions employing inverse tapers [1] or metamaterial waveguides [2] in order to achieve coupling to SMFs through spot-size conversion. Nevertheless, those structures suffer from either increased fabrication complexity, including material engineering and undercut waveguide sections, or considerable losses due to poor mode matching. Recently, a very interesting concept was presented by Soganci et al. [3], proposing a compliant polymer interface between SMFs and nanophotonic waveguides, relying on adiabatic coupling. The first experimental demonstration of the interface [4] revealed the necessity of a well-defined, angled adhesive gap so as contain the scattering loss at the chip edge that is degrading the performance. However, considering the coefficient of thermal expansion (CTE) mismatch between the polymer and the SiPh chip, such an accurate control over the adhesive gap will significantly increase the intricacy of the assembly process.

In the current manuscript we propose and simulate, an adiabatic coupling scheme between a 2 degrees angled 3D glass waveguide and a SiPh platform, as shown in Fig. 1. The concept relies on the simultaneous and reverse tapering of the two waveguide cores, that increases the coupling performance and reduces the coupling length, while it alleviates the edge chip scattering loss thanks to the angled approach. The 3D glass waveguide exhibits a mode diameter of about 7um and it relies on the 3D waveguide inscription technology developed by Optoscribe.

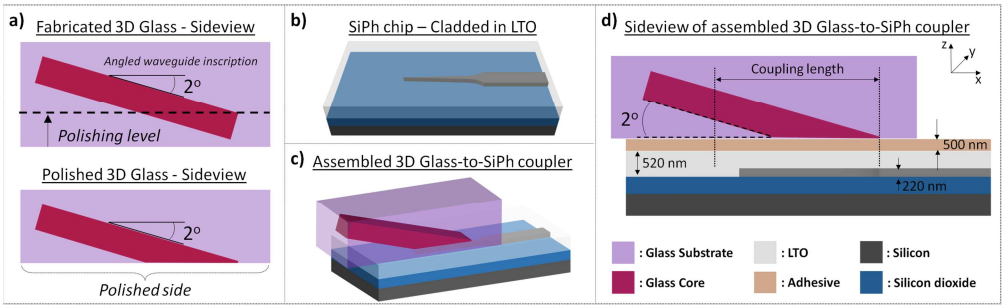



**Fig. 6. (a) Angled 3D glass waveguide, (b) SiPh chip, (c) 3D sketch and (d) Sideview of the assembled 3D Glass-to-SiPh coupler**

Access to the glass waveguide, prior the assembly, can be achieved by regular polishing (Fig. 1a). The SiPh chip employs 220nm top-Si strip waveguide configuration, with

450nm nominal waveguide width and 520nm LTO cladding (Fig. 1b), whereas a 500nm-thick adhesive gap, separating the two platforms, is also considered. A 3D sketch and a sideview of the assembled structure are shown in Figs. 1c and 1d.

**Simulations** Coupler's design relies on the calculation of the optimum taper shape that will allow for maximum power coupling within the coupling length that is firmly specified by the angle of the glass waveguide. The ends of the tapering sections of both waveguides are aligned (marker A, Fig 1d) and the assembled structure is backwards divided into fixed-length segments. For each segment, the width of the silicon waveguide is varied and the excited supermodes are calculated, employing Lumerical's Finite Difference Eigenmode solver (FDE). The optimum silicon width is chosen based on the simultaneous fulfillment of the two following criteria: (i) the overlap integral between the fundamental TE supermode of the current and the previous segment should lay within 0.9975 and 0.9999, (ii) the supermode's effective index should be equal or higher than the effective index of the glass mode so to avoid leaky mode excitation. The resulting taper shape is shown in Fig. 2a revealing a rather slow slope from 170nm to 240nm and fast transitions before and after that. The minimum silicon width was 150nm so as to enable standard photolithography and avoid e-beam.

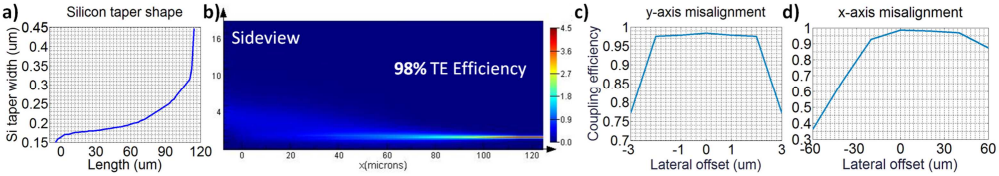



**Fig. 2. (a) Silicon taper shape, (b), Sideview of the EME TE propagating field, and effect of the (c) y-axis and (d) x-axis lateral assembly misalignments on the coupling efficiency**

The coupler design was then imported into a 3D Eigenmode Expansion (EME) propagation simulation environment under the assumption the 2 degrees angle of the propagating field can be ignored. The overall TE glass-to-silicon coupling efficiency was found to be 98% while the coupling length was as low as 120um. A sideview impression of the TE propagating field is shown in Fig. 2b. The effect of the lateral assembly misalignments on the coupling efficiency was also briefly investigated using the EME solver. The results shown in Fig. 2c and 2d indicate adequate tolerance to lateral misalignments both along the y- and the x-axis, enabling the use of low-cost passive alignment assembly equipment.

**Acknowledgments** This work was supported by European Commission under FP7 projects PHOXTROT (318240) and MIRAGE (318228).

## References

[1] X. Tu *et al.*, *Low polarization-dependent-loss silicon photonic trident edge coupler fabricated by 248 nm optical lithography*, Proceedings of the Conference ACP 2015, AS4B.3

[2] T. Barwicz *et al. An O-band Metamaterial Converter Interfacing Standard Optical Fibers to Silicon Nanophotonic Waveguides,* Proceedings of the Conference OFC 2015, Th3F.3

[3] I. M. Soganci *et al.*, *Flip-chip optical couplers with scalable I/O count for silicon photonics*, Optics Express, vol. 21, no. 13, pp. 16075-16085, 2013

[4] T. Barwicz *et al.*, *Optical Demonstration of a Compliant Polymer Interface between Standard Fibers and Nanophotonic Waveguides,* in Proceedings of the Conference OFC 2015, Th3F.5

ECIO 2016
18TH EUROPEAN CONFERENCE ON INTEGRATED OPTICS 2016
18–20 MAY | WARSAW | POLAND

# Optimization of Silicon Photonic Components using Multi-Fidelity Simulations and Co-Kriging

**Pierre WAHL[16], Ivo COUCKUYT[2], Christian KREMERS[3], Frank DEMMING[3]**
**Tom DHAENE[2], Wim BOGAERTS[145]***
[1] Luceda Photonics, Dendermonde, Belgium
[2] Surrogate Modelling Group, Ghent University-iMinds, Dept. of Information Technology, G. Crommenlaan 8 Blok C0 bus 201, 9050 Ghent, Belgium
[3] CST-Computer Simulation Technology AG, Bad Nauheimer Strasse 19, 64289 Darmstadt, Germany.
[4] Photonics Research Group, Ghent University-Imec, Technologiepark 15, 9052 Ghent, Belgium
[5] Center for Nano- and Biophotonics, Ghent University, Belgium
[6] Brussels Photonics Team B-PHOT, Department of Applied Physics and Photonics, Vrije Universiteit Brussel, Brussels, Belgium
* Wim.Bogaerts@ugent.be

Silicon photonic devices can be very compact because of the high refractive index contrast. But this also makes them very sensitive to geometry variations, and hard to model [1]. Typically, a fully vectorial, 3D solution of Maxwell's equations is the only reliable simulation technique, be it with *eigenmode expansion* (EME) or *finite-difference-time-domain* (FDTD). Finding an optimum geometry of a parametric component is therefore computationally very expensive, and it is important to keep the number of these 'expensive' simulation as small as possible. *Efficient global optimization* (EGO) uses *Kriging* to reduce the number of simulations by adaptively selecting the simulation point with the largest likelyhood of producing a better component. However, individual simulations are still expensive.

In this work, we combine expensive, high-precision 3D-FDTD simulations with much cheaper, lower-precision 2D EME simulations to accelerate the optimization. This *Co-Kriging* technique uses the cheap simulations to learn the trends of the component behavior, which are calibrated with the expensive simulations [2]. The cheap simulations allow a quick building of the landscape of multi-dimensional parameter space, which minimized the use of the expensive simulations.

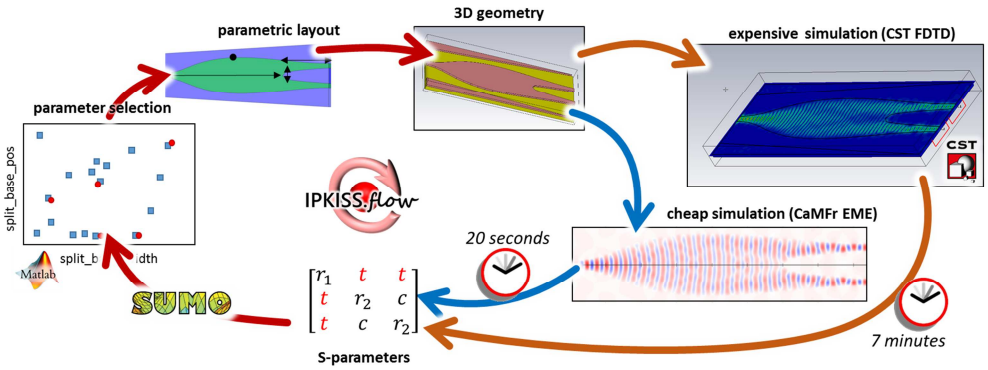



**Fig. 38. Optimization of a photonic component using cheap and expensive simulations**

We have optimized the geometry of a silicon 1×2 splitter for maximum transmission over the entire wavelength range 1.5-1.6 μm. The splitter is a parametric component in the IPKISS design framework, and has 5 parameters for the smooth shape shown in Fig. 2. We defined 2 simulation strategies: a fast 2D EME simulation in CaMFr, and an accurate 3D-FDTD simulation in CST Studio Suite. Both simulations are launched from the IPKISS python interface [3]. The CoKriging optimization is controlled by the *SUMO* and *ooDACE* toolboxes for Matlab [4,5].

The results of this optimization are shown in Fig. 2. The exploration starts with a Latin hypercube sampling of the parameter space using 21 cheap and 4 expensive simulations. After this initial mapping, the cheap simulations are used to map the landscape of the transmission over the entire parameter space, while the expensive simulations are used to target the optimum. The total global optimization in 5 dimensions uses 238 cheap simulations (75 minutes) and only 12 expensive simulations (94 minutes) and yields a splitter with a transmission > 87% over the entire wavelength range.

This demonstrates that the combination of simulation techniques with different fidelity and efficient adaptive sampling algorithms can dramatically improve the optimization cycle of high-contrast photonic components.

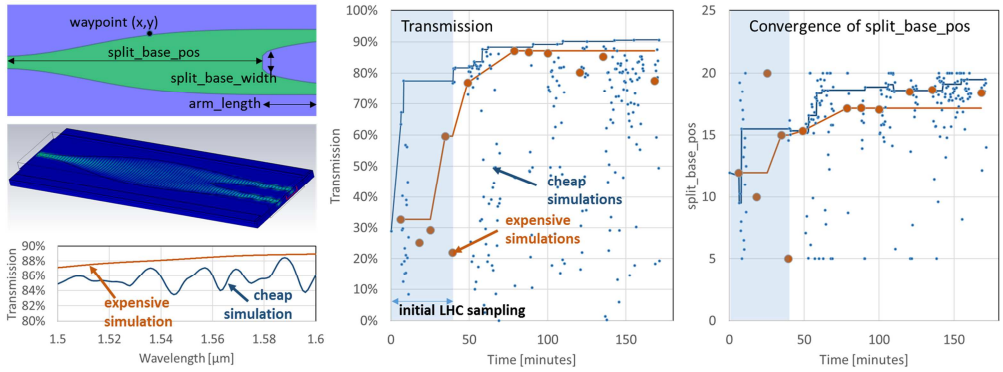



**Fig. 39. Optimization of a 1×2 splitter. Left: splitter geometry and simulation of the optimum result. Middle: Evolution of transmission in cheap and expensive simulations. Right. Sampling of one parameter during simulations.**

References

[1] W. Bogaerts, M. Fiers, P. Dumon, *Design Challenges in Silicon Photonics*, J. Sel. Top. Quantum Electron., 20(4), p.1-8 (2014)

[2] M.C. Kennedy, A. O'Hagan,. *Predicting the output from a complex computer code when fast approximations are available*. Biometrika 87, p.1-13 (2000)

[3] M. Fiers, E. Lambert, S. Pathak, P. Dumon, B. Maes, P. Bienstman, W. Bogaerts, *Improving the design cycle for nanophotonic components*, J. Comp. Sci., 4(5), p.313-324 (2013)

[4] I. Couckuyt, T. Dhaene, P. Demeester, *ooDACE Toolbox: A Flexible Object-Oriented Kriging Implementation*, J. Machine Learning Res. 15, 3183-3186 (2014)

[5] D. Gorissen, K. Crombecq, I. Couckuyt, P. Demeester, T. Dhaene. *A Surrogate Modeling and Adaptive Sampling Toolbox for Computer Based Design*. J. Machine Learning Res., 11, 2051-2055 (2010)

ECIO 2016
18TH EUROPEAN CONFERENCE ON INTEGRATED OPTICS 2016
18–20 MAY | WARSAW | POLAND

# Feedback-Insensitive Integrated Laser

**Perry van SCHAIJK*, Daan LENSTRA, Erwin BENTE**
University of Technology, P.O.Box 513, 5600MB Eindhoven, The Netherlands
* p.v.schaijk@tue.nl

It is well known that semiconductor lasers are highly susceptible to external optical feedback (EOF)[1] which is detrimental to laser performance in many applications. EOF is normally prevented using optical isolators, but these cannot be integrated. Therefore we propose to fabricate an integrated feedback-insensitive laser. Simulations show that such a device can be realized as a ring laser in which the clockwise (cw) and counterclockwise (ccw) modes are not optically coupled. We have studied in detail two configurations of integrated ring lasers that show such characteristics. The theoretical analysis for both configurations is based on rate equations backed up by results from simulation packages.

The first ring laser configuration studied is a so called S-ring laser and is sketched in figure 1a. Here, A and B are 2x1 couplers and O is a 2x2 coupler. The field in the ccw mode splits in A and B and joins the cw mode in B and A, respectively. This creates a different behaviour in the cw and ccw directions which favors the cw over the ccw mode such that the ccw mode will be suppressed. Ref. [2] has implemented such a laser and suppression of the cw mode by 35 dB was observed, but EOF sensitivity was not addressed. Back reflections reaching the out coupler port of the ccw mode will end up in the cw mode and hence are expected to be suppressed as well.

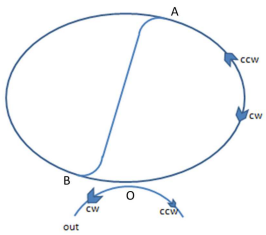



**Fig 1a: schematic layout of S-ring laser**

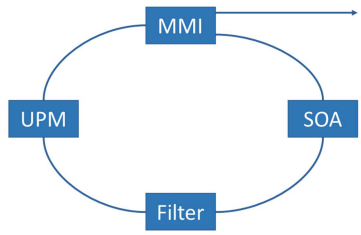



**Fig 1b: schematic layout of ring laser with UPM**

A rate equation analysis for this laser shows that without EOF the cw mode will contain more power than the ccw mode, but the damping of the latter is typically weak, i.e. not exponential but proportional to $1/t^2$, where $t$ is time. Since the ccw mode is at threshold, it is most susceptible for external feedback from the cw mode. Our theory predicts as high as ~10dB cw-ccw power ratio at ~1% EOF. Simulations also show the laser spectrum to be highly sensitive to the feedback. From this we predict that the robustness of such a laser is insufficient for practical applications.

The second laser studied consists of a ring laser and a built-in unidirectional phase modulator (UPM) as shown in figure 2a. Apart from the semiconductor optical amplifier (SOA) and the multi mode interferometer (MMI) for out coupling, the ring contains a UPM and an appropriate spectral filter. The UPM is explained and demonstrated in [3]; ideally it has unit transmission in one direction (the cw direction in this case) and redistributes power in the other direction over various frequencies as shown in figure

ECIO 2016
18TH EUROPEAN CONFERENCE ON INTEGRATED OPTICS 2016
18–20 MAY | WARSAW | POLAND

2b. Thus, assuming ideal components total isolation is achieved at the designed operation frequency when this component is combined with a spectral filter.

Analysis shows suppression of ccw mode with respect to cw mode of ~30dB for ~1% EOF (power). Figures 3 show the simulated dependence of the RIN and linewidth on the

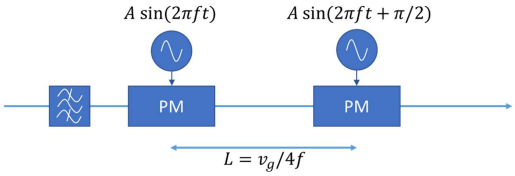



**Fig 2a: schematic layout of UPM**

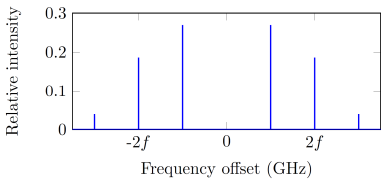



**Fig 2b: transmission of UPM in reverse direction**

fraction $R$ of output power that is returned to the laser for three transmission values of the single-pass transmission $T_{UPM}$ of the UPM and filter combination at the operation wavelength. These figures show negligible influence on the RIN and linewidth of the cw output when $T_{UPM}$ is sufficiently small. We therefore conclude that this proposed laser will be highly insensitive to EOF. We have fabricated a photonic integrated circuit with a ring laser with UPM which is currently being characterized. Its design and initial experimental results will be presented.

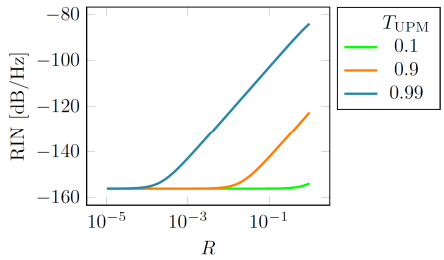



**Fig 3a: RIN vs EOF and UPM transmission**

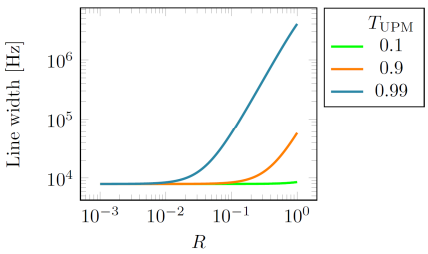



**Fig 3b: line width vs EOF and UPM transmission**

References

[1] R. Tkach and A. Chraplyvy, Journal of Lightwave Technology, 4(11):1655–1661, 1986.
[2] Hongjun Cao, Hui Deng, Hai Ling, Chiyu Liu, Vladimir A. Smagley, Robert B. Caldwell, Gennady A. Smolyakov, Allen L. Gray, Luke F. Lester, Petr G. Eliseev, and Marek Osinski, Applied Physics Letters 86, 203117 (2005); doi: 10.1063/1.1931044
[3] Christopher R. Doerr, Nicolas Dupuis, and Liming Zhang, Optics Letters, 36(21):4293, November 2011.

The work presented is supported by the Technology Foundation STW under project 13540 as part of the Memphis II program and by the research centre for integrated nanophotonics of the NWO gravitation program.

ECIO 2016
18TH EUROPEAN CONFERENCE ON INTEGRATED OPTICS 2016
18–20 MAY | WARSAW | POLAND

# Laser soldering for highest-accuracy passive bonding applications

**Moritz SEYFRIED*, Andreas HOPFMUELLER, Torsten VAHRENKAMP**
[1]ficonTEC Service GmbH, Rehland 8, 28832 Achim, Germany
* Moritz.Seyfried@ficontec.com

The actual state of the art in the field of light coupling into photonic integrated circuits (PICs) mostly is based on eutectic bonding of a III-V-light source onto the PIC followed by an active alignment of at least one optical component. During the active alignment the light source needs to be electrically contacted so that the optical power coupled into PIC can be monitored and used as alignment signal. Depending on the number of optical components in the final device (e.g. ball or spherical lenses, isolators…) this method requires, including the laser diode, at least the alignment of two or more elements. Each of this alignment steps needs a highly sophisticated and specially developed alignment and bonding machine which makes the assembly and packaging of PICs to one of the largest cost driver for the final device. Therefore a reduction in the number of assembled components is highly favourable and directly reduces the production and final product cost and hence is lowering the barriers for a market entry. In this paper we present a diode laser based assembly machine specially developed for highest accuracy passive bonding applications. The aim of this machine is to directly butt couple a laser diode into a waveguide by a passive Top-Bottom-View approach preventing the need of further optical elements.

For this application a special machine was designed and developed which can be seen as e-drawing in figure 1. The key elements of this machine are a high accuracy motion stage with a bidirectional repeatability of down to +/- 14 nm as well as a vision system including microscope objectives leading to a resolution of ~ 0.3 µm/pixel for all cameras. An automated referencing system for the cameras was implemented.

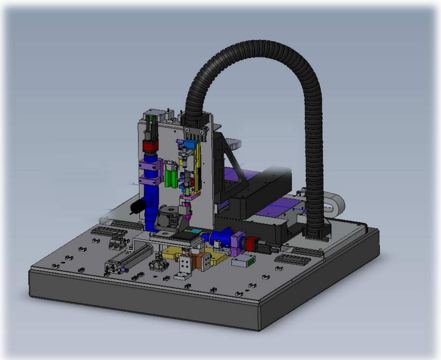


**Fig. 40. 3D model of the high accuracy laser bonder which was tested.**

For a reliable and repeatable detection of the reference marks with accuracies far below one micron, which is a key element for passive placement, special software tools have been developed. One of the major challenges within a soldering process is to keep the aligned position of both components during soldering when the components are heated up from room temperature to ~ 300°C. To keep the thermal input to the devices as minimal as possible a fast heat up and cool down of the devices is favourable. To

accommodate for this a diode laser based soldering approach was chosen and implemented into the machine. With such an approach pure bonding times of below one second have been achieved in the past. As the solder pad inevitably needs to be at elevated temperatures during bonding a sophisticated design of the work holder is necessary to prevent any relative movements. By choosing a proper design as well as the best suited material combinations a work holder with negligible thermal expansion and shift could be manufactured.

To achieve the final goal of the most accurate passive bonding process all hardware and software routines needed to be optimized for the best accuracy and repeatability. Therefore external laser interferometer measurements on the linear accuracy, angular accuracy as well as on the repeatability of all axes have been performed to ensure and improve the quality of the motion system. The vision algorithms have been tested and optimized by measuring the position of the reference marks for hundreds of repetitions until the highest possible repeatability was obtained. After this the combined vison and motion accuracy and repeatability was tested. Figure 2 left shows the distance error between two reference marks measured repeatedly for roughly one hour. Standard deviations of down to 24 nm could be obtained. Due to the Top-Bottom View approach the reference marks on the laser die are not visible any more after bonding and hence a testing of the placement or bonding by visual inspection of the assembled device is not possible. However we have been able to measure the optical power coupled into the PIC which allows conclusions about the placement of the laser die. Figure 2 right shows the optically coupled power into the PIC for 17 subsequent assemblies. The first 5 assemblies have been done on day 1 whereas the last 12 assemblies have been done on the following day without any adjustments or test builds in between. This shows that the machine can reproduce exactly the same bonding conditions after more than a 24 hour break.

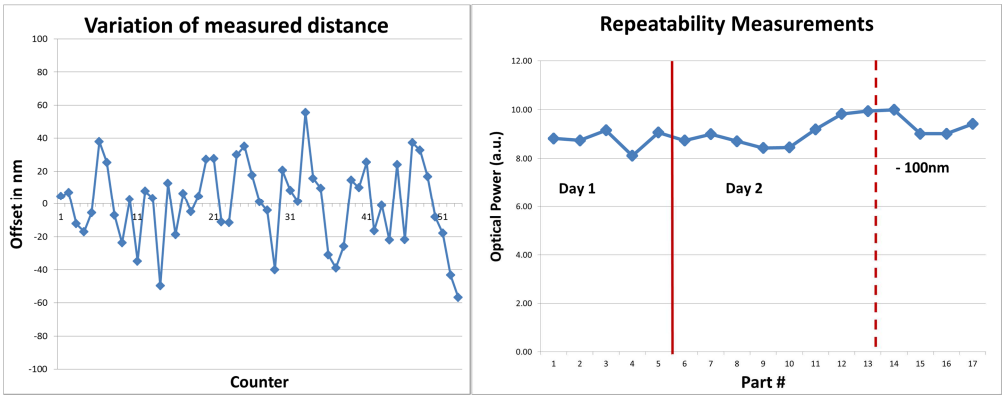



**Fig. 2. Left: Optically measured distance between two fiducials for over 50 measurement cycles. Right: Optical power coupled into a PIC chip17 subsequent builds over two days.**

These results show that the combination of a high accuracy alignment machine with the technique of laser bonding can produce extremely accurate and reproducible bonding results. Hence the presented machine is a very powerful tool for flexible small series or prototype production. A volume manufacturing machine actually is under development.

ECIO 2016
18TH EUROPEAN CONFERENCE ON INTEGRATED OPTICS 2016
18–20 MAY | WARSAW | POLAND

# Integratated IR detection modules

**Maciej FIMIARZ*, Przemysław KALINOWSKI, Józef PIOTROWSKI, Waldemar GAWRON, Artur KĘBŁOWSKI, Dawid STĘPIEŃ, Jarosław PAWLUCZYK**
Vigo System S. A. , Poznańska 129/133, Ożarów Mazowiecki, 05-850, Poland
* mfimiarz@vigo.com.pl

In this paper we present the results of the development of the techniques of integration the infrared detectors with the high speed front-end circuits. The integrated detector consists of: miniature uncooled LWIR/MWIR/SWIR fast detector [1,2], Peltier element and fast low noise transimpedance amplifier. The benefits of the integrated solution compared to the standard IR detection module:

- High speed due to the reduced distance between the amplifier and the detector, which results in decrease of the parastatic inductance and capacitance.
- Improved immunity to the EMI – the preamp is shielded, the uput signal is strong
- Ease of use – the output impedance is standard 50 Ohm – the following amplifier stage may be designed by using common RF techniques

We developed PCB and integration techniques including connection between detector and amplifier, reliable examination of the detector with the preamplifier and hermetic packaging.

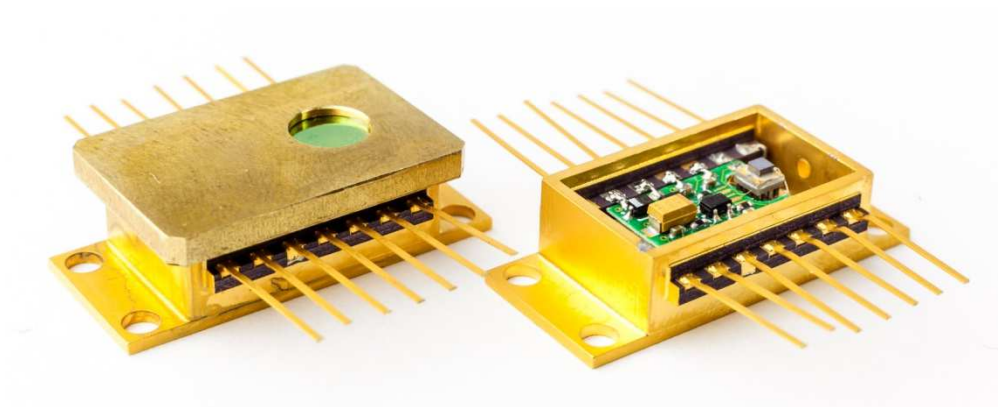


**Fig. 41. Integrated IR detection module in 14-pin butterfly package.**

**Acknowledgement**

*The work was supported by The National Centre for Research and Development, Poland, project PBS2/B3/20/2013 and POIR.01.01.01-00-0389/15-00*

References

[1] J. Piotrowski and A. Piotrowski, "*Room temperature photodetectors*", in Mercury Cadmium Telluride: Growth, Properties and Applications, pp. 513–537, edited by Peter Capper and James Garland, Willey 2011.

[2] J. Pawluczyk, J. Piotrowski, W. Pusz, A. Koźniewski, Z. Orman, W. Gawron, A. Piotrowski „*Complex Behavior of Time Response of HgCdTe HOT Photodetectors*", Journal of Electronic Materials, vol. 44, no. 9, pp. 3163-3173, 2015; DOI 10.1007/s11664-015-3858-6

ECIO 2016
18TH EUROPEAN CONFERENCE ON INTEGRATED OPTICS 2016
18–20 MAY | WARSAW | POLAND

# High Fidelity Electron Beam Lithography for Photonic Devices

**Martin KIRCHNER**
Raith GmbH Dortmund, Germany

Electron beam lithography is a well-established method to define photonic elements. Waveguides, gratings and photonic crystals are important building blocks for many photonic devices. However the traditional way of electron beam lithography comes along with stitching errors reducing device performance. The presentation will review some innovative writing techniques, which help to write devices without stitching errors.

*Long abstract not available at the date of final printing.*

ECIO 2016
18TH EUROPEAN CONFERENCE ON INTEGRATED OPTICS 2016
18–20 MAY | WARSAW | POLAND

# PICs in Terabit Networks

**Marcin TOMKIEWICZ[1], Jarosław KUCIO[2]**
[1]FCA Sp. z o.o., Poland
[2]INFINERA, Poland

Infinera as a global leader in large-scale photonic integrated circuit technology has developed 500 Gb/s super-channel modules integrating over 600 optical functions within a pair of small fingernail-sized chips. Currently the PIC technology is being implemented in 1.2 Tb/s superchannels providing incomparable bandwidth for telecommunication and data center applications. The presentation, provided by FCA – the major Polish partner of Infinera company – will demonstrate key technology aspects and their impact on the latest DWDM implementations.

*Long abstract not available at the date of final printing.*

ECIO 2016
18TH EUROPEAN CONFERENCE ON INTEGRATED OPTICS 2016
18–20 MAY | WARSAW | POLAND

# Optical Isolators for Photonic Integrated Circuits

**Martijn J. R. HECK**
Aarhus University, Department of Engineering, Finlandsgade 22, 8200 Aarhus, Denmark
mheck@eng.au.dk

With the advance of mature fabrication technologies, photonic integrated circuits (PICs) reach ever-higher levels of complexity. Integration of thousands of components has been shown [1], with each main technology showing an exponential growth in complexity [2]. This increase in complexity requires a convergence in technologies, and the roadmaps are currently being pushed by silicon nitride, (hybrid) silicon and indium phosphide PIC technologies. This trend is further fuelled by the establishment of PIC foundries for these main PIC technologies.

Although this convergence on a few main PIC platforms and process flows is a requirement for increasing the complexity, yield, uniformity and robustness of PICs, and decreasing the cost, this means that flexibility on the physical level is limited. The emphasis shifts towards the circuit level. Practically this means that challenges for the application need to be solved by clever PIC design, instead of merging new materials or process steps into the fabrication flow.

One major challenge is the isolation between the various optical components on a PIC. Optical isolators are ubiquitously used in fiber-optic and discrete-optics systems, e.g., to prevent optical feedback from entering a laser cavity. Even minute amounts of coherent feedback, e.g., due to reflections further downstream the system, will increase the laser noise [3]. In silicon and silicon nitride PIC platforms the light source is hybridly integrated in the package, and discrete isolators can be added [4]. However, the indium phosphide and hybrid silicon platforms [5] do not have this option, as the laser is integrated on the PIC. Previous research has clearly shown the limitations due to on-chip optical feedback for tunable lasers [6], mode-locked lasers [7] and wavelength converters [8]. Although by careful design the on-chip reflections can be minimized [9,10], optical isolators with an isolation ratio of around -20 dB are still required.

Efforts to integrate practical optical isolators on a PIC typically include the use of magneto-optic (MO) materials, heterogeneously integrated onto the PIC. With these materials a nonreciprocal absorption [11] or phase shift [12] can be achieved. However, such MO materials are not part of the current PIC foundry platforms. Approaches that are compatible with existing foundry platforms typically make use of time-dependent index or amplitude modulation [13,14].

I will present and discuss two recent approaches to realize PIC foundry-compatible optical isolators. The first is based on hybrid integration of two PICs, using vertical grating couplers for coupling (Fig. 1) [15]. The second approach is based on the timed drive of a pair of optical modulators, with a main application in microwave photonics (Fig. 2) [16].

Partial funding from Det Frie Forskningsråd through the mmW-SPRAWL project (DFF – 4005-00246) is acknowledged.

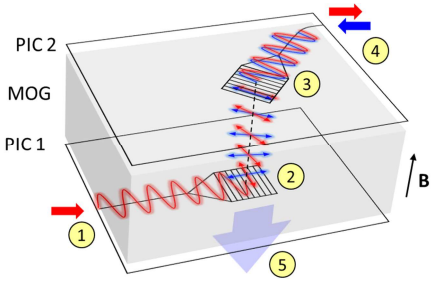



**Fig. 3. Magneto-optic garnet (MOG) between two PICs. TE input light (1, red) propagates through first vertical grating coupler (GC, 2), MOG and second GC (3) to output (4). Counter-propagating TE light (blue) does not couple to the input (1), and is radiated out of the plane (5). The magnetic field direction is indicated by B. Picture from [15].**

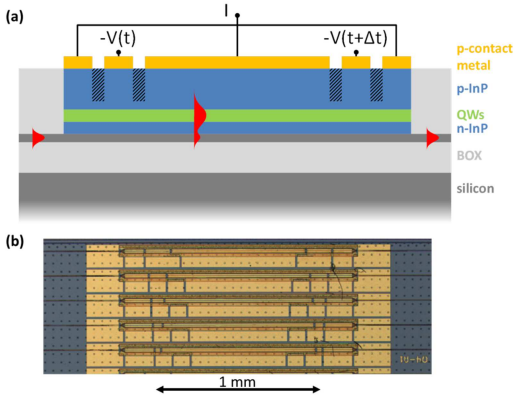



**Fig. 4. (a) Hybrid silicon microwave-photonic isolator, showing the optical field (red). Time dependent reverse bias voltage V(t) modulates transmission. (b) Microscope picture of an array of realized devices. Pictures from [16].**

## References

[1] J. Sun et al., *Large-scale nanophotonic phased array*, Nature vol. 493, no. 7431, pp. 195-199, 2013

[2] M. J. R. Heck, *Hybrid and heterogeneous photonic integrated circuits for high-performance applications*, In Proc. SPIE OPTO, pp. 936503-936503, Intern. Soc. for Opt. and Photon., 2015

[3] R. W. Tkach and A. R. Chraplyvy, *Regimes of feedback effects in 1.5 μm distributed feedback lasers*, Journ. of Lightw. Technol. vol. 4, no. 11, pp. 1655–1661, 1986

[4] P. De Dobbelaere et al., *Packaging of Silicon Photonics Systems*, In Proc. Optical Fiber Communication Conference, pp. W3I-2, Optical Society of America, 2014

[5] M. J. R. Heck et al., *Hybrid silicon photonic integrated circuit technology*, IEEE Journal of Selected Topics in Quantum Electronics vol. 19, no. 4, 2013

[6] M. J. R. Heck et al., *Monolithic AWG-based discretely tunable laser diode with nanosecond switching speed*, IEEE Photonics Technology Letters vol. 21, no. 13, pp. 905-907, 2009

[7] Y. Barbarin et al., *Realization and modeling of a 27-GHz integrated passively mode-locked ring laser*, IEEE Photonics Technology Letters vol. 17, no. 11, pp. 2277-2279, 2005

[8] M. L. Masanovic et al., *Widely tunable monolithically integrated all-optical wavelength converters in InP*, Journ. of Lightwave Technology vol. 23, no. 3, pp. 1350-1362, 2005

[9] R. Hanfoug et al., *Reduced reflections from multimode interference couplers*, Electronics Letters vol. 42, no. 8, pp. 465-466, 2006

[10] G. Kurczveil et al., *Characterization of Insertion Loss and Back Reflection in Passive Hybrid Silicon Tapers*, IEEE Photon. Journ., vol. 5, no. 2, p. 6600410, 2013

[11] W. Van Parys et al., *Transverse magnetic mode nonreciprocal propagation in an amplifying AlGaInAs/InP optical waveguide isolator*, Appl. Phys. Lett. Vol. 88, no. 7, p. 071115, 2006

[12] T. Mizumoto et al., *Waveguide optical isolators for integrated optics*, IEEE Journ. Of Quantum Electronics vol. 48, no. 2, pp. 252-260, 2012

[13] C. R. Doerr et al., *Silicon photonics broadband modulation-based isolator*, Optics Express vol. 22, no. 4, pp. 4493-4498, 2014

[14] M. J. R. Heck et al., *Monolithic Semiconductor Waveguide Device Concept for Picosecond Pulse Amplification, Isolation and Spectral Shaping*, IEEE J. Quant. Electron. 43, 10, 910-922, 2007

[15] M. J. R. Heck, *Grating Coupler Enabled Optical Isolators and Circulators for Photonic Integrated Circuits*, IEEE Journ. of Sel. Topics in Quantum Electronics vol. 21, no. 4, pp. 361-369, 2015

[16] M. J. R. Heck et al., *Integrated Microwave Photonic Isolators: Theory, Experimental Realization and Application in a Unidirectional Ring Mode-Locked Laser Diode*, Photonics 2, 3, 957, 2015

ECIO 2016
18TH EUROPEAN CONFERENCE ON INTEGRATED OPTICS 2016
18–20 MAY | WARSAW | POLAND

# Engineering the optical characteristics of waveguide grating couplers

**Hon Ki TSANG, Linghai LIU**
The Chinese University of Hong Kong, Hong Kong, China

We review recent progress in the design of waveguide grating couplers using subwavelength structures and apodization, and describe how direct numerical optimization of grating coupler parameters may further improve their performance. We show how direct numerical optimization may be used to engineer a flat-top spectral response from a grating coupler.

*Long abstract not available at the date of final printing.*

ECIO 2016
18TH EUROPEAN CONFERENCE ON INTEGRATED OPTICS 2016
18–20 MAY | WARSAW | POLAND

# Electro-optic Long Period Ti:$LiNbO_3$ Waveguide Gratings in Parallel for Broadband Filtering

**De-Long Zhang[1,2*], Jia-Qi Xu[1], Wing-Han Wong[1,2], Edwin Yue-Bun Pun[2]**
1 School of Precision Instruments and Opto-electronics Engineering, Tianjin University, Tianjin 300072, China, and Key Laboratory of Optoelectronic Information Technology (Ministry of Education), Tianjin University, Tianjin, 300072, China.
2 Department of Electronic Engineering and State Key Laboratory of Millimeter Waves, City University of Hong Kong, Kowloon, Hong Kong SAR, China.
* dlzhang@tju.edu.cn

We report broadband optical filter based on two parallel electro-optic long period Ti:$LiNbO_3$ waveguide gratings with different pitches. By utilizing electro-optic and photorefractive effects of $LiNbO_3$ and by changing driving voltage, one can realize 360 nm broadband linear tunability and 0-30 dB linear adjustment of dip contrast.

Long-period waveguide grating (LPWG) and long-period fiber grating have similar working principle and application background [1, 2]. An LPWG based on electro-optic effect of $LiNbO_3$ (LN) is promising for high-speed application [3,4]. Here, we demonstrate a broadband filter based on a parallel structure of two electro-optic long period gratings in two same Ti:LN strip waveguides. The device was developed on the basis of the electro-optic and photorefractive effects of LN.

The device was fabricated in a following way. First, a special structure of an array of strip waveguides embedded in a planar waveguide was fabricated on an LN substrate surface by successive diffusion of 60 nm thick homogeneous Ti film at 1060 $^{o}$C for 6 h and an array of 6-μm-wide, 105-nm-thick Ti-strips at 1060 $^{o}$C for 11 h. Second, a 320 nm thick $SiO_2$ buffer layer was coated onto the waveguide surface. Third, two parallel interdigital Al electrodes with pitches 675 and 880 μm were patterned on the top surface. Upper left of Fig. 1 shows the structure of the device.

After the fabrication, the device performances were fully characterized. The lower left part of Fig. 1 shows the morphology of waveguide surface and the mode patterns of the strip waveguide at the 1.5μm wavelength. The upper right of Fig. 1 shows the normalized transmission spectra of the device driven under different voltages for the grating having a pitch of (a) 675 μm and (b) 880 μm. Two features could be identified from these spectra. First, the contrast of the dip increases with a rise in driving voltage. The panel (a) in the lower right of Fig. 1 shows the driving voltage dependence of the dip contrast for the two grating pitches. We note that as the voltage changes from zero to 300 V the contrast increases almost linearly from zero to 30 dB. This feature is associated with the electro-optic effect of LN. Second, the panel (b) in the lower right of Fig. 1 shows the driving voltage dependence of the resonant wavelength for the two grating pitches.

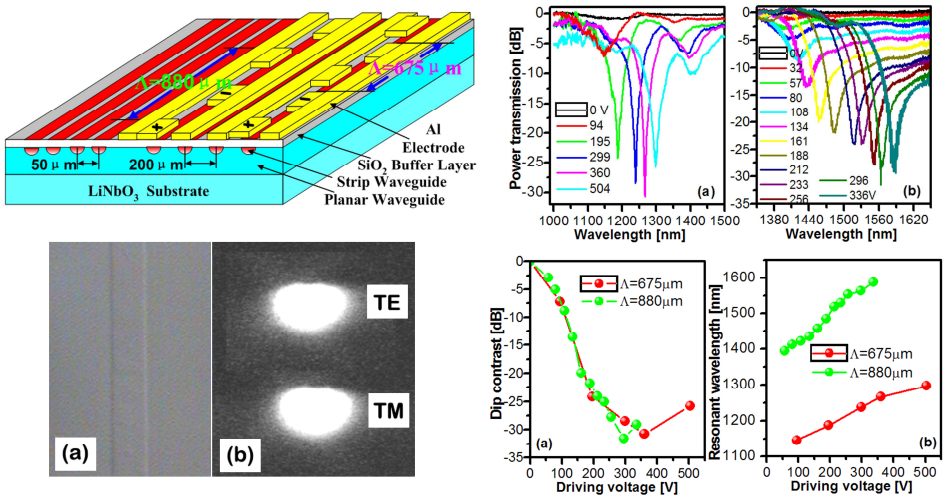



**Fig. 1. Upper left: Structural schematic of device; Lower left: (a) Waveguide surface and (b) mode images at 1.5 μm; Upper right: Transmission spectra of the device driven under different voltages for grating pitch of (a) 675 μm and (b) 880 μm; Lower right: Driving voltage dependence of (a) dip contrast and (b) resonant wavelength for two grating pitches.**

One can see that the resonant wavelength red-shifts almost linearly with the increase of the driving voltage. The shift is ~160 nm for the shorter period grating and ~200 nm for the longer pitch grating, and hence ~360 nm in total. An overall investigation shows that the shift is due to the photorefractive effect of LN.

In summary, we have demonstrated a broadband filter based on two parallel electro-optic Ti:LN LPWGs with different pitches. By using the electro-optic and photorefractive effects of LN and by changing the driving voltage, one can realize 360 nm broadband linear tunability and 0-30dB linear adjustment of dip contrast. Broader bandwidth is expected by using more parallel LPWGs. The device may find its use in fields of high-speed optical filter, gain flattening and sensing.

References

[1] M. Kulishov, X. Daxhelet, M. Gaidi, M. Chaker, Transmission spectrum reconfiguration in long-period gratings electrically induced in pockels-type media with the help of a periodical electrode structure, J. Lightwave Technol., vol. 22, no. 3, pp. 923-933, 2004.

[2] S. Pal, A. Chauhan, M. Singh, P. Kumar, M. Sharma, N. Pradhan, K. Singh and C. Dhanavantri, Realization of long-period corrugated grating in silica-on-silicon-based channel waveguide, IEEE Photon. Technol. Lett., vol. 21, no. 20, pp. 1490-1492, 2009

[3] W. Jin, K. S. Chiang and Q. Liu, Electro-optic long-period waveguide gratings in lithium niobate, Opt. Express, vol. 16, no. 25, pp. 20409-20417, 2008

[4] J. Kang, W. H. Wong, E. Y. B. Pun and D. L. Zhang, Electro-optic long period grating based on Ti:$LiNbO_3$ optical waveguide, IEEE Photon. Technol. Lett., vol. 27, no. 24, pp.2555-2558, 2015

ECIO 2016
18TH EUROPEAN CONFERENCE ON INTEGRATED OPTICS 2016
18–20 MAY | WARSAW | POLAND

# Critical coupling enhanced refractive index sensing in SOI slot microring resonators

**Weiwei Zhang*, Samuel Serna, Xavier Le Roux, Laurent Vivien, and Eric Cassan**
Institut d'Electronique Fondamentale, University Paris-Sud, CNRS UMR 8622, Université Paris Saclay, Bat. 220, 91405 Orsay Cedex, France
* weiwei.zhang1@u-psud.fr

## Abstract

We present a novel refractive index sensing mechanism based on slot ring resonators fabricated in the silicon platform. The sensing mechanism relies on detuning the critical coupling resonance of the ring. This new method has been realised through engineering the dispersion property of the ring directional coupler, which enables forming a narrow ring resonance spectrum with a V-shape profile. We both numerically and experimentally demonstrate that this V-shape profile can enhance the refractive index sensing operation due to following conditions: firstly, the V-shape is robust in the 1.3-1.5 refractive index range; secondly, the critical resonance peak (or bottom of the spectrum V-profile) follows a monotonically increase with the refractive index change, which results in a strong critical coupling detuning. The sensitivity of the critical peak has been measured to around 1300nm per refractive index unit with an uncertainty of the shift equal to 2 times the ring free spectral range. Different from a single resonance peak sensing, , the proposed sensing mechanism can get rid of the high losses of slot waveguides that usually spoil the ring and can target low detection limit.

## Introduction

In the context of refractive index sensing in integrated silicon photonics, ring resonators [1], [2], nano cavities [3], Mach–Zehnder interferometers [4] and Bragg gratings [5] have been proposed and demonstrated with asssed feasibilities. Complex structures, for instance, quadrabeam photonic crystal cavities [6], Vernier ring resonators [7] or ring resonator with Mach–Zehnder interferometers [8] have been proposed to increase the sensitivity and lower sensor limit of detection.

Basically, the sensing mechanism of these devices is based on the light matter interaction between the cladding material and the evanescent field out of the silicon core, which thus results in a weak optical mode perturbation. To improve and enhance light matter interaction, hollow core waveguide sensors with strong light confinement in low index active materials have been demonstrated with larger sensitivities than their standard rib-or-ridge-waveguide-based counterparts [1]. In this context, slot waveguides, which can partially confine light power up to 40-50% in low index in-slot materials, can strongly enhance the electric field in the slot region. They have been demonstrated with lots of applications such as refractive index sensing, optical manipulation of nanoparticles/biomolecules [9], all-optical signal processing [10] through nonlinear optical processes , and so on.

## Experiments

In the present paper, we present a sensing method based on slot waveguide ring resonators to overcome loss limited individual resonance Q-factors. The proposed principle consists in a quick detuning of the micro-ring resonator critical coupling peak wavelength when experiencing a weak cladding index change. In this purpose, the considered slot waveguide bus-waveguide/micro-ring coupler is specially designed to increase the cross coupling ability wavelength dispersion. In the specifically studied case, geometry optimization led to a Si slab thickness of 220nm, rail width of 170nm, slot width of 110nm, and a coupler gap of 600nm. Then, relying on such a highly dispersive coupler, resonance spectra displayed distinguished critical coupling peaks [11]. In a similar configuration but with normal rail width couplers (235nm), a wider spectrum envelop is obtained, as show in Fig.2, preventing a clear identification of the critical peak.

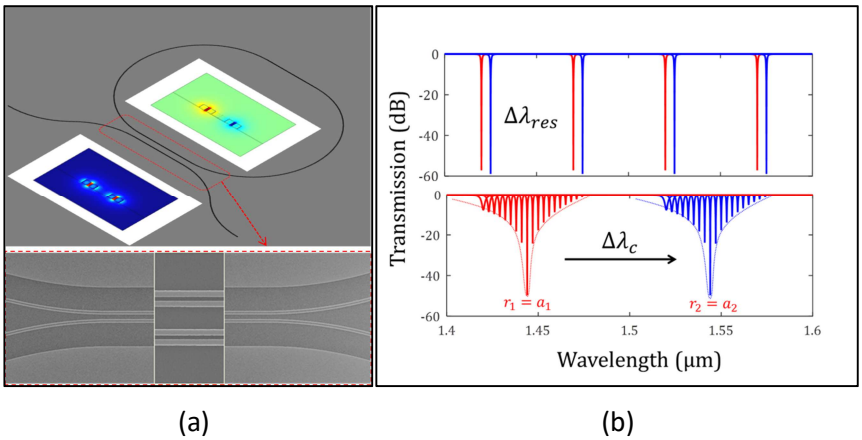



**Fig. 1. (a) Optical design of dispersive coupler loaded silicon slot microring resonator; (b) Comparison between single peak sensing and critical coupling enhanced resonance comb sensing.**

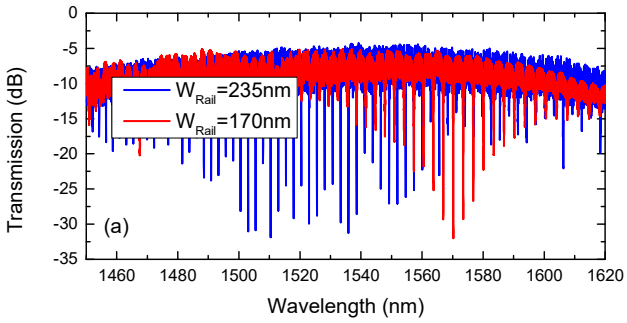



**Fig. 2. Comparison of strong dispersive coupler ($W_{rail}$=170nm) and normal coupler ($W_{rail}$=170nm) loaded slot ring resonators' transmission spectra.**

This engineered critical coupling condition can serve as a new sensing method if compared with a standard single peak sensing scheme, as shown in Fig.1.b. In this critical coupling sensing mechanism, the deepest peak shifts are monitored instead of a

single peak shift. To verify this principle and estimate the sensitivity of the optimized optical ring sensors, we realized a set of experiments by drop casting a series of commercial index liquids (from Cargille). As depicted in Fig.3, the experimentally monitored resonance spectra effectively sustain V shape profiles and clearly exhibit a nearly-single critical resonance peak (with an uncertainty range of approximately 2 micro-ring FSRs).

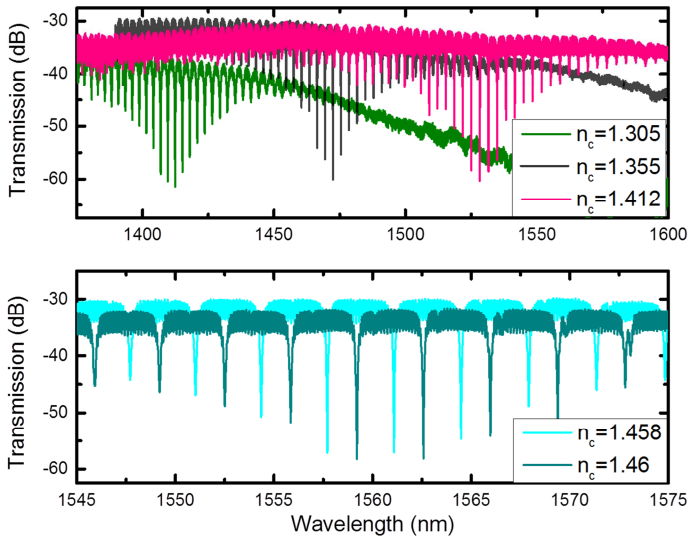



**Fig. 3. Critical coupling enhanced sensing comb shifts due to cladding refractive index change.**

The related monitored critical peak wavelength shift is plotted in figure.4.a. A very fast critical coupling resonance peak detuning corresponding to sensitivity (S) of 600-1300 nm/RIU is visible. This sensitivity is around 2-4 times larger than with a standard single peak resonance shift sensing approach. Such large sensitivity originates from the fact that the critical coupling condition is much more sensitive than the effective index ($n_{eff}$) induced resonance change. As shown in Figure.4.b, the related limit of detection defined as 2FSR/S, is here of the order of $10^{-3}$. The pretty high values could be yet easily minimized by considering spiral ring resonators with FSR values down to pm levels. We thus anticipate that limit of detection down to $10^{-5}$ could be obtained by this approach while significantly relaxing the constraint related to high individual peak *Q* factors.

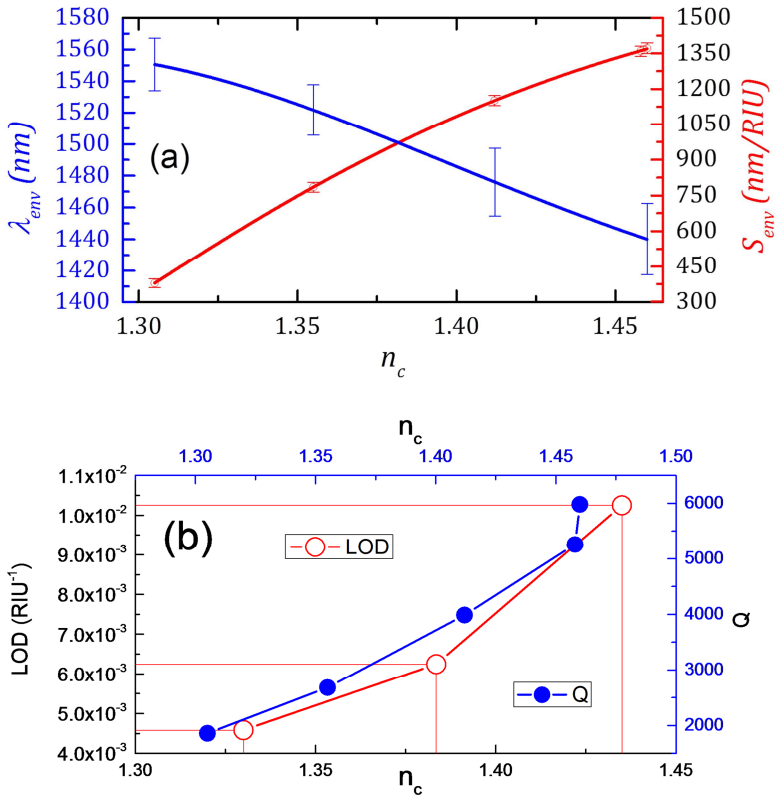



**Fig. 4. (a) Critical coupling peak ($\lambda_{env}$) shift and its sensitivity ($S_{env}$) measured from experiments performed in Fig.3, (b) Limit of the dection (LOD) of critical coupling enhanced sensing and *Q* factor of the critical coupling peaks as function of the cladding refractive index.**

## Conclusion

To conclude, a critical coupling enhanced refractive index sensing approach relying on silicon slot waveguide ring resonators is proposed. The realized optical index sensor has a sensitivity of 1300nm/RIU around the water refractive index (1.33). The proposed method get rids of the necessity of high *Q* factors of the micro-ring resonators and presents a limit of detection that inversely scales with the ring length, typically scalable down to $10^{-5}$.

References

[1] T. Claes, J. G. Molera, K. De Vos, E. Schacht, R. Baets, and P. Bienstman, "Label-free biosensing with a slot-waveguide-based ring resonator in silicon on insulator," *IEEE Photonics J.*, vol. 1, no. 3, pp. 197–204, 2009.

[2] F. Dell'Olio and V. M. Passaro, "Optical sensing by optimized silicon slot waveguides.," *Opt. Express*, vol. 15, no. 8, pp. 4977–4993, 2007.

[3] C. Ca, S. F. Serna, W. Zhang, X. Le Roux, and E. Cassan, "Liquid sensor based on high- Q Slot Photonic Crystal Cavity in Silicon-On-Insulator configuration," pp. 1–3, 2014.

[4] X. Tu, J. Song, T.-Y. Liow, M. K. Park, J. Q. Yiying, J. S. Kee, M. Yu, and G.-Q. Lo, "Thermal independent Silicon-Nitride slot waveguide biosensor with high sensitivity," *Opt. Express*, vol. 20, no. 3, p. 2640, 2012.

[5] X. Wang, J. Flueckiger, S. Schmidt, S. Grist, S. T. Fard, J. Kirk, M. Doerfler, K. C. Cheung, D. M. Ratner, and L. Chrostowski, "A silicon photonic biosensor using phase-shifted Bragg gratings in slot waveguide," *J. Biophotonics*, vol. 6, no. 10, pp. 821–828, 2013.

[6] D. Yang, S. Kita, F. Liang, C. Wang, H. Tian, Y. Ji, M. Lončar, and Q. Quan, "High sensitivity and high Q-factor nanoslotted parallel quadrabeam photonic crystal cavity for real-time and label-free sensing," *Appl. Phys. Lett.*, vol. 105, no. 6, p. 063118, 2014.

[7] T. Claes, W. Bogaerts, and P. Bienstman, "Experimental characterization of a silicon photonic biosensor consisting of two cascaded ring resonators based on the Vernier-effect and introduction of a curve fitting method for an improved detection limit.," *Opt. Express*, vol. 18, no. 22, pp. 22747–22761, 2010.

[8] M. La Notte and V. M. N. Passaro, "Ultra high sensitivity chemical photonic sensing by Mach-Zehnder interferometer enhanced Vernier-effect," *Sensors Actuators, B Chem.*, vol. 176, no. 2010, pp. 994–1007, 2013.

[9] A. H. J. Yang, S. D. Moore, B. S. Schmidt, M. Klug, M. Lipson, and D. Erickson, "Optical manipulation of nanoparticles and biomolecules in sub-wavelength slot waveguides.," *Nature*, vol. 457, no. 7225, pp. 71–75, 2009.

[10] C. Koos, P. Vorreau, T. Vallaitis, P. Dumon, W. Bogaerts, R. Baets, B. Esembeson, I. Biaggio, T. Michinobu, F. Diederich, W. Freude, and J. Leuthold, "All-optical high-speed signal processing with silicon–organic hybrid slot waveguides," *Nat. Photonics*, vol. 3, no. 4, pp. 216–219, 2009.

[11] W. Zhang, S. Serna, X. Le Roux, L. Vivien, and E. Cassan, "Highly sensitive refractive index sensing by fast detuning the critical coupling condition of slot waveguide ring resonators," *Opt. Lett.*, vol. 41, no. 3, p. 532, Feb. 2016.

ECIO 2016
18TH EUROPEAN CONFERENCE ON INTEGRATED OPTICS 2016
18–20 MAY | WARSAW | POLAND

# Integrated polarization controller with 40 dB polarization extinction ratio range in the C-Band

**Jose D. SARMIENTO-MERENGUEL[1], Carlos ALONSO-RAMOS[2*], Robert HALIR[1], Xavier LE ROUX[2], Laurent VIVIEN[2], Pavel CHEBEN[3], Elena DURÁN-VALDEIGLESIAS[2], Íñigo MOLINA-FERNÁNDEZ[1], Delphine MARRIS-MORINI[2], Dan-Xia XU[3], Jens H. SCHMID[3], Siegfried JANZ[3], Alejandro ORTEGA-MOÑUX[1].**

[1]Universidad de Málaga, Dept. de Ingeniería de Comunicaciones, ETSI Telecomunicación, Campus de Teatinos s/n, Málaga, 29071, Spain

[2]Institut d'Electronique Fondamentale, Université Paris Sud, CNRS, UMR 8622, Université Paris-Saclay, Bât. 220, 91405 Orsay Cedex, France

[3]National Research Council Canada Ottawa, K1A 0R6, Canada

[*]carlos.ramos@u-psud.fr

In this work we present a technology-independent highly tolerant tunable polarization controller. The device is implemented in the silicon-on-insulator platform, experimentally achieving 40 dB of polarization extinction ratio (PER) range in the complete C-band, with a Poincaré sphere coverage of 98%. The key benefit of this approach is that a broad PER range is achieved, even when the individual polarization rotators have limited polarization conversion efficiency (PCE) in the range 25-75%. This results in substantially relaxed fabrication tolerances. To the best of our knowledge, this is the highest PER range yet demonstrated in an integrated polarization controller.

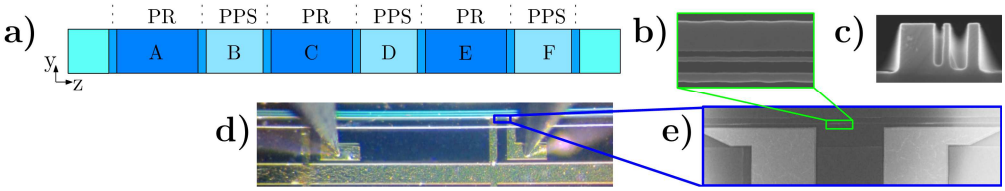



**Fig. 1. a) Schematic of the fabricated polarization controller. b) Top-view of the polarization rotator waveguide. c) Polarization rotator waveguide cross-section. d) Gold heaters placed alongside the waveguides. e) Detail of the heaters placement.**

Polarization controllers are important for many applications, including telecommunications, polarization diversity circuits and sensing, to name a few. These devices typically comprise two elements: a polarization rotator (PR) and a tunable polarization phase shifter (TPPS). While the latter can be implemented using waveguide heaters, the former require either specialized fabrication processes or a tight control of the fabrication tolerances on the order of a few nanometers [1]. These stringent tolerances hinder the integration prospects of these devices. To overcome this limitation we propose a polarization controller device based on three TPPSs and three PRs, shown in figure 1a.

The device operates as follows: Elements A to E (see figure 1.a), act as a tunable polarization rotator [2], establishing the desired polarization extinction ratio, which is defined as the ratio of power in the vertical and horizontal component, i.e. PER = $(|E_x|/|E_y|)^2$. The last element (F) introduces the polarization-dependent phase shift. Note that practically full coverage of the Poincaré sphere is achieved for polarization

rotators with PCE in the range 25-75% (polarization rotator PER in the range ±4.7 dB). This largely relaxes the fabrication tolerances.

Our approach has been experimentally demonstrated in the silicon-on-insulator (SOI)_platform [3]. Figure 1.b,c shows the polarization rotator element. For the implementation of the TPPS we take advantage of the opposite thermo-optics coefficients of the SU-8 (used as cladding material) and the $SiO_2$. As waveguide heaters we used metal pads (gold), as shown in figure 1.d,e.

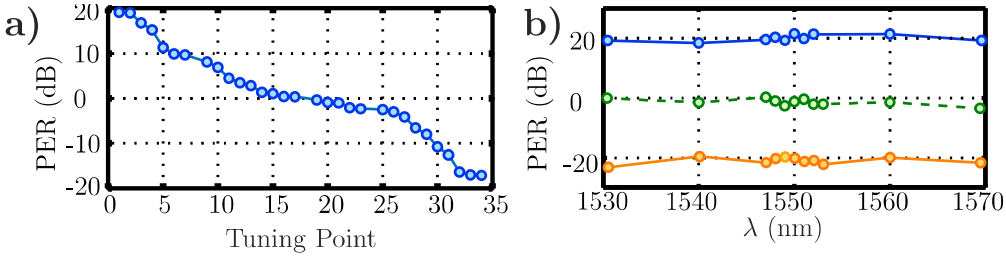



**Fig. 2. a) Measured PER at a constant wavelength, a full 40 dB PER range is achieved. b) Solid lines: Maximum and minimum measured PER over the C-band. Dashed line: raw PER of the polarization rotator elements.**

Several experiments have been carried out to demonstrate the device operation. First, we have demonstrated that a single TPPS can induce polarization phase shifts in the range 0 - 2π. This has been done by increasing the temperature of the last TPPS and measuring the polarization phase. In the second experiment, we evaluated the PER range, by tuning the first two TPPS. Figure 2.a shows the measured PER for this experiment. A range of 40 dB was achieved (PER = 20dB represents virtually pure TE polarization state, while PER=-20dB corresponds to TM state). Once the performance of the device has been demonstrated at a single wavelength, we have tuned the device for different wavelengths, within the C-band. Figure 2.b shows the maximum and minimum measured PERs over the C-band (solid lines) and the raw PER of the rotator elements (dashed line). Our device thus overcomes the current limitations of a trade-off between integration and device performance in polarization management circuits, paving the way towards the monolithic integration of highly efficienct polarization controllers.

References

[1] H. Deng, D. O. Yevick, C. Brooks, and P. E. Jessop, "*Fabrication tolerance of asymmetric silicon-on-insulator polarization rotators*", J. Opt. Soc. Am. A, vol. 23, no. 7, 1741-1745 2006

[2] C. Alonso-Ramos, R. Halir, A. Ortega-Moñux, P. Cheben, L. Vivien, Í. Molina-Fernández, D. Marris-Morini, S. Janz, D.-X. Xu, and J. Schmid, *Highly tolerant tunable wave-guide polarization rotator scheme*, Optics Letters, vol. 37, no. 17, pp. 3534-3536, 2012.

[3] J. D. Sarmiento-Merenguel, R. Halir, X. Le Roux, C. Alonso-Ramos, L. Vivien, P. Cheben, E. Durán-Valdeiglesias, I. Molina-Fernández, D. Marris-Morini, D.-X. Xu, J. H. Schmid, S. Janz, and A. Ortega-Moñux, *"Demonstration of integrated polarization control with a 40 dB range in extinction ratio"*, Optica vol. 2, no. 12, pp. 1019-1023 2015.

ECIO 2016
18TH EUROPEAN CONFERENCE ON INTEGRATED OPTICS 2016
18–20 MAY | WARSAW | POLAND

# Coherence Comb Laser Sources: Quantum Dots, Packaging and Active Control

**Zhenguo LU**
National Research Council Canada

We have successfully developed several InAs/InP quantum-dot (QD) C-band coherence frequency comb laser sources with the frequency spacing from 10 GHz to 100 GHz with the total output power of up to 50 mW in telecommunication industry for Tb/s high speed optical transmission networking systems. In this talk, we will present our advanced in-house QD growth, laser chip design, nano-fabrication, characterization, packaging and electrical fast-feedback-loop control systems.

*Long abstract not available at the date of final printing.*

ECIO 2016
18TH EUROPEAN CONFERENCE ON INTEGRATED OPTICS 2016
18–20 MAY | WARSAW | POLAND

# Indium phosphide monolithic photonic integrated circuits for gas sensing applications

**S. Latkowski[1*], P.J. van Veldhoven[1], A. Hänsel[2], D. D'Agostino[1], H. Rabbani-Haghighi[1], B. Docter[3], N. Bhattacharya[2], P. Thijs[1], H. Ambrosius[1], M. Smit[1], K. Williams[1] and E.A.J.M. Bente[1]**

[1]COBRA Research Institute, Eindhoven University of Technology
De Zaale, 5612 AJ, Eindhoven, The Netherlands
[2]Optics Research Group, TU Delft, 2628 Delft, The Netherlands
[3]EFFECT Photonics B.V., Torenallee 20, Eindhoven, The Netherlands
[*]S.Latkowski@tue.nl

In order to extend the scope of potential applications for the generic photonics integration technology platforms [1] it is desired to widen the range of spectral bands covered by such integration technologies. Access to wavelengths in the mid-infrared range at around 2μm would make it particularly attractive for gas sensing applications due to presence of strong absorption lines of many gas species e.g. acetone and ammonia. Therefore, a development of long-wavelength (2 μm) active-passive monolithic integration technology on indium phosphide substrate with use of strained multi-quantum wells (MQW) was undertaken at the COBRA Research Institute [2]. Along with the technology development a novel tunable laser design featuring an asymmetric Mach-Zehnder interferometer (AMZI) based intra-cavity filter suitable for single line gas spectroscopy has been proposed [3]–[5] . The device has been fabricated within a multi-project wafer (MPW) run using such long-wavelength technology as presented in Fig. 1.

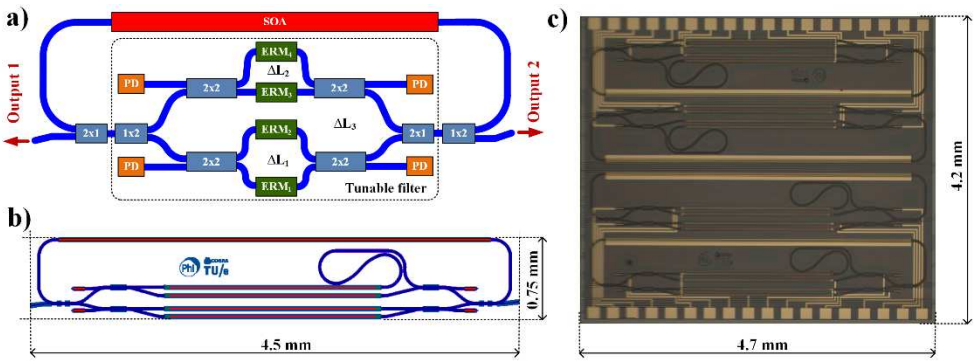



**Fig. 1 (a) A diagram of the extended cavity ring laser featuring an intracavity tunable wavelength filter based on nested asymmetric Mach-Zehnder interferometers (dotted box). The photonic integrated circuit (PIC) consists of several basic building blocks connected with passive waveguides (in blue): a semiconductor optical amplifier (SOA), multimode interference couplers (1x2, 2x2 MMI), electro-refractive modulators (ERM) and photodiodes (PD). (b) Mask layout of the laser cavity with a total area of 3.4 mm². (c) A microscope picture of a long-wavelength chip including four tunable lasers. The 20 mm² PIC was fabricated within a multi-project wafer run.**

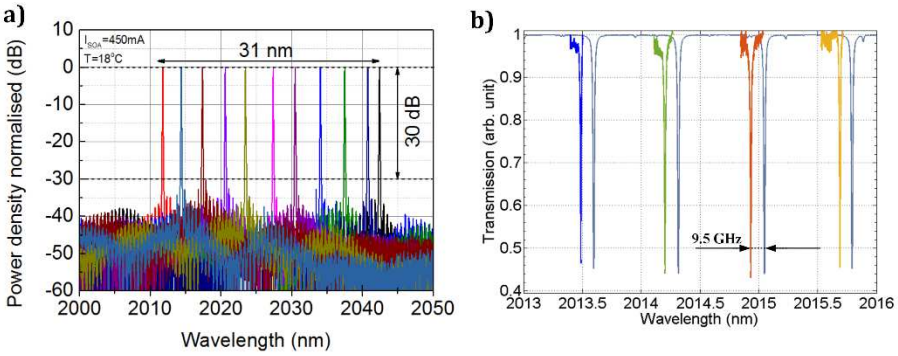



**Fig. 2 (a) Optical spectra recorded for a series of sets of reverse voltages applied to the ERMs with the injection current into the SOA and temperature kept constant at $I_{SOA}$=450 mA and T= 18 °C respectively. (b) Four absorption lines of carbon-dioxide recorded using the long-wavelength PIC laser overlapped (9.5GHz offset) with the simulated absorption spectrum.**

The fabricated PIC laser operating at DC current injection and at room temperature features a threshold current density of 3.4kA/cm$^2$ and delivers around 0.1mW of average output power coupled into the lensed fiber (~ 0.3mW ex-facet assuming a fiber coupling loss of ~5dB). The AMZI filter in a nested configuration allows for a record tuning range of 31 nm at around 2027nm Fig. 2(a). Such tuning bandwidth is achieved by applying a reverse bias voltage to four electro-refractive modulators (ERM) while the current injection into the semiconductor optical amplifier (SOA) section and the temperature of the chip are being held constant. The laser's feasibility for gas spectroscopy was evaluated in a gas spectroscopy experiment using a carbon-dioxide reference cell. Four individual absorption lines were targeted using the voltage controlled ERMs and the lasing wavelength was tuned across each line by scanning the current injected into the SOA section. The four absorption lines are presented in Fig. 2(b) overlapped with the absorption spectrum of carbon-dioxide simulated using the HITRAN database and parameters of the reference gas cell.

References

[1] M. Smit, et al. "An introduction to InP-based generic integration technology," Semicond. Sci. Technol., vol. 29, no. 8, p. 083001, Jun. 2014.

[2] S. Latkowski, P. Thijs, P. J. van Veldhoven, H. Rabbani-Haghighi, M. K. Smit, and E. A. J. M. Bente, "Small signal modal gain measurement of ridge waveguide semiconductor optical amplifiers operating at 2 µm suitable for active-passive integration," in 2013 IEEE Photonics Conference (IPC), 2013, pp. 258–259.

[3] S. Latkowski, M. Smit, and E. A. J. M. Bente, "Integrated tunable semiconductor laser geometry based on asymmetric Mach-Zehnder interferometers for gas sensing applications," in Proceedings of the 17th Annual Symposium of the IEEE Photonics Society Benelux Chapter, Mons, Belgium, 2012.

[4] S. Latkowski, A. Hansel, N. Bhattacharya, T. de Vries, L. Augustin, K. Williams, M. Smit, and E. Bente, "Novel Widely Tunable Monolithically Integrated Laser Source," IEEE Photonics J., vol. 7, no. 6, pp. 1–9, Dec. 2015.

[5] S. Latkowski, D. D'Agostino, P. J. van Veldhoven, H. Rabbani-Haghighi, B. Docter, H. Ambrosius, M. Smit, K. Williams, and E. A. J. M. Bente, "Monolithically integrated tunable laser source operating at 2µm for gas sensing applications," in Photonics Conference (IPC), 2015, 2015, pp. 535–536.

ECIO 2016
18TH EUROPEAN CONFERENCE ON INTEGRATED OPTICS 2016
18–20 MAY | WARSAW | POLAND

# Development of active-passive regrowth for butt-coupled lasers in membrane photonic integrated circuits

**Vadim POGORETSKIY*, Aura HIGUERA-RODRIGUEZ, Yuqing JIAO, Rene P.J. van VELDHOVEN, Jos J.G.M van der TOL, Dominik HEISS, Meint K. SMIT**
COBRA Research Institute, Technische Universiteit Eindhoven
De Zaale, Eindhoven, 5600 MB, The Netherlands
* v.pogoretskiy@tue.nl

**Introduction:** Photonic integration on membranes can be used to combine electronic and optical functionality. An InP membrane on Si (IMOS) [1] is an advantageous solution, since it can include lasers, detectors and waveguide devices. In order to scale down the footprint of active devices such as photonic crystal nanolasers (Fig. 1a.), active passive regrowth is necessary. This paper reports on the design of the active layer stack and development of an active-passive regrowth process for integrated active devices which are butt-coupled to membrane waveguides. A first realized structure with this technique is shown in Fig. 1b.

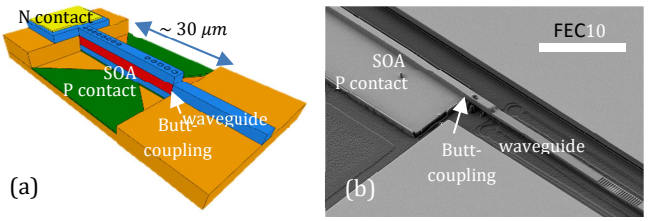



**Fig. 1. (a) Schematic of a laser butt-coupled to a waveguide; (b) SEM image of a realized structure.**

**Active layer stack design:** Electrical and optical confinement is provided by a double heterostructure with bulk InGaAs or InGaAsP as the active layer and doped InP as a barrier layer. We use bulk material in order to provide higher gain in small devices when cavity losses are large and high injection currents are necessary (Fig. 2a.). We carefully choose doping levels and thicknesses in order to make a tradeoff between technology and SOA performance. On the one hand, we need to isolate optically the active region and reduce cladding doping levels in order to reduce the internal loss of the SOA. On the other hand, we cannot afford a total thickness higher than 1 μm to perform high quality dry etching using a thin hard mask. Moreover, a thin layerstack and high doping of the cladding will minimize the series resistance of the device. Apart from that we need to include several sacrificial and etch stop layers (green in Fig.3a) in order to make successful regrowth possible. Optimized layer stack parameters are presented in Fig. 3a. Fig. 3b. shows the optical mode distribution in a designed layer stack. Fig. 3c. depicts loss and mode confinement dependence on SOA width for a chosen layerstack. In order to avoid multimode behavior we have to stay below 1 μm SOA width where we expect high loss and a low confinement factor. Thus, choosing an optimal layerstack is very important for a butt-coupled membrane integrated platform.

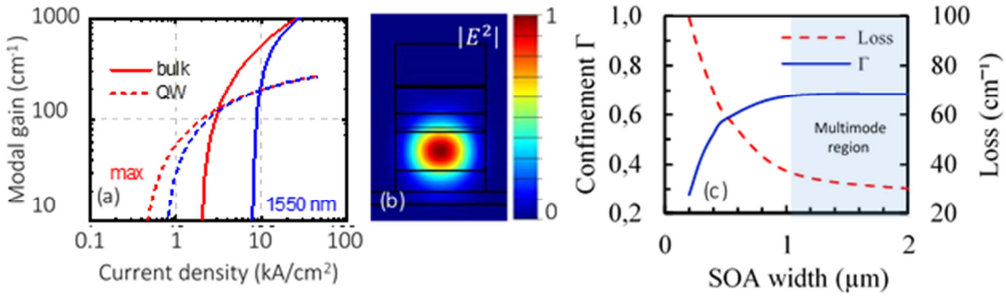



**Fig. 2. (a) Modal gain dependence on current density for bulk and quantum well active material; (b) mode distribution in SOA; (c) loss and mode confinement dependence on SOA width.**

**Active-passive regrowth:** Using MOCVD we first growth the active layer stack on top of a (100)-InP wafer. Then, we pattern active areas with 30 μm width and various length with optical lithography and apply a combination of dry and wet etching to remove etch stop layer and obtain atomic flat surface which will reduce loss in passive parts of the circuit. Finally, we regrow a 300 nm thick InP infill layer for the passive regions of the chip. On the active regions a 200 nm thick $Si_xN_y$ mask prevents further growth. We characterize the regrowth with cross-sectional SEM images as shown in Fig. 3. As a result of the wet etching process the $(0\bar{1}\bar{1})$ and $(01\bar{1})$ facets are shaped differently, typically characterized as dove tail and V-grove facets [2]. In the cross-sectional SEM we observed a gap (Fig. 3c) for the V-grove facet. This facet of the InGaAs compound does not allow InP to nucleate on its surface, thus creating the gap, which prevents light coupling. The dove tail facet, on the other hand, provides a homogeneous interface suitable for active-passive coupling, as shown in Fig. 3b.

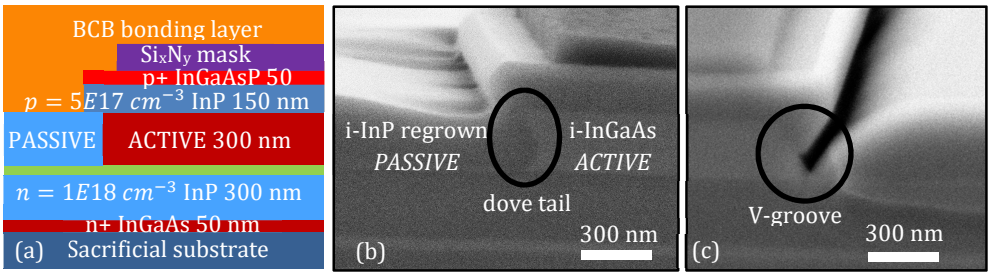



**Fig. 3. (a) Designed layer stack for butt-coupled IMOS platform; (b) SEM image of $(0\bar{1}\bar{1})$ facet (dove tail); (c) $(01\bar{1})$ facet (V-groove).**

**Conclusion:** In this work we have presented the successful active-passive regrowth for fabrication of small footprint membrane photonic integrated devices. Active passive regrowth allows us to fabricate lasers with a footprint below 30 μm². Fabrication of the butt-coupled lasers is currently ongoing. During the conference we will show more results of the fabricated devices.

**References**

[1] J. van der Tol, et al, "Photonic integration in indium-phosphide membranes on silicon (IMOS)," *IET Optoelectron.*, vol. 5, p. 89880M, 2014.

[2] S. Adachi, "Chemical Etching Characteristics of (001)InP," *J. Electrochem. Soc.*, vol. 128, no. 6, p. 1342, 1981.

[3] L. A. Coldren and S. W. Corzine, "*Diode lasers and photonic circuits*". 2012.

ECIO 2016
18TH EUROPEAN CONFERENCE ON INTEGRATED OPTICS 2016
18–20 MAY | WARSAW | POLAND

# On-Chip Multiple Colliding Pulse Mode-Locked Laser for Millimeter and Terahertz Wave Generation

**Carlos D. GORDON[1*], Mu Chieh LO[1], Robinson GUZMAN[1], Vinicio CORRAL[1], Guillermo CARPINTERO[1]**
[1]Universidad Carlos III de Madrid, Av. de la Universidad N°29, Madrid, 28911, Spain.
* ingcarlosgordon@gmail.com

We report a novel on-chip multiple colliding pulse mode-locked (ocMCPM) semiconductor laser source for the generation of an optical pulse train at millimeter wave frequency repetition rate, generating a repetition rate at a higher harmonic of the fundamental laser round-trip frequency. We demonstrate a repetition rate at 100 GHz (within the millimeter wave frequency range), using a resonator cavity length with fundamental repetition rate at 25 GHz. As the optical pulse train output is generated within the chip, thanks to integrated mirrors, further increases of the repetition rate are possible, through an optical clock multiplier (OCM) scheme, in order to reach 300 GHz, for terahertz wave generation.

Recent technology roadmaps point to the need of increasing the data rates used in wireless communication systems into the multi-gigabit-per-second to cope with the future needs based in current trends of the demand [1]. A current cost effective solution is to increase the carrier wave frequency into the millimetre (30 to 300 GHz) and terahertz (300 GHz to 3 THz) wave regions [2]. The difficulties to generate, amplify and modulate signals at these frequencies have been overcome by combining electronic with photonic techniques. Currently, most if not all of the reported wireless communication links operating above 100 GHz employ photonic generation of the carrier frequency, demonstrating different available techniques.

There are various photonic techniques to generate MMW and THz frequencies, among which optical heterodyning and pulsed techniques are commonly used. Pulsed sources are usually based on mode locked laser structures [3], having recently reported that it can increase the radiated emitted power about 7 dBm above heterodyning schemes [4]. Mode locked sources can either be passive or hybrid, depending on weather the pulse train is locked to an electronic reference. Passive mode locking requires only fixed direct current and reverse voltage to generate the pulsed signal, which lacks stability. The stability can be addressed through hybrid mode locking, in which the reverse voltage is combined with a continuous wave (CW) signal at the fundamental frequency. The stability is inherited from the electronic source, but is limited by the electrical modulation bandwidth, usually below 30 GHz. The aim of this work is to present the on-chip multiple colliding pulse mode-locked laser diode structure (ocMCPM) using multimode interference reflectors (MIRs). Thanks to active-passive integration technology, we realized these structures as a photonic integrated circuit (PIC).

The structure of the on-chip multiple colliding pulse mode-locked laser diode is sketched in Fig. 1(a). The ocMCPM´s assembly includes three semiconductor optical amplifiers (Lengths, LSOA 1 = 182 um, LSOA 2 = 348 um and LSOA 3 = 350 um), two saturable absorbers (Lengths, LSA 1/2 = LSA 1/4 = 20 um ) with four electrical isolators (Lengths, LISO = 20 um each) located on each side of the SAs as well as passive waveguides (LPW = 451.4 um) and two multimode interference reflectors on each end in order to build the resonator cavity. The total length of the cavity is L_cav = 1632 um

which offers a fundamental repetition rate of 25 GHz. Besides, the microscope photograph of the fabricated sample is shown in Fig. 1(b). Similarly, we present the block diagram of the future approach in order to multiply by four the repetition rate of an ocMCPM in Fig. 1(c) and the schematic of the OCM-x4 in Fig. 1(d) respectively.

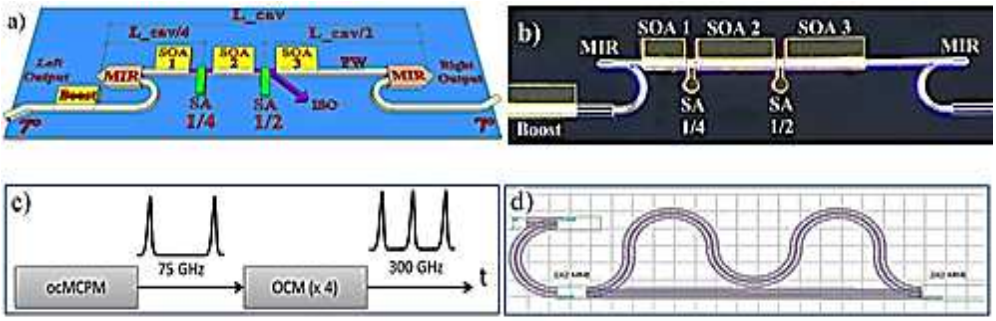



**Fig. 16. (a) Schematic of the ocMCPM structure. (b) Microscope photograph of the ocMCPM. (c) Block diagram of the future approach. (d) Schematic of the OCM-x4.**

The ocMCPM was characterized by choosing a bias condition, which exhibits this behaviour. The recorded optical spectrum for ocMCPM is depicted in Fig. 2(a). Moreover, the electrical characterization was carried out at the same bias condition. The electrical mode beating tone at 405 MHz is delivered by the Rohde & Schwarz FS-Z110 external mixer head working with the tenth harmonic which down converts the 100 GHz repetition rate of the ocMCPM. Fig. 2(b) shows the recorded electrical spectrum of the mode beating provided by the ocMCPM.

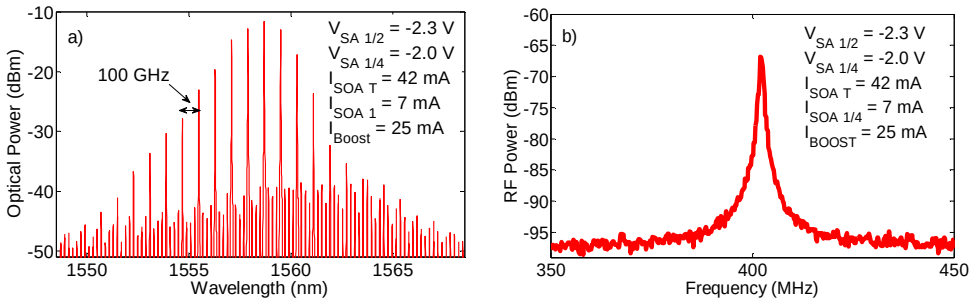



**Fig. 2. ocMCPM characterization. (a) Optical spectrum. (b) Electrical spectrum.**

References

[1] Ericsson Mobility Report. February (2015), http:// www.ericsson.com/mobility-report.

[2] A. Stohr, *Photonic millimeter-wave generation and its applications in high data rate wireless access*, IEEE Top. Meeting on Microwave Photonics, 5-9 Oct. 2010.

[3] T. Nagatsuma, et. al, *Photonic Generation of Millimeter and Terahertz Waves and Its Applications*, Applied Electromagnetics and Communications, pp. 1-4, 2007.

[4] L. Moeller, A. Shen, C. Caillaud, and M. Achouche, *Enhanced THz generation for wireless communications using short optical pulses*, In Infrared, Millimeter, and Terahertz Waves, pp. 1-3, 2013.

ECIO 2016
18TH EUROPEAN CONFERENCE ON INTEGRATED OPTICS 2016
18–20 MAY | WARSAW | POLAND

# Waveguide coupled high-Q micro-optical resonators

**Simone BERNESCHI[1], Immacolata Angelica GRIMALDI[2], Silvia SORIA[1], Romeo BERNINI[2], Gualtiero NUNZI CONTI[1]***

[1]Institute of Applied Physics "N. Carrara",CNR-IFAC, Via Madonna del Piano 10, 50019 Sesto Fiorentino (FI), Italy

[2]Institute for Electromagnetic Sensing of the Environment, CNR-IREA, Via Diocleziano 328, 80124 Napoli, Italy

* g.nunziconti@ifac.cnr.it

For practical applications, in order to fully exploit the unique properties of Whispering Gallery Mode (WGM) micro-optical resonators, a critical point is an efficient and robust coupling of the light to the cavity [1,2]. We present the results of our studies on coupling methods based on integrated waveguides, with particular reference to the case of crystalline waveguides ($LiNbO_3$) and polymeric waveguides (SU8 photoresist). In both cases the WGM resonators were made of the same material of the waveguides and Fig. 1 shows pictures of the two systems with a $LiNbO_3$ disk (Fig. 1a), and a SU8 bottle resonator (Fig. 1b).

After the first demonstration of waveguide based coupling obtained by using an ion-exchanged waveguide (fabricated in BK7 glass and coupled to a BK7 microsphere [3]), we have been working on this type of approach mainly for two different applications, RF photonics and biosensing. In the first case, in order to develop innovative optoelectronic oscillators we have fabricated high-Q $LiNbO_3$ disk resonators of few millimeters in diameter. Aiming to achieve improved device compactness and robustness we have implemented coupling from fiber pigtailed $LiNbO_3$ waveguides, successfully developing a system which is all in guided optics architecture [4]. The waveguides are made by Ti:diffusion in X-cut lithium niobate substrates while the high-Q disks are made from commercial Z-cut lithium niobate wafers by polishing the edges into a spheroidal profile. An example of high-Q resonances in excess of $10^8$ around 1550 nm is shown in Fig. 2a.

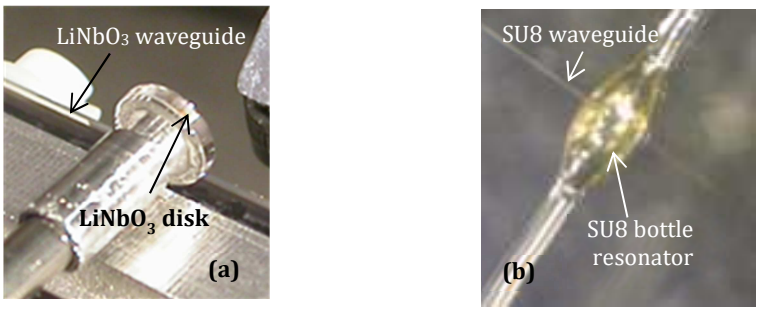



**Fig. 5. Photo of a $LiNbO_3$ disk coupled to a Ti:diffused $LiNbO_3$ waveguide (a), and of a SU8 bottle resonator coupled to a ridge SU8 polymer waveguide made on PMMA substrates (b).**

The experience developed using WGM resonators as micro-optical transducer for biosensing suggested us that a polymer based integrated platform could be an ideal approach for such application. We have recently implemented and optimized a simple, self-assemble process to fabricate bottle micro-resonators in SU-8 polymer [5]. The method is based on dispensing a droplet of SU-8 polymer photoresist on a fiber stem by a syringe pump followed by an UV curing step. In order to excite the WGMs in the

microbottle resonators, we fabricated single mode SU-8 ridge waveguides by SU-8 spin coating on a PMMA substrates followed by a standard photolithograpic process. The waveguides were designed and fabricated 3 μm wide × 2 μm thick in order to be single mode at 1550 nm. The development of this solid, fully polymeric platform based on integrated waveguide is essential for implementing a convenient and reliable WGM-based sensing device (which could be critical to implement with standard silica fiber taper based couplers because of their inherent instability and mechanical fragility). The measured Q factors were in excess of $10^4$ (see spectrum of Fig. 2b), which represents the basic limit due to material absorption.

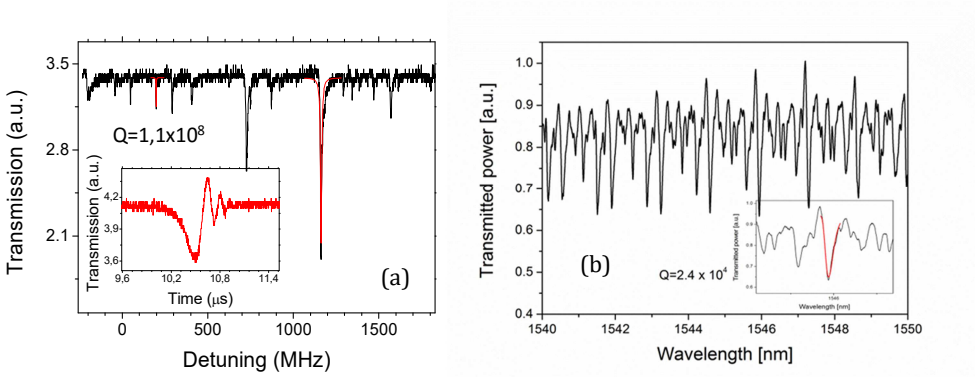



**Fig. 2. WGMs spectra around 1550 nm of a waveguide coupled high-Q $LiNbO_3$ disk (with a resonance ringdown measurement in the inset) (a) and of a SU8 bottle resonator (with a magnified resonance in the inset) (b).**

The authors thank Dr. D. Farnesi and Dr. F. Baldini from CNR-IFAC and Dr. G. Testa from CNR-IREA for useful discussions. This research was partially supported by Italian MIUR-FIR program No. RBFR122KL1, and by Ente Cassa di Risparmio di Firenze project No. 2014.0770A2202.8861. S. Berneschi acknowledges the European Community for its funding within the framework of the projects Hemospec (FP7 - 611682).

References

[1] D. Ristić, A. Rasoloniaina, A. Chiappini, P. Féron, S. Pelli, G. Nunzi Conti, M. Ivanda, G. C. Righini, G. Cibiel, M. Ferrari, *About the role of phase matching between a coated microsphere and a tapered fiber: experimental study*, Opt. Express vol. 21, pp. 20954-20963, 2013

[2] D. Farnesi, G. C. Righini, A. Barucci, S. Berneschi, F. Chiavaioli, F. Cosi, S. Pelli, S. Soria, C. Trono, D. Ristic, M. Ferrari, G. Nunzi Conti, *Coupling light to whispering gallery mode resonators*, in Proceedings SPIE 9133, pp. 913314-1-9, 2014

[3] Y. Panitchob, G. Senthil Murugan, M. N. Zervas, P. Horak, S. Berneschi, S. Pelli, G. Nunzi Conti, and J. S. Wilkinson, *Whispering Gallery Mode Spectra of Channel Waveguide Coupled Microspheres*, Opt. Express, vol. 16, pp. 11066-11076, 2008

[4] G. Nunzi Conti, S. Berneschi, F. Cosi, S. Pelli, S. Soria, G. C. Righini, M. Dispenza, A. Secchi, *Planar coupling to high-Q lithium niobate disk resonators*, Opt. Express, vol. 19, pp. 3651-3656, 2011

[5] I. A. Grimaldi, S. Berneschi, G. Testa, F. Baldini, G. Nunzi Conti, R. Bernini, *Polymer based planar coupling of self-assembled bottle microresonators*, Appl. Phys. Lett., vol. 105, pp. 231114-1-4, 2014

ECIO 2016
18TH EUROPEAN CONFERENCE ON INTEGRATED OPTICS 2016
18–20 MAY | WARSAW | POLAND

# Highly-Efficient Subwavelength Engineered Grating Couplers for Silicon-on-Insulator Waveguides

**D. Benedikovic[1,*], C. Alonso-Ramos[1], P. Cheben[2], J.H. Schmid[2], S. Wang[2], D.-X. Xu[2], R. Halir[3], A. Ortega-Moñux[3], L. Vivien[1], J. Lapointe[2], S. Janz[2], J.-G. Wangüemert-Pérez[3], I. Molina-Fernández[3], J.-M. Fédéli[4], and M. Dado[5]**

[1]Institut d'Electronique Fondamentale, Université Paris Sud, CNRS, UMR 8622, Université Paris-Saclay, Bat. 220, Orsay Cedex, France
[2]National Research Council Canada, 1200 Montreal Road, Ottawa, Canada
[3] Universidad de Málaga, Dpto. de Ingeniería Comunicaciones, 29010 Málaga, Spain
[4]CEA-LETI, Minatec, CEA-Grenoble, 38054 Grenoble, France
[5]University of Žilina, Dept. of Telecommunications and Multimedia, 010 26 Žilina, Slovakia
[*] daniel.benedikovic@u-psud.fr

**Abstract:** We present experimental results of efficient subwavelength index engineered surface grating couplers, developed in a standard 220-nm SOI substrate. Grating couplers are fabricated using a single full etch or a dual etch process (full etch and 70nm shallow etch). The measured efficiency of -2.2 dB, -2.5 dB, and -0.7 dB are reported for single-etch couplers without and with metal reflector in the near-IR wavelengths. We demonstrate a peak coupling efficiency of -1.3 dB for a novel and flexible dual-etch grating coupler with interleaved deep and shallow etched trenches.

**Introduction:** Grating couplers are an effective approach to couple light to or from integrated circuits, enabling flexible placing of the interface on the chip surface and automated wafer scale testing [1-4]. In these structures, the directionality, i.e. the amount of power coupled towards an optical fibre, is an important parameter that determines the overall coupling efficiency. Grating directionality strongly depends on the thickness of the silicon and the buried oxide (BOX) layers. Thicker Si waveguides yield higher directionality [2], while the 220 nm Si thickness is usually used in silicon photonics foundry offerings [3]. The directionality can also be improved by specialized gratings, at the expense of a more complex fabrication [1-5].

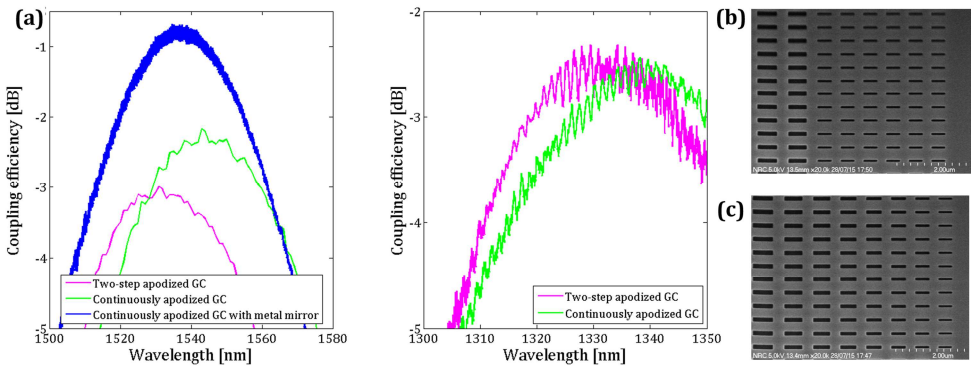



**Fig. 18. (a) Measured coupling efficiency of single-etch subwavelength engineered grating couplers near 1.55 μm and 1.3 μm wavelengths. SEM images of fabricated devices: (b) two-step and (c) continuously apodized grating couplers.**

**Single-etch grating couplers:** We recently designed and fabricated a series of efficient single-etch grating couplers for a standard 220-nm-thick Si layer over 3-μm and 2-μm thick BOX layers [6-8]. We found that the directionality, can be improved by optimizing the radiation angle. Specifically, we demonstrated that the thin film interference from the bottom oxide layer is maximized for a coupling angles of 27° (3-μm BOX, near 1.55

μm) and 33° (2-μm BOX, near 1.3 μm) off normal incidence. The high-directionality grating geometries are apodized using subwavelength grating (SWG) refractive index engineering [5-8]. This allows single-etch fabrication and enhanced coupling performance. Fig. 1(a) shows measured coupling efficiencies of apodized grating couplers, with peaks of -2.2 dB and -2.5 dB in the respective spectral bands. Figs. 1(b) and (c) show scanning electron microscope (SEM) images of fabricated structures. In addition, by utilizing the CMOS-compatible process of backside engineering and metal layer deposition, we reported the first sub-decibel coupling efficiency of -0.7 dB in 220-nm SOIs and single-etch fabrication [7].

**Dual-etch grating couplers:** We also developed a grating coupler with an ultra-high intrinsic directionality of 95% [9]. The structure comprises interleaved deep and shallow etched trenches. The vertical schematic and SEM image are shown in Fig. 2(a) and (b). An important practical benefit is that high-directionality is achieved independently on the BOX thickness [9,10]. The coupler also includes short SWG impedance-matching section (see Fig. (b)) to reduce back-reflections at the junction between the access waveguide and the grating. The coupler was fabricated in a 220-nm-thick SOI with 3-μm-thick BOX layer, with a measured efficiency of -1.3 dB at 1.55 μm, as shown in Fig. 2(c).

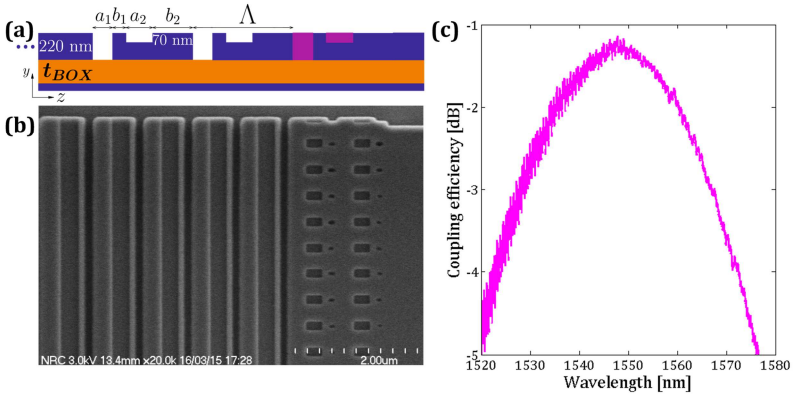



**Fig. 2. (a) Schematic of dual-etch grating coupler with interleaved deep and shallow etched trenches. (b) SEM images of the fabricated structure. (c) Measured coupling efficiency.**

References

[1] A. Mekis, et al., IEEE J. Sel. Top. Quant. Electron. 17(3), pp. 597-608, 2011
[2] D.-X. Xu, et al., IEEE J. Sel. Top. Quant. Electron. 20(4), pp. 189-205, 2014
[3] A.-J. Lim, et al., IEEE J. Sel. Top. Quantum Electron. 20(4), pp. 405-416, 2014
[4] Ch. Kopp, et al., IEEE J. Sel. Top. Quantum Electron. 17(3), pp. 498-509, 2011
[5] R. Halir, et al., Laser Photon Rev. 9(1), pp. 25-49, 2015
[6] D. Benedikovic, et al., Laser Photon Rev. 8(6), pp. 93-97, 2014
[7] D. Benedikovic, et al., Opt. Express 23(17), pp. 22628-22635, 2015
[8] D. Benedikovic, et al., Opt. Express, to be submitted, 2016
[9] C. Alonso-Ramos, et al., Opt. Lett. 39(19), pp. 5351-5354, 2014
[10] D. Benedikovic, et al., Opt. Lett. 40(18), pp. 4190-4193, 2015

ECIO 2016
18TH EUROPEAN CONFERENCE ON INTEGRATED OPTICS 2016
18–20 MAY | WARSAW | POLAND

# Optical frequency domain reflectometry for characterization of waveguide crossings

**Dan ZHAO[1*], Dzmitry PUSTAKHOD[1], Luc AUGUSTIN[1,2], Kevin WILLIAMS[1] and Xaveer LEIJTENS[1]**
[1]Eindhoven University of Technology, Den Dolech 2, 5612 AZ, Eindhoven, the Netherlands
[2]Smart Photonics, Horsten 1, 5612 AX, Eindhoven, the Netherlands
[*]d.zhao@tue.nl

**Abstract:** We have analysed crossings of shallow etched waveguides with a self-calibration high-accuracy optical frequency domain reflectometry method. The power reflection coefficient of crossings was measured to be $(1.4 \pm 0.6) \cdot 10^{-5}$.

**Introduction:** In photonic integrated circuits (PICs) spurious reflections may play an important role, especially for circuits containing active components. Properly designed waveguide crossings have near 100% transmission and very small reflections. These small reflections are difficult to characterize and little has been published. Optical frequency domain reflectometry (OFDR) is a powerful method for characterization of small localized reflections in PICs[1]. In this work, we develop a self-calibration high-accuracy OFDR method to characterize the power reflection coefficient $R$ of shallow etched waveguide crossings. The samples were fabricated by Smart Photonics through the JePPIX.eu multi-project wafer service.

**The OFDR system:** The schematic diagram of the OFDR system in Mach-Zehnder configuration for characterization of waveguide crossings is shown in Fig. 1. Light from a swept tunable laser is coupled into the sample which has a 4600 μm long shallow etched straight waveguide with 8 crossings at distances 1170, 1200, 2250, 2350, 2470, 3400, 3850 and 3950 μm from the front facet, respectively. The intensity modulations resulting from the interferences between the direct signal, acting as reference, and the signals with multiple reflections between cleaved facets and waveguide crossings are recorded by the power meter when sweeping the tunable laser. Taking the Fast Fourier transform (FFT) of the output signal, it is then possible to determine the position and the reflectivity of the crossings. A wavelength span of 120 nm with a step of 0.01 nm is used, which contributes to a high theoretical resolution $\delta L = c/2n_g\Delta f$ of about 3 μm[2].

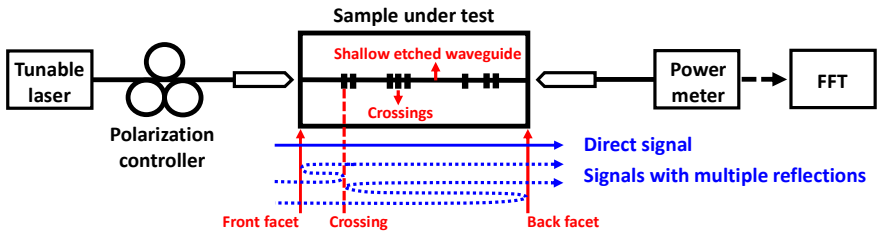



**Fig. 19. The schematic diagram of the OFDR system in Mach-Zehnder configuration.**

**Results and discussions:** The FFT of the measured signal is normalized to the maximum intensity and is shown as a function of cavity length $L$ in Fig. 2(a). The positions of the facets and crossings match accurately with the design values. In this figure the group index $n_g$ is assumed to be constant. The relative intensity $RI$ of the back facet is underestimated as $-17$ dB, much lower than the calculated value of

$-13.23 \pm 1.36$ dB according to $RI = |r_f|^2 e^{-2\alpha\Delta L}$[2], where $r_f = \sqrt{0.328 \pm 0.01}$ is the reflection coefficient of each facet, $\alpha$ is the propagation loss measured to be $2.1 \pm 0.3$ dB, $\Delta L$ is the chip length measured to be $4600 \pm 15$ µm. The accuracy can be much improved by including the quadratic term in the dispersion of $n_{\text{eff}}$ versus wavelength $\lambda$. The result is shown in Fig. 2(b), with a relative intensity of the back facet of $-12.32$ dB. We use this method to derive the reflection coefficient of the waveguide crossings from eq. (1)[2] based on the condition that the crossing reflections are much lower than those from the facets, $R = |r_c|^2 \ll |r_f|^2$:

$$r_c = RI_c/(r_f e^{-2\alpha z_c}), \tag{1}$$

where $z_c$ is the actual position of the crossings. The power reflectivity of the crossings is analysed to be $(1.4 \pm 0.6) \cdot 10^{-5}$ by taking into account the variations from each crossing and the parameter errors. A minimum design distance of 30 µm between crossings can be resolved, as shown in the inset. In Fig. 2(c), the group index $n_g(\lambda)$ is extracted from simulations and measurements using the OFDR analysis, by doing the FFT for a small portion of the spectrum per step, according to eq. (2)[2].

$$n_g(\lambda) = \big(\tau_b(\lambda) - \tau_f(\lambda)\big)c/\Delta L, \tag{2}$$

where $\lambda$ is the central wavelength of each portion of the spectrum, $\tau_f$ and $\tau_b$ are the group delay for front and back facet reflections. The value of $n_g(\lambda)$ obtained from simulation matches perfectly with the modelled refractive index[3], which therefore validates the method. The coefficients of the Taylor expansion of $n_g(\lambda)$ and $n_{\text{eff}}(\lambda)$ can be derived from the measured $n_g(\lambda)$ from the OFDR system[4].

$$n_g(\lambda) = a - b\lambda_0 - 2c(\lambda_0 \cdot \Delta\lambda),\ n_{\text{eff}}(\lambda) = a + b\Delta\lambda + c(\Delta\lambda)^2 \tag{3}$$

The derived $n_{\text{eff}}(\lambda)$ is used for improving the accuracy of analysis shown in Fig. 2b.

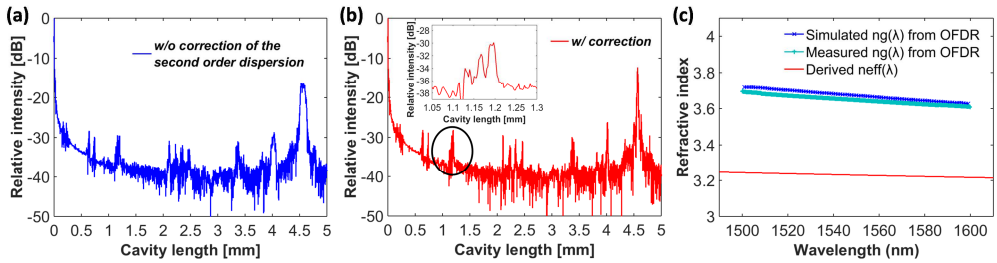



**Fig. 2. OFDR measurements of the waveguide crossings.**

**Conclusion and acknowledgement:** We demonstrate a high-accuracy OFDR analysis to measure the power reflectivity of waveguide crossings: $R = (1.4 \pm 0.6) \cdot 10^{-5}$. The position of the crossings is detected with a spatial resolution better than 30 µm. We acknowledge support by the Dutch Technology Foundation STW for project 13538.

## References

[1] B. J. Soller et. al, Optics Express, vol. 13, no. 2, pp. 666-674, 2005
[2] D. Melati et. al, Advances in Optics and Photonics, vol. 6, no. 2, pp. 156–224, 2014
[3] F. Fiedler and A. Schlachetzki, Solid-State Electronics, vol. 30, no. 1, pp. 73-83, 1987
[4] S. Dwivedi et. al, Journal of Lightwave Technology, vol. 33, no. 21, pp. 4417-4477, 2015

ECIO 2016
18TH EUROPEAN CONFERENCE ON INTEGRATED OPTICS 2016
18–20 MAY | WARSAW | POLAND

# Highly efficient nonlinear waveguides in $LiNbO_3$ fabricated by a combination of Soft Proton Exchange (SPE) and E-beam writing.

**Maxim NERADOVSKIY[1,3*], Dmitry CHEZGANOV[1,2], Lubov GIMADEEVA[1], Evgenii VLASOV[1], Vsevolod KVASHNIN[1], Elizaveta KOLCHINA[1], Andrey AKHMATKHANOV[1,2], Maria CHUVAKOVA[1], Denis ALIKIN[1], Herve TRONCHE[3], Florent DOUTRE[3], Pascal BALDI[3], Vladimir Ya. SHUR[1,2], Marc P. DE MICHELI[3]**

[1]Institute of Natural Sciences, Ural Federal University, 620000, Ekaterinburg, Russia
[2]Labfer Ltd., 620014, Ekaterinburg, Russia,
[3]LPMC, University of Nice Sophia-Antipolis, 06100 Nice, France
* marc.de-micheli@unice.fr

Using an E-Beam writing process we produced high quality periodical domains in SPE lithium niobate waveguides. In SHG experiment we got up to 47%/W.cm$^2$ conversion efficiency which is comparable to similar waveguides where the domains are obtained by other techniques.

The samples under investigation is a 0.5-mm-thick Z-cut CLN plates. The SPE process [1] was carried out in benzoic acid diluted with 3.1% of lithium benzoate (LB) at 300 °C for 72 hours, using a $SiO_2$ mask on Z– polar surface to fabricate the channel waveguides with different width along the X-crystallographic axes. Using a scanning electron microscope (Auriga Crossbeam workstation, Carl Zeiss) equipped with an electron-beam (e-beam) lithography system (Elphy Multibeam, Raith), we produced domain structures with various periods. The maximum length of written PPLN segment was 1.5 mm. Longer segments were obtained by moving the sample and writing several segments. The domain patterns were visualized by piezoresponse force microscopy (PFM) and confocal Raman microscopy (CRM).

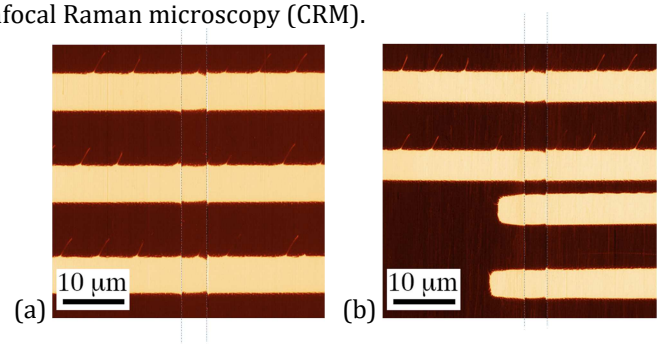



**Fig. 1. PFM image of SPE waveguide (vertical) going through periodical domain structure (horizontal): dark – initial state, white – written domain. (a) inside one segment of writing (b) illustration of the stitching error between two written segments when the nonlinear grating is obtained by concatenation of several 1.5 mm PPLN sections.**

Typical PFM images of the SPE waveguide going through periodical structure is presented in Fig. 1, which shows that the e-beam poling process is nearly not affected by the presence of the waveguide in contrary to what has been observed for E-field poling [2]. Moreover, we did not observe any nanodomains, contrarily to what we obtained earlier [3]. The other observed features of the written domain patterns

("fingers") can be attributed to highly non-equilibrium switching conditions during e-beam irradiation caused by gradient of spontaneous polarization in SPE layer [4].

For the SHG experiments, we used a TUNICS T100S-HP tunable laser with a fiber amplifier delivering 80mW within the wavelength range 1535 to 1570 nm. The SHG spectrums of waveguides of different widths and a 1.5 mm PPLN section are presented in Fig. 2a. The SHG efficiency was up to 47%/(W·cm$^2$) as high as what is obtained in PPLN waveguides produced by other techniques. The FWHM of the SHG spectra is in good agreement with the calculated one. The observed wavelength shift corresponds to the influence of the waveguide width on the effective indices of the modes.

We also characterized waveguides going through 6mm PPLN sections (4 writing segments) and presenting some stitching errors (Fig. 1b). In this case we observed a similar conversion efficiency and as expected a narrower SHG spectra but also multiple SH pics which are not completely explained yet (Fig. 2b).

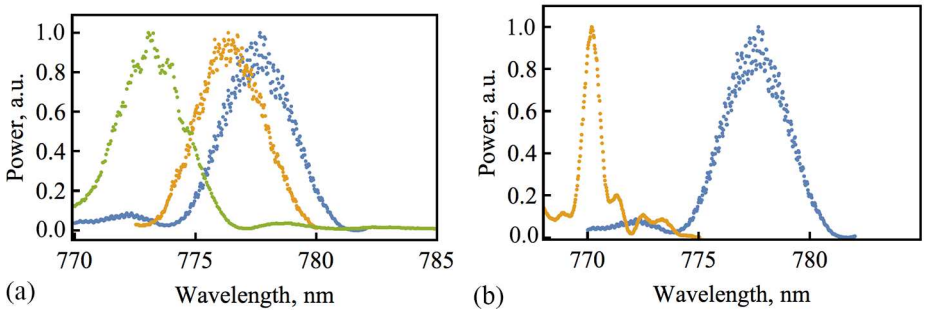



**Fig. 2. SHG spectra for SPE waveguides. Parameters: (a) waveguides width 5 μm (green), 7 μm (orange), and 8 μm (blue). Period of pattern 16.2 μm, length of periodically poled section – 1.5 mm. (b) Blue spectrum – the width of the waveguide is 8 μm, the period of PPLN is 16.2 μm, the length of PPLN is 1.5 mm; orange spectrum – the width of the waveguide is 5 μm, the period of PPLN is 16.0 μm, the length of PPLN is 6.0 mm.**

In conclusion, this work shows that it is possible to get state of the art SH conversion efficiency by writing the periodic domains after the waveguides fabrication. This is of capital interest for device combining nonlinear section with more complicated circuits.

The equipment of the Ural Center for Shared Use “Modern nanotechnology” UrFU was used. The research was made possible in part by RFBR (15-32-21102-mol_a_ved) and by Government of the Russian Federation (Act 211, Agreement 02.A03.21.0006).

References

[1] L. Chanvillard, et al., *Soft proton exchange on periodically poled $LiNbO_3$: A simple waveguide fabrication process for highly efficient nonlinear interactions,* Appl. Phys. Lett., vol. 76, p. 1089, 2000

[2] M. Neradovskiy, et al., *Investigation of domain kinetics in congruent lithium niobate modified by proton exchange*, Ferroelectrics, vol. 496, in Press

[3] M. Neradovskiy, et al., *Fabrication of SPE Waveguides on PPLN: Formation of Nanodomains and Their Impact on the SHG Efficiency*, Ferroelectrics, vol. 476, p. 127, 2015

[4] V. Ya. Shur, et al., *Micro- and nano-domain engineering in lithium niobate*, Appl. Phys. Rev., vol. 2, p. 040604, 2015

ECIO 2016
18TH EUROPEAN CONFERENCE ON INTEGRATED OPTICS 2016
18–20 MAY | WARSAW | POLAND

# A new hybrid fibre / planar platform for optics, offering ultralow loss and robust integration

**Peter G.R. SMITH*, Christopher HOLMES, Stephen G. LYNCH, James C GATES, Sam. A. BERRY, Teresa I. FERREIRO, Alexander JANTZEN**

Optoelectronics Research Centre, University of Southampton, Highfield, Southampton, SO17 1BJ, United Kingdom
* peter.smith@soton.ac.uk

A novel hybrid optical fibre / planar platform is presented. The approach offers exceptionally low losses <0.003 db/cm and physical robustness. The approach is based on a combination of flame hydrolysis deposition onto an existing bare fibre laid upon a silica-on-silicon type substrate. Example devices include an anemometer and a narrow line laser based on external Bragg gratings.

This invited talk describes the development of a new concept in integrated optics that combines many of the advantages of optical fibres (eg low losses, and fusion splicing) with the stability and integrated aspects of conventional integrated optics. The new approach combines a well-established technology (flame hydrolysis deposition) with conventional optical fibres. The resulting devices, with optical waveguides permanently bonded to a silica-on-silicon substrate offer potential for many applications.

The new technique involves placing an existing optical fibre onto an oxidised silicon wafer, and then depositing oxide glass soot (silica doped with boron, germanium and phosphorous), to provide a glass that is chemical similar to the optical fibre itself. Upon sintering the fibre becomes permanently welded to the surface using the miscible optical grade glass.

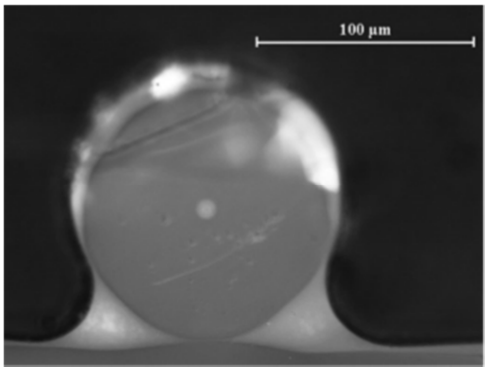



**Fig. 8. Showing SEM image of hybrid planar fiber in end-on view. Note that the core of the single mode fiber is visible.**

The resulting structures are extremely robust, and capable of further processing including the addition of Bragg gratings by laser UV writing, are robust enough to allow high quality polishing, and additionally can make use of physical processing steps such as machining and dicing to create novel structures..

This talk will review the basic concepts, provide data on the measured losses. In this regard the novel fibre offers potential for much lower losses than conventional

integrated optics. This is because fibre losses can routinely be below 0.2dB/km whereas planar waveguide losses are usually of order 0.1dB/cm suggesting up to $10^5$ possible loss reduction. Measurements using Bragg gratings suggest that losses are <0.003dB/cm for our new devices.

To date, applications of the new approach have included the realization of an anemometer [1], and the use of the hybrid system in the realization of an external Bragg cavity semiconductor laser [2]. All the devices to date have been simple linear configurations, and suggestion as to how to extend to more complex structures will be presented.

References

[1] Christopher Holmes, James C. Gates, and Peter G. R. Smith, "Planarised optical fiber composite using flame hydrolysis deposition demonstrating an integrated FBG anemometer," Opt. Express 22, 32150-32157 (2014)

[2] Stephen G. Lynch, Christopher Holmes, Sam A. Berry, James C. Gates, Alexander Jantzen, Teresa I. Ferreiro, and Peter G. R. Smith, "External cavity diode laser based upon an FBG in an integrated optical fiber platform," Opt. Express **24**, 8391-8398 (2016)

ECIO 2016
18TH EUROPEAN CONFERENCE ON INTEGRATED OPTICS 2016
18–20 MAY | WARSAW | POLAND

# Overview of Laser Sources for Silicon Photonic Transceivers

**Sylvie MENEZO**[1*]
[1] CEA-Leti, Minatec Campus, Grenoble, 38054 Cedex 9, France
* sylvie.menezo@cea.fr

Several strategies have been adopted and are still being developed for providing Si-Photonic Integrated Circuits with lasers. "Hybrid integration" architectures (integration of processed and finished III-V chips, e.g. SOAs and Lasers) and "Heterogeneous integration" schemes (integration of unprocessed III-V material on Silicon, followed by wafer level processing) will be reviewed and compared.

References

[1] Peter De Dobbelaere, *Light source approach for silicon photonics transceivers*, ECOC Workshop, Sept. 2014.
[2] A. J. Zilkie, *Power-efficient III-V/Silicon external cavity DBR lasers*, OPTICS EXPRESS, vol. 20, n° 21, 2012
[3] Jae-Woong Nah, e.a*., Flip chip Assembly with Sub-micron 3D Re-alignment via Solder Surface Tension*, Electronic Components & Technology Conference (ECTC), 2015
[4] Shinsuke Tanaka, e.a., *Four-Wavelength Silicon Hybrid Laser Array with Ring-Resonator Based Mirror for Efficient CWDM Transmitter*, in Proceedings of the OFC Conference, OTh1D.3, 2013
[5] Jin Hyoung Lee, e.a*., High power and energy-efficient WDM Si/III-V hybrid external cavity lasers*, in Proceedings of the 'Optical Interconnect Conference', TuB2, 2014
[6] Tin Komljenovic, e.a., *Widely Tunable Narrow-Linewidth Monolithically Integrated External-Cavity Semiconductor Lasers*, IEEE JSTQE, VOL. 21, NO. 6, Nov-Dec 2015
[7] Daniel Sparacin and Greg Fish, *Uniting silicon and InP to make versatile, low cost photonic chips*, www.compoundsemiconductor.net, Industry Photonic Integration, 2013
[8] Sylvie Menezo, e.a., *Hybrid III-V on Silicon Lasers: Heterogeneous 200mm-wafer-level Integration for WDM-Dense-optical-interconnects*, in Proceedings of the 'IEEE Compound Semiconductor Integrated Circuit Symposium (CSICS)', Oct. 2014
[9] Hélène Duprez, e.a., *Heterogeneously Integrated III-V on Silicon Distributed Feedback Lasers at 1310 nm*, in Proceedings of OFC 2015.
[10] Guang-Hua Duan, e.a., *Hybrid III–V on Silicon Lasers for Photonic Integrated Circuits on Silicon*, IEEE JSTQE, Vol. 20, n°. 4, 2014
[11] Po Dong, e.a., *Novel integration technique for silicon/III-V hybrid laser*, OPTICS EXPRESS, vol. 22, n° 22, 2014
[12] Timothy Creazzo, *Integrated tunable CMOS laser*, OPTICS EXPRESS, vol. 21, n°23, 2013
[13] Shinji Matsuo, *Excelling in the efficiency of lasers formed on silicon*, in Proceedings of the 'PIC International Conference', Brussels, Feb. 2016
[14] Siming Chen, e.a., *Electrically pumped continuous-wave III–V quantum dot lasers on silicon*, Nature Photonic Letter, DOI: 10.1038/NPHOTON.2016.21, 2016

ECIO 2016
18TH EUROPEAN CONFERENCE ON INTEGRATED OPTICS 2016
18–20 MAY | WARSAW | POLAND

# High-Optical-Quality Oxide-Free InP-on-Si Hybrid Interface

**Anne Talneau, I. Sagnes and G. Patriarche**
Laboratoire de Photonique et de Nanostructures, route de Nozay, F-91460 Marcoussis
Corresponding author: anne.talneau@lpn.cnrs.fr

**Abstract:** Oxide-free bonding of InP on Si has already demonstrated a perfect crystallographic interface, without defects, amorphization or voids, the dislocations necessary to accommodate the large lattice mismatch being located in the grain boundary that does not extend further than a single atomic layer [1]. Here we demonstrate through the sensitive measurement of propagation losses of a hybrid mode supported by a hybrid shallow ridge and strongly sensing the hybrid interface that the oxide-free hybrid interface does have a perfect optical quality: no significant additional propagation losses could be measured compared to an oxide-mediated bonded hybrid waveguide or a comparable monolithic waveguide.

The future of all optical networks links relies upon hybrid silicon photonics, wherein III-V semiconductors provide light emission and amplification that silicon is not able to efficiently perform. Bonding them without intermediate layer allows electrical injection through the hybrid interface [2-3], which opens the route to all optical and electrical 3D integration. For efficient device performances, such an oxide-free hybrid interface has to demonstrate no optical losses for the propagating modes which strongly interact with the hybrid interface, being near the mode profile antinode in usual designs.

Previous optical characterization was dedicated to optical functionalities related to the nanostructuration of the silicon waveguide [4-5]. In order to consider only the propagation losses introduced by the hybrid interface, without additional contribution related to the modal structure arising from nanostructuration, we have produced hybrid shallow ridges fabricated on an InP membrane bonded on a SOI wafer. Propagation losses then originate from both the etched walls and the hybrid interface.

We have measured 3 different shallow ridge waveguides: (i)- oxide-free bonded hybrid waveguides, (ii)- thin-oxide-mediated bonded hybrid waveguides, and (iii)- monolithic InP waveguides, both (ii) and (iii) being references. We took care to use shallow ridge geometries having comparable horizontal extent of the mode.

Device (i) is achieved with oxide-free surfaces preparation and oxide-free annealing at 500°C during 90 min. Oxide-mediated bonding is performed including a 2 nm-thick $SiO_2$ layer deposited by ALD (Atomic Layer Deposition) on both InP and Si, and annealing at 300°C during 3 h [6]. For both cases, a 400 nm-thin InP membrane is bonded on top of the 300nm-thick Si guiding layer on a SOI stack, kindly provided by SOITEC. After substrate removal, shallow ridges are patterned by e-beam lithography using an HSQ resist and then etched by an ICP $Cl_2$-$H_2$ process, through all the InP membrane and down 60 nm in the Si guiding layer. Fig.1-(a) shows a cleaved-facet SEM picture of an oxide-free bonded hybrid waveguide. In order to protect the waveguides during cleaving, a thin resist layer is coated over the surface. The calculated TE mode intensity is shown on Fig.1-(b) evidencing the large overlap of the interface by the mode.

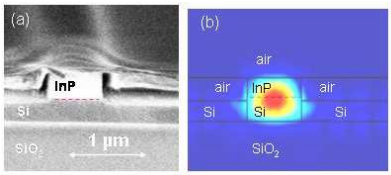



**Fig. 1: (a) SEM picture of a hybrid waveguide cleaved facet; (b) TE modal intensity (same scale)**

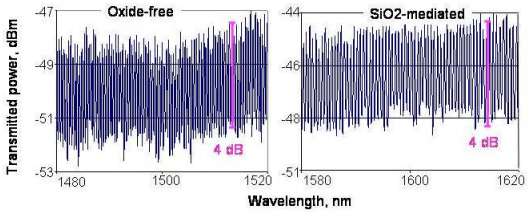



**Fig. 2: Transmission measurement showing a 4 dB fringe contrast for *left*-oxide-free hybrid waveguide and *right*-SiO2-mediated bonded hybrid waveguide**

Waveguides with two cleaved facets have been measured on an end-fire set-up including polarization-maintaining tuneable sources and injection fibre for TE polarization. Collection is performed with a microscope objective allowing simultaneous observation of the guided mode and collection in the fibre.

Propagation losses are calculated based on the fringe contrast. A 0.48 µm-wide oxide-free hybrid waveguide transmission shows a 4 dB contrast (Fig.2-*left*), as well as the ALD-mediated 0.5 µm-wide hybrid waveguide transmission (Fig.2-*right*), both waveguides being 650 µm long. This 4 dB fringe contrast, assuming a facet reflectivity r= 0.56, corresponds to propagation losses $\alpha$=5.0 $cm^{-1}$, which is also very close to the value for similar InP monolithic ridges waveguides etched with the same ICP process.

Neither of the two bonding processes contributes to extra optical losses on the optical mode sensing the hybrid interface during its propagation. The oxide-mediated bonding being already well qualified as not impacting propagation losses [7-8], we thus demonstrate here that oxide-free bonded interface reaches the same high optical quality.

**Conclusion:** The oxide-free hybrid interface has already shown to be crystallographic defect-free; we demonstrate here that it is optical-defect-free. This hybrid interface has the potential for electrical injection through the interface, thus allowing to fully performing the 3D optical-electrical integration.

References

[1] A. Talneau et al., Appl. Phys. Lett., **102**, 212101 (2013)
[2] K. Tanabe, K. Watanabe and Y. Arakawa, Sci. Rep., **2**:349 (2012)
[3] K. Pantzas et al., IPRM 2014, Montpellier, May 2014
[4] K. Bougot-Robin et al., Optics Express **22**(19), 23333-23338 (2014)
[5] A. Talneau et al., Optics Letters, **40** (22), 5148 (2015)
[6] A.Talneau et al., MNE , La Haye 2015
[7] A. Spott et al. , Optics Letters, **40** (7), 1480, (2015)
[8] G.-H. Duan et al., Invited paper, IEEE. J. Sel. Top. Quantum Electron., to appear in 2016

ECIO 2016
18TH EUROPEAN CONFERENCE ON INTEGRATED OPTICS 2016
18–20 MAY | WARSAW | POLAND

# CMOS-compatible low-loss silicon nitride waveguide integration platform for interferometric sensing

**Paul MUELLNER[1*], Alejandro MAESE-NOVO[1], Eva MELNIK[1], Rainer HAINBERGER[1], Guenther KOPPITSCH[2], Jochen KRAFT[2], Gerald MEINHARDT[2]**
[1]AIT Austrian Institute of Technology GmbH, 1220, Vienna, Austria
[2]ams AG, Unterpremstätten, 8141, Austria
[*] paul.muellner@ait.ac.at

During the past fifteen years, the major driving force for extensive research in the field of silicon photonic integrated circuits has been the continuously increasing data traffic to be transmitted over optical fiber links. The focus has therefore been on silicon-on-insulator (SOI) based optical waveguide technology, which cannot be applied for shorter wavelengths in the visible and near infrared region at wavelength smaller than 1.1µm. However, the <1.1µm wavelength region is most relevant for life sciences and health related applications such as evanescent biosensing and novel medical imaging diagnostic applications, which gained significant importance in recent years. Many of these applications are based on interferometric sensing principles.

In order to overcome the drawbacks of SOI, we present a silicon nitride waveguide based photonic integration platform realized by means of a low temperature plasma enhanced chemical vapour deposition (PECVD) process for the silicon nitride waveguide layer and the top & bottom silicon dioxide ($SiO_2$) cladding layers. Such an approach has already been pursued successfully in the past [1, 2]. However, in contrast to preceding works, we aim at the monolithic integration of the waveguides on top of a CMOS optoelectronic chip comprising photodiodes with which the light propagating in the waveguides can be directly detected. A main challenge in this context is the planarity of the lower buffer oxide covering the uneven surface of the optoelectronic chip. To this end, a process is required that provides a sufficiently planar surface for the waveguides.

A first task was the development of a low-loss silicon nitride waveguide fabrication process on bare silicon wafers without integrated photodiodes. For this purpose, we compared the losses of waveguides with different thicknesses measured for TE and TM polarization at a wavelength of 850 nm. From these results we were able to determine the main sources of the losses. About 90% of the losses can be attributed to absorption and scattering in the silicon nitride waveguide core. Only ~10% of the 1.5 dB/cm (see blue line in Fig. 1a) losses for a waveguide cross-section of 600x250 $nm^2$ are caused by other loss mechanisms such as roughness at the dry etched sidewalls or scattering in the $SiO_2$ cladding. This proves the high quality of the etching process. The observed propagation loss of 1.5dB/cm is slightly higher than in our previous demonstration [3]. This can be attributed to the fact that $SiO_2$ was used as top cladding instead of photoresist SU-8 in our former experiments. Since the refractive index of $SiO_2$ (n=1.46) is lower than that of SU-8 the light is more strongly confined in the waveguide core, which gives rise to loss.

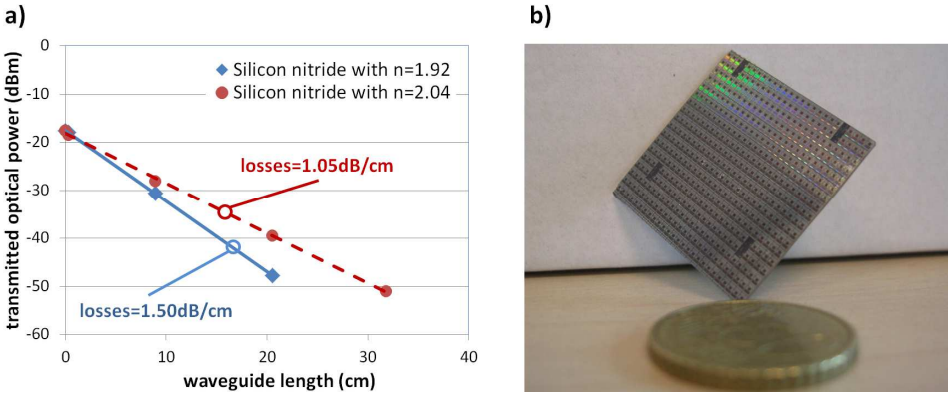



**Fig. 22. a) Transmitted optical power for different waveguide lengths and two different types of silicon nitride. From the slope a loss value of 1.5 dB/cm can be calculated for the silicon nitride with a refractive index n=1.92 (blue line) and 1.05 dB/cm for the silicon nitride with n=2.04. b) Optoelectronic chip with several hundreds of integrated photodiodes. In the foreground a 50 € cent coin is shown for the sake of size comparison.**

With an optimization of the deposition process of the silicon nitride waveguide layer we were able to significantly reduce these losses. The red dashed line in Fig. 1a) is the result of loss measurements for a silicon nitride waveguide layer with a refractive index of 2.04. The measured loss value of 1.05 dB/cm corresponds to a decrease of the losses by 30%. Eigenmode simulations suggest that for a waveguide cross-section of 160x800nm$^2$, which represents an optimized geometry for interferometric sensing applications, losses as low as 0.4 dB/cm can be achieved.

In a second step, the waveguide layer stack was fabricated on top of a wafer tightly packed with integrated photodiodes (see Fig. 1b). After adapting a chemical mechanical planarization process, the same low propagation loss was measured as on the samples without integrated photodiodes.

It has to be pointed out that all fabrication steps were performed in a commercial CMOS foundry environment. The results of this study open up the path for interferometric measurements employing optical waveguides monolithically co-integrated with silicon photodiodes.

References

[1] A. Gorin et al., *Fabrication of silicon nitride waveguides for visible-light using PECVD: a study of the effect of plasma frequency on optical properties,* Optics Express, Vol. 16, No. 18, pp. 13509–13516, 2008.

[2] A. Z. Subramanian et al., *Low-Loss single mode PECVD silicon nitride photonic wire waveguides for 532–900 nm wavelength window fabricated within a CMOS pilot line*, IEEE Photonics Journal, Vol. 5, No. 6, pp. 2202809, 2013.

[3] P. Muellner et al., *CMOS-compatible $Si_3N_4$ waveguides for optical biosensing,* Procedia Engineering, Vol. 120, pp. 578-581, 2015.

ECIO 2016
18TH EUROPEAN CONFERENCE ON INTEGRATED OPTICS 2016
18–20 MAY | WARSAW | POLAND

# Euler bends and TIR mirrors for ultra-dense PIC integration on SOI

**Timo AALTO[1*], Mikko HARJANNE[1], Matteo CHERCHI[1], Sami YLINEN[1]**
[1]VTT Technical Research Centre of Finland, Tietotie 3, Espoo, 02044, Finland
* timo.aalto@vtt.fi

Photonic integrated circuits (PICs) can be realized on multiple technology platforms that all have their own strengths and limitations. In this paper we describe some of the latest results in the ultra-dense integration of PICs using 3 µm thick silicon-on-insulator (SOI) waveguides. In particular we describe the design, fabrication and testing of Euler bends and total internal reflection (TIR) mirrors that both allow to turn light e.g. 90° with an effective bending radius of a few micrometers and ~0.1 dB/90° or smaller loss. For the Euler bends we also introduce a concept that allows designers to draw bends without the need to perform numerical simulations for each bend angle, wavelength and polarization that they want to use in the PIC.

Figure 1 illustrates an Euler bend and the new concept to design it. The bend is realized in a multi-moded (MM) strip waveguide that is adiabatically coupled to singe mode (SM) rib waveguides [1] using rib-strip converters. This way the PIC can be single-moded even if some parts are multi-moded. In 3 µm thick SOI waveguides the light is extremely well confined into the Si core, which eliminates radiation losses in the bend and enables down to 1 µm bending radius with <0.1 dB/90° loss [2]. Figure 1 shows the simulated transmission of TE-polarized light through the Euler bend at 1550 nm wavelength as a function of bend angle and minimum radius. The red line and the two dots show a fitted curve that represents bends that have high transmission and low transmission ripple. One should note that the colour scale is from 99.5% (black) to 100% (white) transmission, so that the ripple around the curve is very small. By using the analytical formula of the curve one can design a bend with arbitrary angle without numerical simulations. Different curves can be defined for different polarizations and wavelengths, although the same design typically works well for both polarizations over a very wide wavelength range.

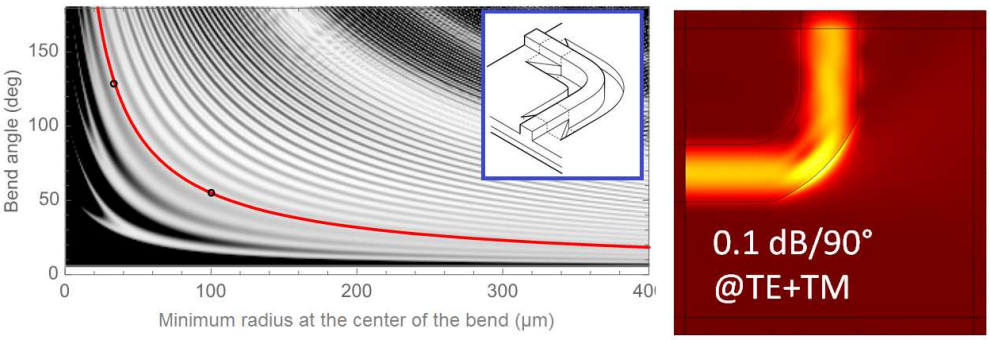
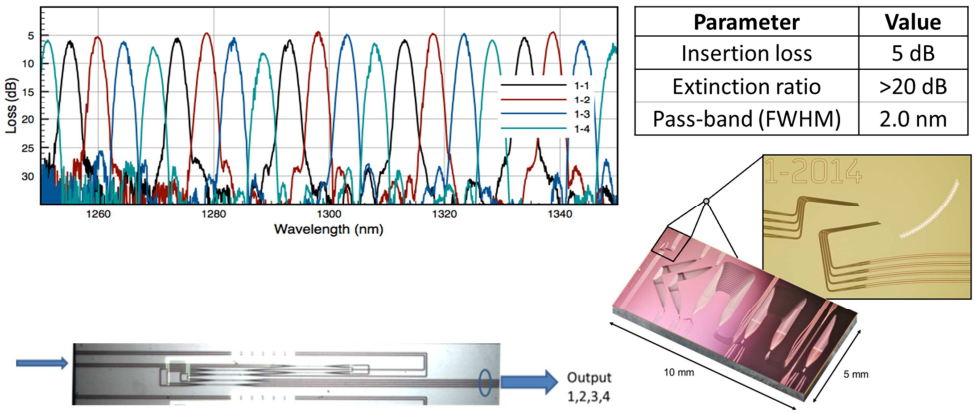



**Fig. 23. Left: Simulated light transmission in an Euler bend (schematic in inset). Right: Simulation of a TIR mirror with curved facet (loss result is experimental).**

Figure 1 also shows the simulation result for a TIR mirror that has a curved facet. The experimentally measured loss for such a TIR mirror in a strip waveguide is 0.1 dB/90° at both polarizations. Conventional TIR mirrors with straight facet have approximately 0.3 dB/90° loss. The advantage of the TIR mirrors is that they can be integrated directly into SM rib waveguides. However, the Euler bends are a natural choice when strip waveguides are anyway needed to realize e.g. ultra-small multi-mode-interference (MMI) couplers that require very high confinement between the input/output waveguides. The Euler bends can also be used to turn light by an arbitrary angle, unlike the TIR mirrors.

Despite the micron-scale core dimensions the 3 µm SOI waveguides also support the realization of many other densely integrated components, such as arrayed waveguide gratings (AWGs), Echelle gratings and asymmetric Mach-Zehnder interferometers (AMZIs). Examples of such devices have been illustrated in Fig. 2. The benefits of the large core dimensions also include low propagation loss (~0.1 dB/cm), small polarization dependency (dual polarization operation, even for DWDM), tolerance to high optical power and insensitivity to small fabrication errors.




| Parameter | Value |
|---|---|
| Insertion loss | 5 dB |
| Extinction ratio | >20 dB |
| Pass-band (FWHM) | 2.0 nm |

**Fig. 2. Bottom right: 3 µm SOI chip with various wavelength multiplexers having 50 GHz (DWDM) to 5 nm (CWDM) channel spacing. The Echelle grating is magnified. Top: Transmission spectra from four AWG outputs with 5 nm channel spacing and tabulated performance. Bottom: Cascaded AMZIs for compact and low-loss multiplexing (here 1x4).**

References

[1] R. A. Soref, J. Schmidtchen, and K. Petermann, "Large single-mode rib wave-guides in GeSi-Si and Si-on-SiO2," IEEE J. Quantum Elect., vol 27, pp. 1971–1974, 1991

[2] M. Cherchi, S. Ylinen, M. Harjanne, M. Kapulainen, and T. Aalto, "Dramatic size reduction of waveguide bends on a micron-scale silicon photonic platform," Optics Express, vol 21, pp. 17814-17823, 2013

ECIO 2016
18TH EUROPEAN CONFERENCE ON INTEGRATED OPTICS 2016
18–20 MAY | WARSAW | POLAND

# Buried heterostructures for deep UV lithography

**Valeria RUSTICHELLI[1,2*], Huub H.P.P.M. AMBROSIUS[1], René van VELDHOVEN[1], Romain BRENOT[2], Frederic POMMEREAU[2], Kevin WILLIAMS[1]**

[1]COBRA Institute, Eindhoven University of Technology, NL 5600 MB Eindhoven, the Netherlands
[2] III-V Lab, Route de Nozay, 91460 Marcoussis, France
[*] v.rustichelli@tue.nl

Buried Heterostructure (BH) lasers and amplifiers are known to have good thermal performance and efficient current injection [1-2]. However they have not so far been integrated with ridge waveguide devices, preventing complex circuit integration. The inclusion of BH waveguide in photonic circuits requires their integration with deep and shallow waveguides and this has been challenging to achieve because the active and passive waveguides are defined in different mask layers. The waveguides may be connected using either precision tapers [3] and or precision mask alignment at the 100 nm scale.

Among all the lithography techniques, which enables wafer scale production, deep UV (DUV) scanner lithography allows for high resolution and high precision alignment (100 nm). Therefore, in this work we propose the use of DUV scanner for the integration of BH and passive structures on the same circuit, and develop the processing steps required to minimize wafer flatness within the accepted field of focus.

In a DUV scanner, the pattern is projected on the substrate through a lens system, which reduces (four times) the pattern present on the mask. The used wavelength is short (195 nm) so the depth of focus is low and it requires a total thickness variation (TTV) of 1 µm and a local focal point variation (LFPV) of 200 nm: therefore, it is necessary that the exposed wafer present a flat surface during the exposure to ensure the wanted resolution all over the wafer. In a BH laser or amplifier the mesa is first defined by etching and later on is buried by the InP regrowth. The hard mask is removed after the InP regrowth and the passive integration can be carried on by DUV lithography. Then the COBRA generic integration process can be implemented to complete circuit fabrication [4].

Figure 1 shows a SEM picture of the cross section of a BH before (1-a) and after (1-b) regrowth.

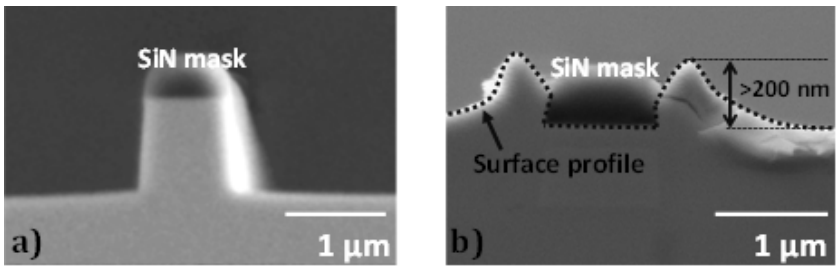



**Fig. 3. SEM cross section of the mesa after dry etching and after InP regrowth (b); the overgrown material at the edge of the stripe doesn't allow for the use of DUV.**

The mesa were oriented in the [0$\bar{1}$1] direction and were defined by ICP with a $CH_4/H_2$ chemistry and SiN as hard mask. The successive InP regrowth was performed by MOVPE. The resulting topography shows an anomalous growth in the vicinity of the mask. These overgrowth defects have thickness of 500 nm meaning that the surface profile does not meet the DUV requirements mentioned above. As demonstrated in [5-6], to improve the wafer flatness for planar BH, one solution is to create, by wet etching, an overhang under the hard mask. The purpose is to prevent the InP under the overhang to grow upward.

Figure 2-a shows a SEM picture of the cross section of a mesa defined by wet etching: the created overhang (dotted line) is about 250 nm. In the sample, the mesa was created using diluted hydrochloric acid (25 %) for 1 min to etch the InP layer and citric acid to etch the quaternary active layer. The measured overhang is around 250 nm for the optimized process flow. After the definition of the mesa, the InP regrowth was performed (see Fig 2-b) by MOVPE with the same parameters as before. It is clear that, thanks to the overhang, the resulting surface profile is almost flat. Therefore, after removing the SiN mask, it is possible to use DUV.

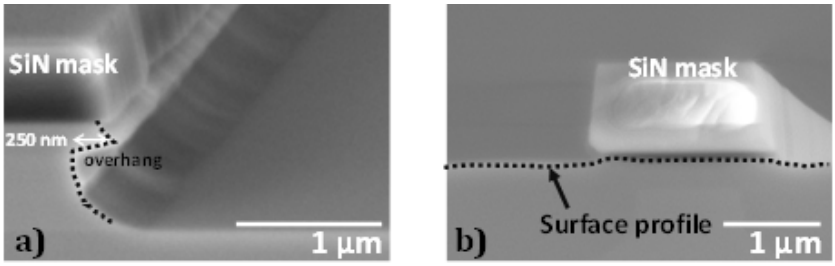



**Fig. 4. SEM cross section of the mesa after wet with creation of the overhang (b) mesa after the regrowth: the surface profile is now compatible with DUV scanner.**

In this work we have demonstrated a first step towards the integration of BH lasers and amplifiers with passive components. The critical steps involved in the fabrication of BH components have been shown to be compatible with the use of DUV lithography. The use of DUV lithography will enable to align with high accuracy active and passive components.

References

[1] N. Iwai et al. *High Power AlGaInAs /InP widely wavelength tunable laser*, Optical Comunication, special issue 2015.
[2] F. Trager, *Springer Handbook of Lasers and Optics*, Springer New York, 2007
[3] V.Rustichelli et al. *Technology development and implementation of a transmitter in generic technology using Buried Heterostructure Semiconductor Amplifiers*, in Proceeding of the 20th Annual Symposium, pp 43-44, 2016.
[4] M.Smit et al. *An introduction to InP-based generic integration technology*, Semiconductor Science and Technology., vol.29, no.8, 2014
[5] L.Cheng et al, *Analysis of InP regrowth on deep-etched mesas and structural characterization for Buried-Heterostructure quantum cascade lasers*, Journal of Electronic Materials, Vol. 41, No. 3, 2012
[6] K.Nakai, *Planar selective growth of InP by MOVPE*, Journal of Chrystal Growth, Vol. 93, 1998

ECIO 2016
18TH EUROPEAN CONFERENCE ON INTEGRATED OPTICS 2016
18–20 MAY | WARSAW | POLAND

# Double-sided processing for membrane-based photonic integration

**Longfei SHEN[1*], Yuqing JIAO[1], Aura HIGUERA-RODRIGUEZ[1], Alonso MILLAN-MEJIA[1], Gunther ROELKENS[1,2], Meint SMIT[1], Jos van der TOL[1]**
[1] Photonic Integration Group, Eindhoven University of Technology, Eindhoven, The Netherlands
[2] Photonics Research Group, Ghent University-IMEC, Ghent, Belgium
[*] l.shen@tue.nl

*Abstract:* double-sided processing, as a fabrication technology dedicated for membrane photonics, gives rise to new design optimizations. This paper reports latest achievements of this processing scheme in an InP-membrane-on-silicon (IMOS) platform, with a focus on a high bandwidth (>67 GHz) photodetector. Furthermore, a novel integration platform based on the double-sided processing is proposed, to integrate high-performance building blocks in a single membrane layer, providing full photonic functionality.

Membrane photonics presents a promising platform technology for the realization of photonic integrated circuits (PICs) on silicon [1, 2]. High-performance devices covering full functionality need to be developed on this platform. Double-sided processing technology enables a new degree of freedom in device optimization, by designing and fabricating membrane structures from both sides. It is uniquely suitable for the IMOS platform, in which InP membranes can be processed both before and after bonding to a silicon wafer using BCB [1]. As the light only propagates in the InP membrane where all photonic components are located, critical alignment to the silicon wafer during the bonding is not necessary, which assures the practicality of this technology. Also, thanks to the use of BCB, high yield in bonding with processed samples can be achieved.

In the IMOS platform, a high speed uni-traveling carrier photodetector (UTC-PD) is developed. It uses double-sided processing to define p- and n- contacts on opposite sides of the membrane (Fig. 1), leading to a significant reduction of the resistance on the p-side. Since the p-InGaAs absorber in UTC-PDs is usually doped with a gradient, p-contact depositing on the highly doped surface on the bottom of the p-InGaAs layer results in low contact resistance. Moreover, p-contacts defined at the lower side of the mesa can be placed very close to the optical mode, which is crucial for avoiding the excessive series resistance from the thin p-InGaAs layer. Consequently, this results in a very low RC-time constant and a very high 3 dB bandwidth beyond 67 GHz, which is the highest value reported for membrane PDs on silicon so far.

An efficient metal grating coupler is another demonstrated device using the double-sided processing [3]. By depositing silver-based low-loss metal mirrors at the bottom side of the membrane, the grating shows reduced leakage of light to the silicon substrate, resulting in a high coupling efficiency of 54%. Furthermore, the efficiency is independent of the BCB layer thickness. This solves a fundamental problem of membrane photonic circuits: as the BCB layer thickness is not uniform over the wafer, interference between the waves reflected at two interfaces (InP/BCB and BCB/Si) can cause unpredictable variations in coupling efficiency.

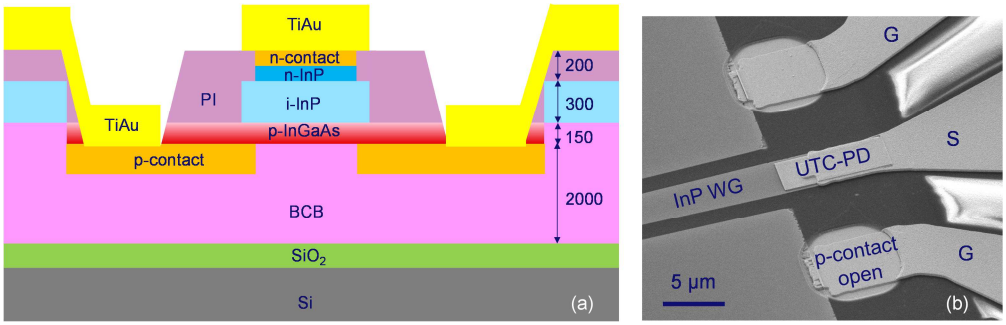



**Fig. 28. (a) Cross-section of the UTC-PD. Thickness in nm. (b) SEM photo of the device.**

Finally, double-sided processing provides a potential technology to integrate components with different layer-stacks without using multiple regrowth steps. As proposed in Fig. 2, demonstrated devices and existing designs can be integrated monolithically as building blocks on this new platform. These include low-loss waveguides [1], electrically-pumped lasers [2], metal gratings [3], slot-waveguide modulators [4], and high speed UTC-PDs. A remarkable advantage of this integration platform is the optimal material choice for each component. In particular, quantum-wells (QWs) give high efficiency and low threshold for lasers, but they are not efficient as the absorption material in PDs. On the other hand, UTC structures provide high bandwidth and high saturation power to PDs, but they are not compatible with laser structures. To avoid trade-offs on material choices, QW-based lasers and InGaAs-based UTC-PDs can be integrated using the double-sided processing.

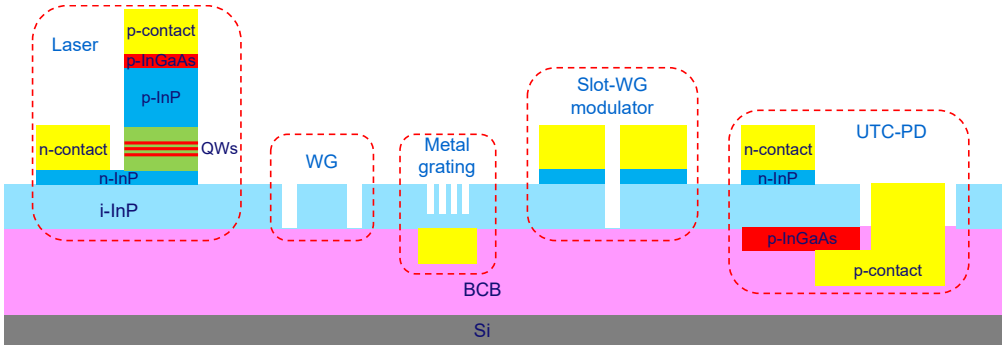



**Fig. 29. A new integration platform based on double-sided processing.**

In conclusion, double-sided processing promises high performance membrane devices by offering more freedom in design optimization. It is also a potential technology for platform integration of advanced components which are very difficult to integrate using traditional techniques.

References

[1] J. van der Tol *et al.,* Proc. SPIE 8988, 89880M, 2014
[2] Y. Jiao, *et al.,* in Proceedings of the Advanced Photonics Conference, p. IM4B.3, 2015
[3] A. Higuera-Rodriguez *et al.,* Optics Letters, vol. 40, no. 12, pp. 2755-2757, 2015
[4] A. Millan-Mejia *et al.,* in Proceedings of the 20th Annual Symposium of the Benelux IEEE Photonics Society, p. 1.01, 2015

ECIO 2016
18TH EUROPEAN CONFERENCE ON INTEGRATED OPTICS 2016
18–20 MAY | WARSAW | POLAND

# Fast and Energy Efficient Micro-Ring-Resonator-Based 4×4 InP Switch Matrix

**Ripalta STABILE*, Prometheus DASMAHAPATRA, Kevin A. WILLIAMS**
Eindhoven University of Technology, COBRA research institute, P.O. Box 513, 5600 MB Eindhoven, The Netherlands
*r.stabile@tue.nl

Wavelength-selective micro-ring resonators combined with electro-optic tuneable elements can provide fast switching functionalities. Most of the research done so far on active micro-ring resonators has however focused on the realization of first-order micro-ring resonator based devices such as filters and lasers [1-2] or on monolithically integrated switches on Silicon on Insulator (SOI) platform [3]. However, the inherent trade-off between the achievable bandwidth and the signal extinction in first-order micro-rings [4] have limited their use in switching. Moreover, nanoscale feature size variations lead to a shift of the peak wavelength of the same order [4] which particularly complicates applications in large scale circuits.

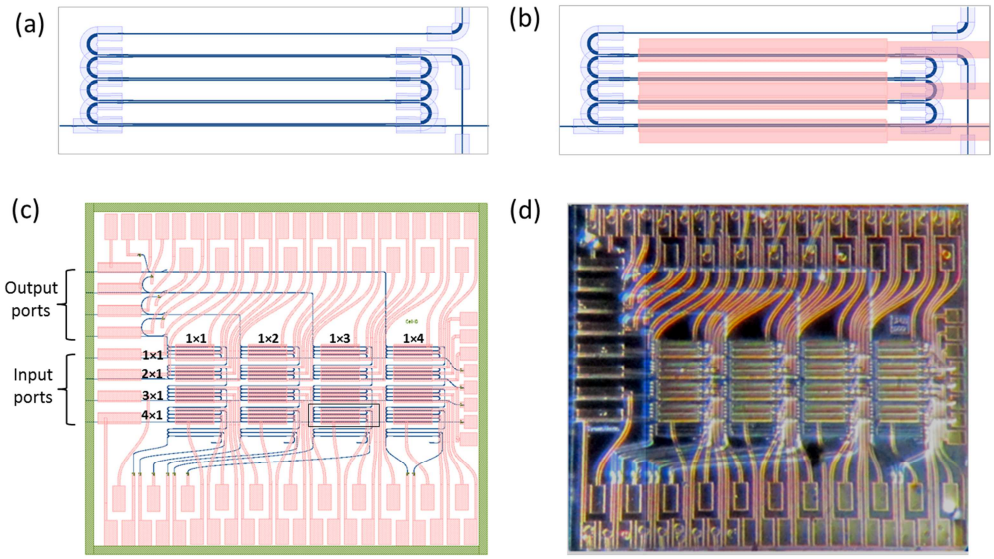



**Fig. 32. (a) Single switching element composed of three race-track micro-rings. (b) Electrodes (in red) place on the top of directional coupler for fine tuning. (c) Full layout of the chip, including the optical wiring layer (in black) and the metal wiring (in red). (d) Photograph of the fabricated chip.**

Higher-order resonator have been shown to decouple the trade-off between the bandwidth and the signal extinction so that both data bandwidth and switch speed parameters can be optimised together [5-6] This also enables an enhanced bandwidth of such devices and improves tolerance to variations in fabrication [4]. The possibility of achieving faster switching times and low power consumption makes III-V material platform very attractive for photonic integrated circuits based on ring resonators.

In this work, for the first time a 4×4 switch matrix based on higher-order resonant elements is designed and fabricated in the InP material platform. Third-order ring resonators (Fig. 1a) are designed and placed in a cross-point matrix. Fast electro-optic

tuning is used to allow data to drop to the next port or pass through. Three electrodes per element are provided to allow the reciprocal tuning of each element (Fig. 1b). The full mask layout and a photograph of the realized chip are shown in Fig. 1c and d.

10Gbps data routing is performed across a combination of 4 different paths in the circuit. Furthermore, a representative path is used to demonstrate higher, passband-limited line-rate of 20Gbps (see Fig. 2a). A maximum power penalty of 2.6 dB is recorded. The on-state electrical power consumption is only 79 μW, which leads to an energy consumption of 8 fJ/s for 10 Gb/s operation. Fast switching of a few nanoseconds for the rise and the falling time is measured as shown in Fig. 2b.

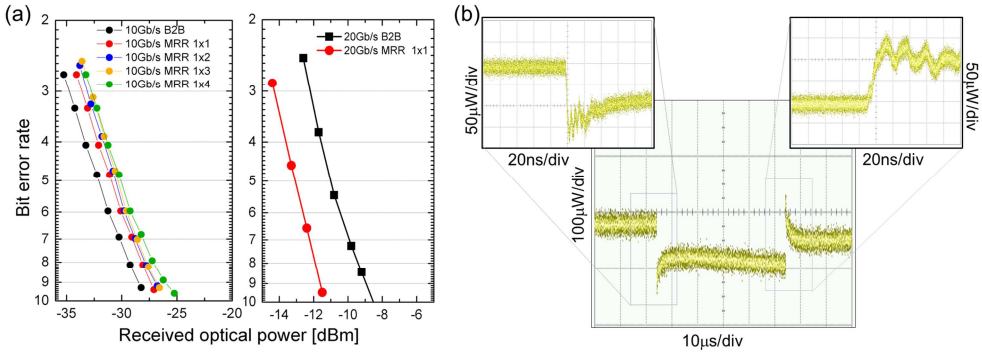



**Fig. 33. (a) Bit error rate for 10 and 20 Gbps line rates. (b) Time traces for switching time: falling time in the left-hand side inset and rising time in the right-hand side inset.**

**Acknowledgement:** The devices reported in this work were fabricated by Smart Photonics through the JePPIX.eu MPW service.

References

[1] M. T. Hill, H. J. S. Dorren, T. de Vries, X. J. M. Leijtens, J. H. den Besten, B. Smalbrugge, Y. S. Oei, H. Binsma, G. D. Khoe and M. K. Smit, “A fast low-power optical memory based on coupled micro-ring lasers”, Nature 432, 206-209 (2004).

[2] G. Griffel, J. H. Abeles, R. J. Menna, A. M. Braun, J. C. Connolly and M. King, "Low-threshold InGaAsP ring lasers fabricated using bi-level dry etching," Photon. Tech. Lett., IEEE, vol.12, no.2, pp.146,148, (2000).

[3] P. DasMahapatra, R. Stabile and K.A. Williams, “”, JSTQE 2014

[4] K. Williams, A. Rohit, and M. Glick, "Resilience in optical ring-resonant switches," Opt. Express 19, 17232-17243 (2011).

[5] D. G. Rabus, M. Hamacher, U. Troppenz and H. Heidrich, "Optical filters based on ring resonators with integrated semiconductor optical amplifiers in GaInAsP-InP," Selected Topics in Quantum Electronics, IEEE Journal of, vol.8, no.6, pp.1405,1411, (2002).

[6] H. Ikehara, T. Goto, H. Kamiya, T. Arakawa, and Y. Kokubun, "Hitless wavelength-selective switch based on quantum well second-order series-coupled microring resonators," Opt. Express, 21, 6377-6390 (2013).

ECIO 2016
18TH EUROPEAN CONFERENCE ON INTEGRATED OPTICS 2016
18–20 MAY | WARSAW | POLAND

# A New Approach to Designing Polarization Rotating Waveguides

**Moritz BAIER*, Francisco M. SOARES, Martin MOEHRLE, Norbert GROTE and Martin SCHELL**
Fraunhofer HHI, Einsteinufer 37, Berlin, 10587, Germany
* moritz.baier@hhi.fraunhofer.de

Implementation of polarization rotating building blocks for photonic integrated circuits remains a challenge. To achieve polarization extinction ratios (PER) above 20 dB in indium phosphide (InP) based waveguides, fabrication tolerances with respect to the waveguide width of around 100 nm or less are required with previous designs [1]. In this work, we present a way of allowing for a respective tolerance of more than 200 nm which substantially eases fabrication using common optical lithography techniques. The design is again based on a slanted sidewall waveguide but a key feature of it is that it does not rely on the waveguide modes being angled by 45° as is commonly required with devices reported recently [1]–[3].

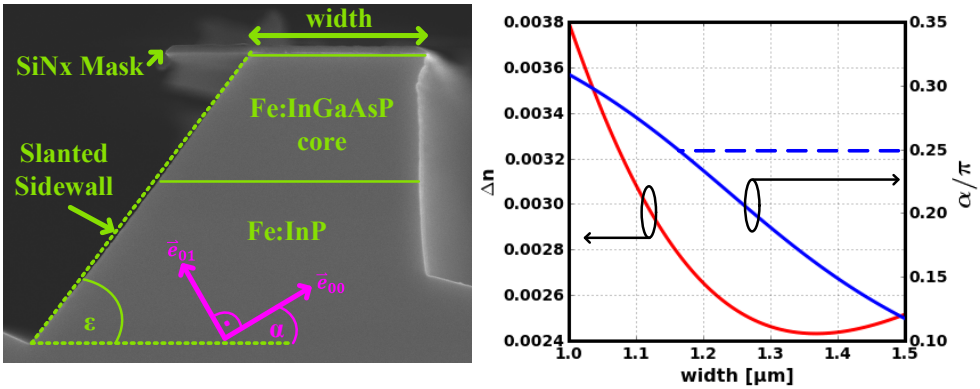



**Fig. 7. Left: Cross-section of the slanted sidewall waveguide in this work. The InGaAsP guiding layer has a photoluminescence peak of 1.06 µm. The drawing indicates the tilt α of the modal basis. The slant angle ε is 52° in this work. The waveguide width is defined at the top. Right: Birefringence (red) and modal tilt (blue) versus waveguide width. The slope of these curves becomes smaller for $\alpha < \pi/4$, making larger widths significantly more favorable in terms of tolerance.**

A slanted sidewall waveguide generally supports a modal basis that is tilted by an angle α with respect to the substrate's plane (see fig. 7). The two modes generally exhibit a birefringence $\Delta n$. The Jones matrix of such a waveguide with physical length L and normalized length $\delta = \Delta n L/\lambda$ is given by

$$\underline{J} = \begin{bmatrix} e^{i\pi\delta}sin^2(\alpha) + e^{-i\pi\delta}cos^2(\alpha) & \frac{1}{2}(1-e^{2i\pi\delta})e^{-i\pi\delta}\sin(2\alpha) \\ \frac{1}{2}(1-e^{2i\pi\delta})e^{-i\pi\delta}\sin(2\alpha) & e^{i\pi\delta}cos^2(\alpha) + e^{-i\pi\delta}sin^2(\alpha) \end{bmatrix} \quad (1)$$

The Jones matrix of a series of such waveguides is given by the respective matrix product. In this paper, we limit ourselves to a two-section device, represented by a product of two matrices $\underline{J}_1$ and $\underline{J}_2$. For perfect rotation, the main diagonal of the resulting matrix must vanish while the anti-diagonal must be unity. A simple solution

can be found when setting $\alpha_1 = -\alpha_2 = \pi/4$. One then finds $\delta_1 = 0.25$ and $\delta_2 = 0.75$. There are, however, other solutions for various other angles that cannot be found analytically.

Using a FDE mode solver, we derived the dependence of $\alpha$ and $\Delta n$ on the waveguide width $w$. The result is shown in fig. 7. It can be seen that the slope of $\Delta n$ and hence the tolerance is particularly crictical for widths where $\alpha \geq \pi/4$. The slope decreases at larger widths, i.e. smaller $\alpha$. Using those $\alpha(w)$ and $\delta(w)$ as well as eq. (1), one can compute the Jones matrix of any arbirtrary 2-(or more) section device. It should be noted that once $\alpha(w)$ and $\delta(w)$ are known, computing the Jones matrix only takes milliseconds or less. This makes optimization algorithms readily applicable even if they have to evaluate thousands of devices.

Fig. 8 shows maps of the PER for a two-section device in the space of the respective waveguide width of either section, $w_1$ and $w_2$.

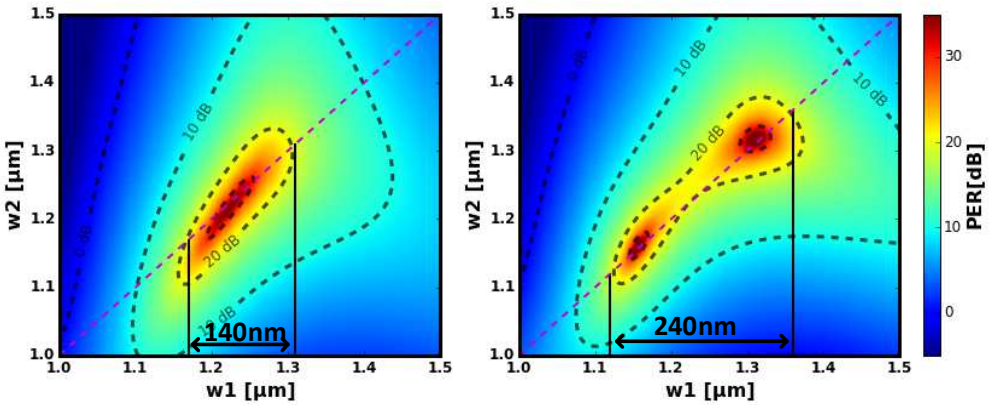



**Fig. 8. PER maps versus waveguide widths of a 2-section device. Left: PER map of a device with $\alpha_1 = -\alpha_2 = \pi/4$ and $\delta_1 = 0.25, \delta_2 = 0.75$. Right: PER map for a device with $\alpha_1 = -\alpha_2 = 0.21\pi$ and $\delta_1 = 0.29, \delta_2 = 0.74$. These parameters are obtained from numerical optimization of the Jones matrix' tolerance. The tolerance of either waveguide width is increased from 140 nm to 240 nm. To obtain those numbers, it is assumed that a deviation in width will be equal over both sections (indicated by dashed magenta line).**

In summary we have shown a method of designing an integrated polarization rotator which does not rely on the common condition $\alpha = \pi/4$ and therefore enables 100 nm of additional tolerance.

References

[1] D. O. Dzibrou, J. J. G. M. Van Der Tol, and M. K. Smit, "Extremely efficient two-section polarization converter for InGaAsP-InP photonic integrated circuits," in *Lasers and Electro-Optics Europe (CLEO EUROPE/IQEC), 2013 Conference on and International Quantum Electronics Conference*, 2013, pp. 1–1.
[2] H. Deng, D. O. Yevick, C. Brooks, and P. E. Jessop, "Design rules for slanted-angle polarization rotators," *J. Light. Technol.*, vol. 23, no. 1, pp. 432–445, Jan. 2005.
[3] H. El-Refaei, D. Yevick, and T. Jones, "Slanted-Rib Waveguide InGaAsP-InP Polarization Converters," *J. Light. Technol.*, vol. 22, no. 5, p. 1352, Mai 2004.

ECIO 2016
18TH EUROPEAN CONFERENCE ON INTEGRATED OPTICS 2016
18–20 MAY | WARSAW | POLAND

# COBRA long wavelength active-passive monolithic photonic integration technology platform

**S. Latkowski[1*], P.J. van Veldhoven[1], D. D'Agostino[1], H. Rabbani-Haghighi[1], B. Docter[3], P. Thijs[1], H. Ambrosius[1], K. Williams[1], E.A.J.M. Bente[1] and M. Smit[1]**
[1]COBRA Research Institute, Eindhoven University of Technology,
De Zaale, 5612 AJ, Eindhoven, The Netherlands
[2]EFFECT Photonics B.V., Torenallee 20, Eindhoven, The Netherlands
[*]S.Latkowski@tue.nl

Standardized, generic photonic integration technologies [1] enable low-cost design and prototyping of photonic integrated circuits (PIC) realizing complex functionalities for a particular application on a chip scale. The range of potential applications for such photonics integration technology platforms [1] is currently restricted by the accessible wavelengths bands. All of the currently available and mature technology platforms offer their functionalities at wavelengths at around 1.5 µm. This wavelength range corresponds to the c-band in the area of telecommunications and consequently the majority of the application specific photonic integrated circuits (ASPIC) being realized target this area [1]. In order to extend the reach to other fields of applications and broaden a potential market for such generic photonic integration technologies the range of accessible wavelengths has to be diversified [2], [3]. The mid-infrared range beyond 2µm is particularly attractive for gas sensing applications due to presence of strong absorption lines of many gas species for example: acetone, ammonia, carbon dioxide, water vapor, formaldehyde, diethylamine, ethylamine, methylamine and others. Development of a long-wavelength, monolithic, active-passive integration technology on indium phosphide (InP) substrate was undertaken at the COBRA Research Institute in order to extend the potential of the already existing technology at 1.5µm.

The COBRA active-passive generic integration scheme relies on a limited set of predefined functionalities which are provided in the form of building blocks (BB). These BBs are realized in one of two types (active or passive) of vertical layer-stack epitaxial cross-sections combined on a common substrate via butt-joint integration [1].

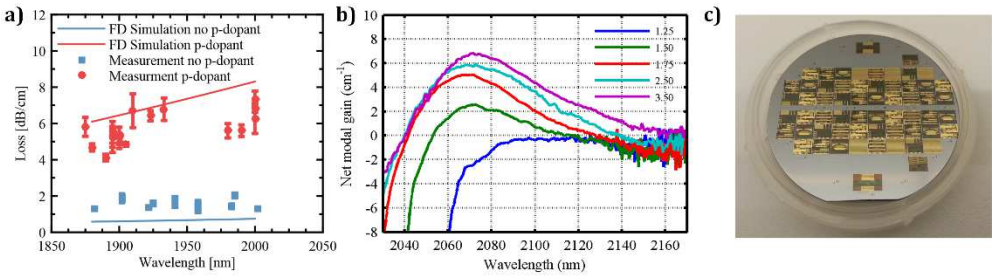



**Fig. 1 (a) Propagation losses in passive waveguides at long wavelengths. (b) Net modal-gain measured from semiconductor amplifier sections based on strained quantum wells and fabricated using non-optimized ridge waveguide geometry i.e. 500 nm thick and 2µm wide c) A photograph of the fabricated multi-project wafer (MPW) containing 8 different designs.**

These BBs can be combined into large complexity topologies to realize an application specific system on-chip or in other word an ASPIC. The development process of the

COBRA long-wavelength technology included modifications of the vertical cross-sections of the active and passive layer-stacks and adaptations of all BBs to realize all basic functionalities at longer wavelengths. The studies and early stage experiments have shown that at longer wavelengths an increase in the propagation loses and lower gain values shall be expected as presented in the Fig. 1(a) and Fig. 1(b) respectively. In order to reduce propagation losses due to overlap with highly doped cladding layers the thickness of the wave guiding layer was increased to 625 nm with further adjustment of the ridge wave-guide (RWG) structures in lateral direction. A new optically active core based on low temperature (560 °C) strained multi quantum wells (InGaAs) has been developed to realize the BBs which provide with on-chip means of light generation and an optical gain (semiconductor optical amplifiers) or absorption (photodiodes, saturable absorbers).

These research and development efforts have enabled fabrication of the first long-wavelength multi-project wafer (MPW) run. The wafer processing was carried using cleanroom facilities of Nanolabl@TU/e [4]. The 2" MPW wafer shown in Fig.1 (c) included 8 designs from 5 different users and projects, including two unique monolithically integrated tunable lasers with a large tuning range in the 2 mm wavelength window [5], [6].

**Acknowledgement**
The authors would like to acknowledge support for the presented work from the STW Technology Foundation project LWAVETECH, the IOP Photonic Devices project TULGAS and the EU FP7 Integrated Project Paradigm.

References

[1] M. Smit, et al. *An introduction to InP-based generic integration technology*, Semicond. Sci. Technol., vol. 29, no. 8, p. 083001, Jun. 2014.

[2] K. Scholle, S. Lamrini, and P. K. and P. Fuhrberg, *2 μm Laser Sources and Their Possible Applications,* Feb. 2010.

[3] G. Roelkens, U. Dave, A. Gassenq, N. Hattasan, C. Hu, B. Kuyken, F. Leo, A. Malik, M. Muneeb, E. Ryckeboer, D. Sanchez, S. Uvin, R. Wang, Z. Hens, R. Baets, Y. Shimura, F. Gencarelli, B. Vincent, R. Loo, J. Van Campenhout, L. Cerutti, J.-B. Rodriguez, E. Tournie, X. Chen, M. Nedeljkovic, G. Mashanovich, L. Shen, N. Healy, A. C. Peacock, X. Liu, R. Osgood, and W. M. J. Green, *Silicon-Based Photonic Integration Beyond the Telecommunication Wavelength Range,* IEEE J. Sel. Top. Quantum Electron., vol. 20, no. 4, pp. 394–404, Jul. 2014.

[4] *NanoLab@TU/e*. [Online], Available: http://www.tue.nl/en/research/research-institutes/research-institutes/nanolabtue/. [Accessed: 13-May-2015].

[5] D. D'Agostino, S. Tahvilli, L. Sylwester, P. J. Veldhoven, H. Rabbani-Haghighi, C. Jin, B. Docter, H. Ambrosius, E. Bente, D. Lenstra, and M. Smit, *Monolithically Integrated Widely Tunable Coupled Cavity Laser Source for Gas Sensing Applications around 2.0μm Wavelength*, Advanced Photonics 2015 (2015), paper JT5A.1, 2015, p. JT5A.1.

[6] S. Latkowski, D. D'Agostino, P. J. van Veldhoven, H. Rabbani-Haghighi, B. Docter, H. Ambrosius, M. Smit, K. Williams, and E. A. J. M. Bente, *Monolithically integrated tunable laser source operating at 2 μm for gas sensing applications*, in Photonics Conference (IPC), 2015, 2015, pp. 535–536.

ECIO 2016
18TH EUROPEAN CONFERENCE ON INTEGRATED OPTICS 2016
18–20 MAY | WARSAW | POLAND

# Low-Energy, Dilated 4x4 Hybrid MZI-SOA Cross-point Optical Switch

**M. DING, A. WONFOR, Q. CHENG, N. BAMIEDAKIS, R. V. PENTY, I. H. WHITE**
Centre for Photonic Systems, University of Cambridge, CB3 0FA, United Kingdom
Author e-mail address:md613@cam.ac.uk.

Optical switches are regarded as potential key enabling components for future communication routing systems to accommodate significantly increasing internet traffic in both data-centres and the core network [1]. Opto-electronic devices, such as semiconductor optical amplifiers (SOAs) and Mach-Zehnder Interferometers (MZIs), with nano-second response times have received much attention since they are able to fulfil the requirements of packet switching [2]. SOAs offer high ON/OFF extinction ratio and broadband operation. However, SOA-based switches are constructed using a broadcast-and-select architecture, where splitters/combiners introduce inherent loss. This loss is compensated for by the gain provided by SOAs, although this is accompanied by amplified spontaneous emission (ASE) noise and saturation-induced distortion. MZI-based switches avoid the inherent loss due to splitters/combiners but they suffer from poor crosstalk performance and exhibit insertion loss.

Therefore, we have proposed a novel hybrid MZI-SOA switch approach to utilise the advantages of both components [3]. As shown in Fig.1(a), the MZIs act as the switching elements and the SOAs are used to suppress the crosstalk signal in the OFF state and compensate the passive components' loss in the ON state. A 2×2 hybrid switch has been reported in [4], which shows 26 dB input power dynamic range (IPDR) for a power penalty of less than 0.5 dB. A rearrangeably nonblocking 4x4 hybrid switch can be built by connecting the modular 2x2 blocks in a dilated Beneš architecture [Fig. 1(b)].

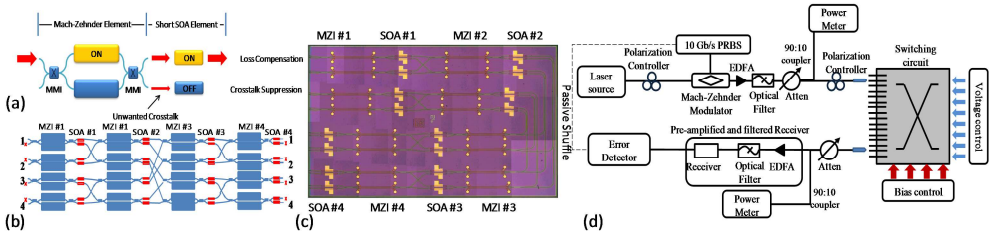



**Fig. 34. (a) Operating principle (b) Schematic of a 4x4 switch (c) Photograph of the fabricated 4x4 switch (d) the experimental test-bed.**

Fig. 1(c) shows the fabricated 4x4 switch chip produced within the EU FP7 PARADIGM project [5]. The chip is realised within a multi-project wafer run with generic basic building blocks based on the InGaAsP material system and has a size of 4 mm × 6 mm. The limited chip size requires the layout to be folded to fabricate all the elements as shown in Fig. 1(b). Each path on the switch contains four 1000/900 μm long MZIs and 230/250 μm long SOAs. The 250 μm long SOAs are used before the passive shuffle network in order to compensate for excess loss. The input and output facets of the chip are anti-reflection coated.

The static characteristics of the longest path are measured using the test-bed shown in Fig. 1(d). The switch is mounted on a thermo-electric cooler and maintained at 20 °C.

Lensed fibres are used to couple light into/out of the chip. The gain performance of the SOAs is characterised by determining their transparency current, which is found to be 3.7/4.2 mA for the 230/250 μm long SOAs respectively. The passive loss of the path can be measured when all SOAs are biased at transparency. The power budget of the longest path through the switch is shown in Fig. 2(a), with the components listed as follows: S-bends (S-Bs), multimode interference couplers (MMIs), phase modulators, semi-circular bends (SC-Bs). The 1000/900μm MZIs exhibit 2.2/2dB insertion loss respectively. 15/17 mA bias currents are chosen for the 230/250μm SOAs respectively to ensure lossless operation. The switch exhibits a peak gain at 1535 nm with a 3 dB bandwidth of 22.5 nm. The switch exhibits more than 100dB ON/OFF extinction ratio.

BER measurements are performed at a wavelength of 1535.89 nm. The optical input to the switch is generated by a tuneable laser that is modulated by a Mach-Zehnder modulator driven by a 10 Gb/s $2^{31}$-1 pattern length PRBS. The output is connected to an optically pre-amplified and filtered receiver and an error detector. Fig 2(b) shows the power penalty at a BER of $10^{-9}$ versus the on-chip input power. The 0.5 dB-penalty IPDR exceeds 15 dB. Each path consumes electrical power of 6 2mW and the energy consumption per bit is 6.2 pJ at a 10 Gb/s data rate, featuring a 42% lower energy consumption compared to equivalent 4x4 SOA switches [1].

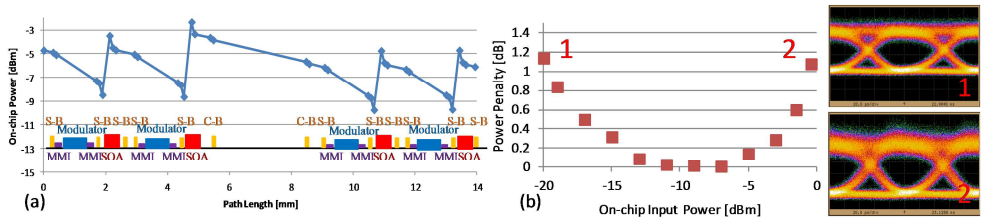



**Fig. 2. (a) Power budget for the longest path (b) IPDR curve with eye diagrams measured at -20 and 0dBm on chip input power.**

In conclusion, this paper presents the first integrated 4x4 hybrid MZI-SOA switch that offers lossless operation. The longest path exhibits more than 15dB IPDR for a penalty less than 0.5 dB.

**Acknowledgment**:
This research has received funding from EPSRC through the INTERNET Project and from the EU via the FP7 PARADIGM project. Additional data related to this publication is available at the Cambridge data repository: http://www.repository.cam.ac.uk/.

References

[1] A. Wonfor, et al, *J. Opt. Commun. Netw.*, vol. 3, p. A32, (2011).
[2] I. White, et al, *International Conference on Transparent Optical Networks,* 1–4 (2015)
[3] Q. Cheng, et.al*, J. Lightw. Technol.,* 18, pp. 3077- 3084, (2013).
[4] Q. Cheng, et.al, *European Conference on Integrated Optics*, paper Th 4b R2, (2014)
[5] M. Smit, et.al, *Semiconductor Science and Technology,* vol. 29, p. 083001, (2014).

ECIO 2016
18TH EUROPEAN CONFERENCE ON INTEGRATED OPTICS 2016
18–20 MAY | WARSAW | POLAND

# Design environment for active photonic integrated circuits improves the DML

**D. GALLAGHER, A. DABBS**
Photon Design, 34 Leopold St, Oxford, OX4 1TW, UK

We present an advanced design environment for the development and simulation of modern photonic integrated circuits (PICs) including active components. Several PIC design environments have been developed targeting passive PICs. But InP PICs in particular can include SOAs and diode lasers. There are many excellent tools available for modelling SOAs and diode lasers but cannot be readily extended to model PICs. The environment is used to design a novel efficiency-enhanced DML (direct modulated laser).

The design environment is capable of detailed modelling of an SOA for active components and a rigorous Maxwell Equation solver for passive components, with models for all the components brought together at circuit level using a travelling wave time domain model PicWave [1,2]. Note that all laser diode devices can be modelled as an SOA plus mirrors or one sort or another. Indeed the SOA can form part of a much larger active PIC.

Modelling of an SOA is divided into two parts. First the heterostructure is modelled in detail using Harold, originally developed by University of Madrid [3]. This implements a self-consistent drift-diffusion model with a parabolic-band gain model and produces a set of material functions: gain g(Nqw, lambda, T), where Nqw is a the quantum well electron density (assumed equal to hole density), carrier lifetime tau(Nqw,T) and a capture-escape model, so that Nqw can be computed for a given injection current. These material functions are then exported into a time-domain travelling wave simulator PicWave [refs], which is able to simulate quickly.

The SOA model, while being required to maintain fast execution, still includes many physical phenomena, including lateral current spreading, carrier diffusion, non-Lorentzian gain, and bulk-to-well capture dynamics. The latter is illustrated in Figure 1 and shows the importance of a multi-carrier model in getting the dynamics of a diode laser correct.

Recently Finisar proposed a method of improving the performance of a DML by adding a modulated SOA after it [4]. A DML can approach 2x the efficiency of a laser with external modulator, since when a “0” is transmitted the DML current is low. However to attain speed of a DML, the “0” state must not switch the laser completely off. Contrast can be regained by following it with a modulated SOA that is switched to low current during “0” bits, absorbing any residual power coming out the DML in “0” state.

A related approach can dramatically improve a DML/SOA setup even without gating (absorbing regime), eliminating the effect of saturation.

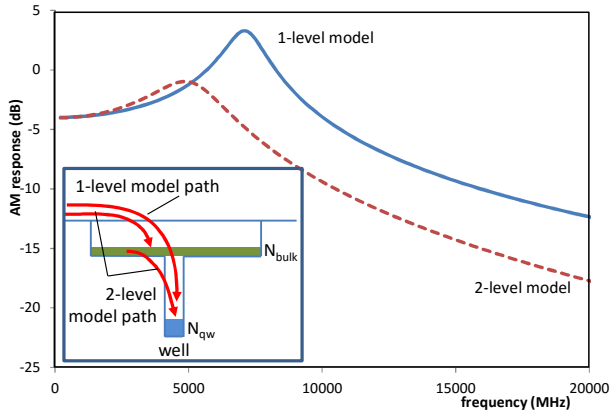



**Fig. 1. Modulation response of an InGaAsP Fabry Perot QW laser, with a 1-level and 2-level carrier model. The bulk carrier reservoir substantially reduces the modulation bandwidth of the laser.**

This is illustrated in Figure 2, modelled using a 2-level carrier model. Due to saturation effects a DC-driven SOA can severely degrade the eye. Modulating the SOA improves matters. Since the SOA experiences non-uniform gain saturation along it's length, better results are obtained by tailoring the modulation current $\Delta J(z)$ to the optical intensity profile P(z). The "split SOA" in Fig 2 approximates this showing further improvement.

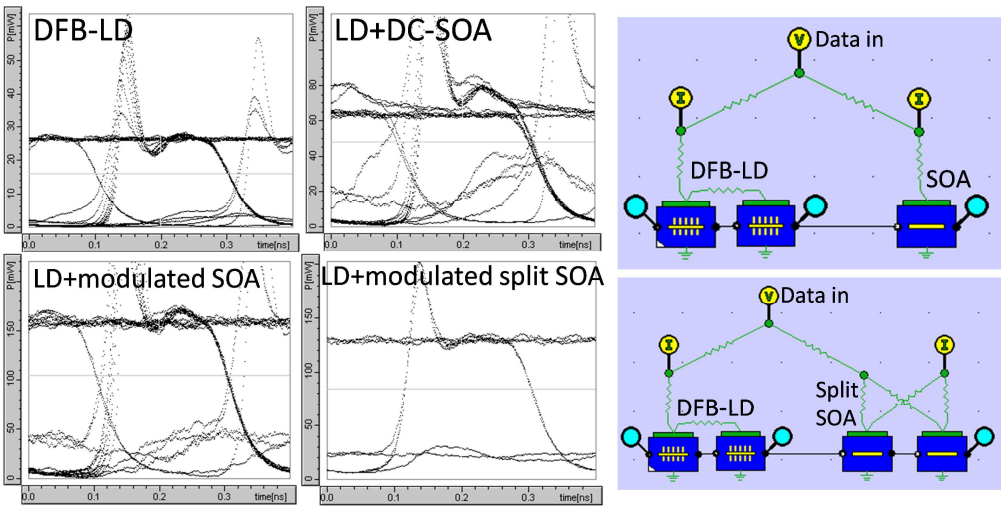



**Fig. 2. Eye diagrams for a DFB-LD/modulated-SOA InGaAP transmitter, with 5GB/s NRZ data in. Top right and bottom-right show schematics of the LD+SOA and LD+split-SOA circuits respectively.**

[1] L. M. Zhang, S. F. Yu, M. C. Nowell, D. D. Marcenac, J. E. Carroll, and R. G. S. Plumb, "Dynamic analysis of radiation and side-mode supression in a second-order DFB laser using time-domain large-signal travelling wave model", JQE, 30, pp. 1389-1395, 1994
[2] 1 Proc. SPIE v5, 5722-69, "Design and simulation of widely tunable lasers using a time domain travelling wave model",2004
[3] 1 Proc. SPIE 3889, pp. 96-106 "Modeling of facet heating in high power laser diodes", 2000
[4] 1 Y. Matsui, US Patent 2013/0308959 "Directly modulated laser for PON applications", 2013

ECIO 2016
18TH EUROPEAN CONFERENCE ON INTEGRATED OPTICS 2016
18–20 MAY | WARSAW | POLAND

# InP-based Photonic Integration Platform: Status and Prospects

**Victor DOLORES-CALZADILLA*, Francisco M. SOARES, Moritz BAIER, Tom GAERTNER, Mike FEYER, Martin MÖHRLE, Norbert GROTE, Martin SCHELL**
Fraunhofer Heinrich-Hertz Institute, Einsteinufer 37, 10587 Berlin, Germany
*victor.calzadilla@hhi.fraunhofer.de

Photonic integration has a key role in the further expansion of the information technologies and it is expected to result in the disruption of many industry sectors [1]. Such a transition promises to lower the energy consumption of optoelectronic systems as well as to enable a broad range of new applications. Multi Project Wafer (MPW) runs for photonics have been implemented during the last decade, which target the use of a generic integration technology with high functionality at low cost [2].

At the Fraunhofer HHI, a generic photonic platform has been developed within the framework of the European projects EuroPIC and PARADIGM. It is commercially available either through MPW runs brokered by JePPIX [3] or by dedicated private runs. The platform started with receiver-only capabilities and evolved rapidly over the years into a Tx-Rx platform. Figure 1 shows a schematic of the evolution of our platform including the potential developments for the near future (Generation IV).

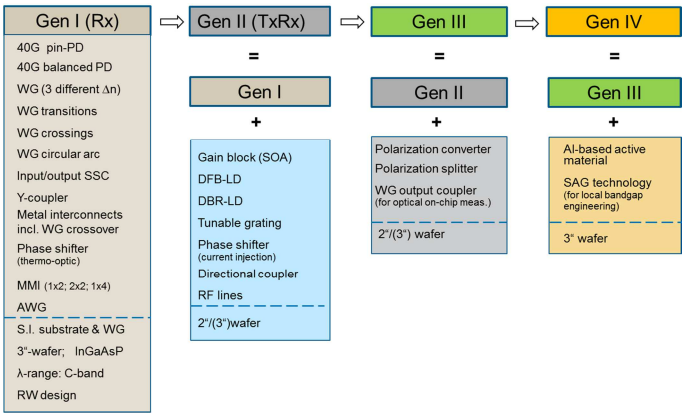



**Fig. 35. Schematic showing the evolution of the HHI photonic platform.**

The platform is based on a Fe-doped semi-insulating substrate which provides high electrical isolation between active devices as well as reduced parasitics for high speed operation. Furthermore, the epitaxial growth of light emitting diodes (using InGaAsP active quantum wells) and photodiodes (using InGaAs bulk) is done separately, meaning that sources and detectors are optimized independently. Moreover, p-type doping is performed only in areas where low contact resistance is required (i.e. in the active devices) by local diffusion. This allows the co-existence of both active devices with low series resistance and low-loss passive waveguide components free from intra-band absorption loss. Regarding on-chip optical routing, the platform offers three types of waveguides (Fe-doped Q1.06) with low, medium and strong confinement. As a unique feature, it also offers a spot-size converter (SSC) to provide optical coupling to single mode optical fibers.

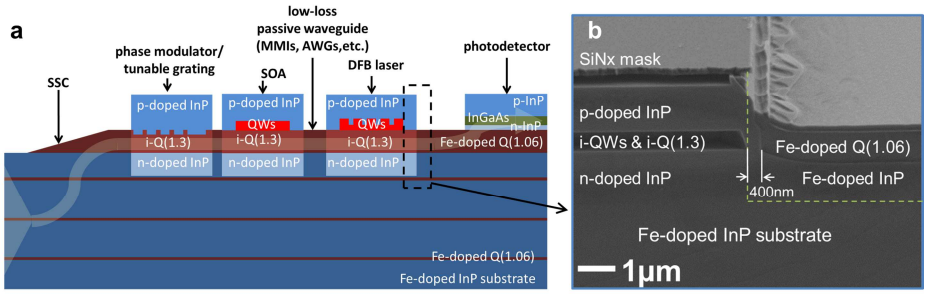



**Fig. 36. (a) Cross section schematic along the light propagation direction. (b) Scanning Electron Microscope photo along the active-passive interface corresponding to area indicated with dashed line in Fig 2a.**

The platform performance is sufficient for many applications requiring transmitter and receiver capabilities. It includes photodiodes with >40 GHz bandwidth and responsivity >0.8 A/W, as well as dark current ~1 nA at -3 V, distributed feedback lasers with >20 GHz bandwidth at 100 mA, waveguide propagation loss <1 dB/cm, spot-size converter with ~1.5 dB insertion loss for chip-to-fiber optical coupling, polarization converter with >15 dB extinction ratio over C-band [4], etc. In order to achieve this performance, an extensive process development has been carried out, including the optimized butt-joint regrowth across 3-4 μm high mesas to achieve 0.8 – 1.2 dB loss per active-passive interface (see Fig. 2b).

A number of devices and technologies are under development for their integration to the platform. For example, the performance of polarization converters is being optimized to eventually be able to replace off-chip (bulky) discrete optical elements. Moreover, the inclusion of Al-based active material for high temperature operation is also under investigation. Selective area growth to engineer the electroluminescence/absorption spectrum of each individual component is another potential extension.

Our current photonic integration platform relies on mature technology to offer an extensive library of building blocks, which is already being exploited in diverse applications. Future platform generations will incorporate new features to further increase the performance and extend its functionality.

References

[1] M. K. Weldon, “The future X network: a Bell Labs perspective”, CRC Press, 2015.
[2] M. Smit et al., “An introduction to InP-based generic integration technology”, J. of Semicon. Science and Technology, vol. 29, no. 8, 2014.
[3] www.jeppix.eu
[4] M. Baier et al., “Highly Fabrication Tolerant Polarization Converter for Generic Photonic Integration Technology”, 28th International Conference on Indium Phosphide and Related Materials, 2016.

ECIO 2016
18TH EUROPEAN CONFERENCE ON INTEGRATED OPTICS 2016
18–20 MAY | WARSAW | POLAND

# Unidirectional Operation of a Monolithically Integrated Mode locked Semiconductor Ring Laser

**Shuxuan Zhu[1*],Adrian Wonfor[1], Adrian Quarterman[1], Nikos Bamiedakis[1], Minsheng Ding[1], Richard Penty[1], Ian White[1]**

[1]Centre for Photonic Systems, Electrical Division, Department of Engineering,9 JJ Thompson Avenue, Cambridge, CB3 0FA, United Kingdom
[*] sz292@cam.ac.uk

## Introduction

Unidirectional operation is desirable attribute of a ring cavity laser. In fibre or bulk form this can be realized by applying discrete optical isolation techniques within the cavity. For monolithically integrated semiconductor lasers, the first monlithic integration of an optical isolator was reported by G. Takahashi *et.al.* in 2010 [1]. However, these are complex components which are difficult to integrate and are not available in the foundry used [2] in this work. Instead, we have realised unidirectional operation through the control of timing of the driving signals of the integrated laser. 4 GHz repetition rate pulses with a duration of 7ps and an energy of 0.24 pJ are generated.

## Device Structure

The QW semiconductor ring laser was fabricated based on the InP Foundry developed within the EU *PARADIGM* Project. A schematic diagram for the device is shown in Figure 1. The laser consists of three separate SOA sections which each have a length of 1000 µm. In the vicinity of each long SOA section, there are four short SOA sections of 50 µm length which act as saturable absorbers when reverse biased. At the output of the laser cavity, a Mach Zehnder modulator is integrated to control the intra-cavity power ratio which enables the mode locking operation regime to be adjusted and optimized.

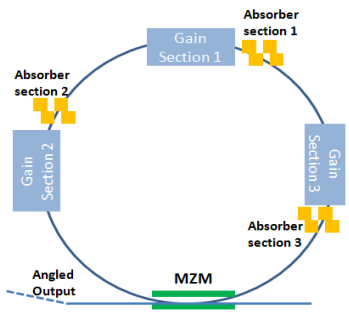



**Fig.1. Schematic diagram of Semiconductor ring laser.**

## Results and Analysis

Figure 2(a) shows the RF spectrum for passive mode locking operation, with corresponding pulse durations of 11 ps and energy of 0.15 pJ. To realize unidirectional operation, electrical delays are added to each of the RF pumping signals. With appropriate delays, the signals are in-phase for clockwise propagating pulses and out of phase for counter-clockwise pulses. As a result, the counter propagating signals are greatly suppressed resulting in unidirectional operation. The improvements in

performances can be observed in Figure 2(b) and (c) which shows that noise power near the fundamental harmonic is reduced by more than 10dB. Figure 2(d) shows the comparison of the autocorrelation traces. With in-phase pumping signals applied, the pulse width is reduced from 11 ps (red) to 7ps (black) with a corresponding energy increase from 0.15 pJ to 0.24 pJ.

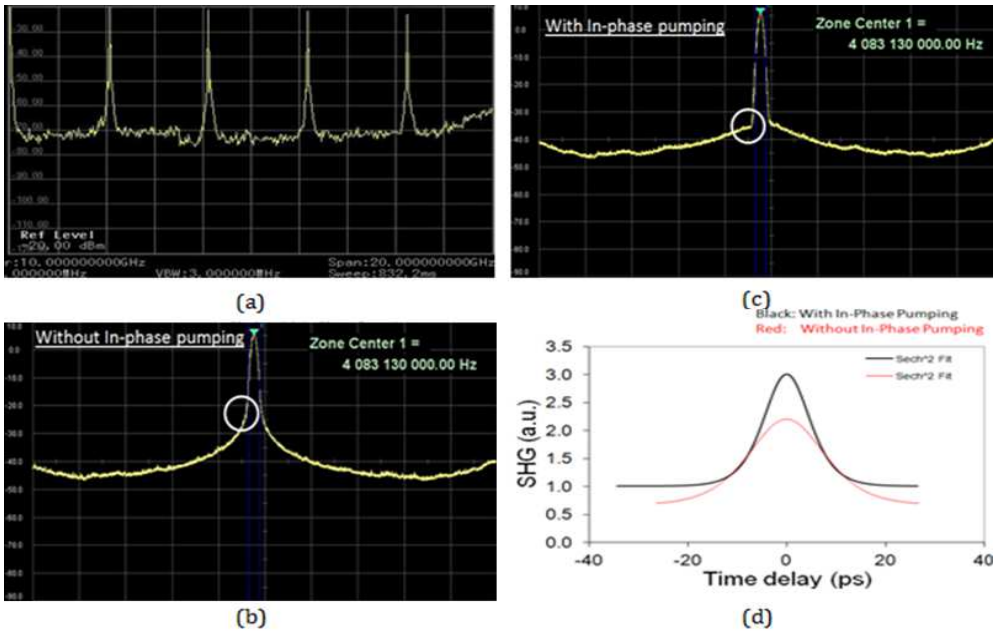



**Fig.2. (a) RF spectrum of passive mode locking operation (b) Without in-phase pumping (c) With in-phase pumping (d) Autocorrelation profile comparison**

## Conclusion

Unidirectional operation in a monolithically integrated semiconductor ring laser has been successfully realised for the first time without the integration of complex optical isolation components, by applying in-phase RF pumping signals.

## Acknowledgement

The research leading to these results has received funding from the European Community's FP7 programme under grant agreement ICT 257210 PARADIGM.

## References:

[1] G. Takahashi *et.al*, "TM mode waveguide isolator monolithically integrated with InP active devices", ICIP&RM, 206(1):1-4, 2010

[2] M. Smit *et.al*, "An introduction to InP-based generic integration technology," Semiconductor Science and Technology, vol. 29, p. 083001, 2014.